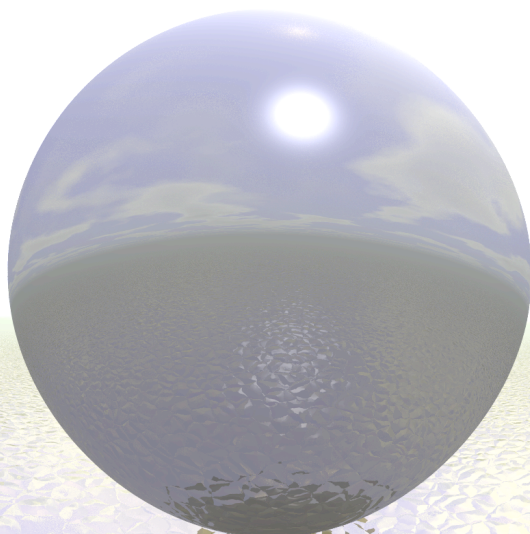


Activating Bonds

Theoretical studies of chemical bonds
and their catalytic activation by palladium

Willem-Jan van Zeist



VRIJE UNIVERSITEIT

Activating Bonds

Theoretical studies of chemical bonds
and their catalytic activation by palladium

ACADEMISCH PROEFSCHRIFT

ter verkrijging van de graad Doctor aan
de Vrije Universiteit Amsterdam,
op gezag van de rector magnificus
prof.dr. L.M. Bouter,
in het openbaar te verdedigen
ten overstaan van de promotiecommissie
van de faculteit der Exacte Wetenschappen
op woensdag 15 juni 2011 om 13.45 uur
in de aula van de universiteit,
De Boelelaan 1105

door

Willem-Jan van Zeist

geboren te Middelburg

promotor: prof.dr. F.M. Bickelhaupt

Activating Bonds

Theoretical studies of chemical bonds
and their catalytic activation by palladium

Willem-Jan van Zeist

This work has been financially supported by the National Research School Combination – Catalysis (NRSC-C) and the Netherlands Organization for Scientific Research (NWO-CW and NWO-NCF).

Cover art by Maya Beyhan (www.xs4all.nl/~pierphil/art/MayaBeyhan.html)

Activating Bonds

Theoretical studies on chemical bonds and their activation by palladium

Willem-Jan van Zeist

2011

"The first essential in chemistry is that thou shouldst perform practical work and conduct experiments, for he who performs not practical work nor makes experiments will never attain to the least degree of mastery."

- Abu Musa Jābir ibn Hayyān (Geber) (721 – 815 CE)

Table of Contents

1	Introduction.....	9
1.1	Applied theoretical chemistry	9
1.2	Oxidative insertion of palladium	10
1.3	This thesis	12
1.4	This thesis (practicalities)	13
2	Theory and methods.....	15
2.1	Density Functional Theory	16
2.2	Computational details	17
2.3	Activation strain model	19
2.4	Example of previous activation strain work	23
2.5	Proper analysis along the reaction coordinate	25
2.6	Choosing the reaction coordinate	31
2.7	Transition vector as approximation to IRC	35
2.8	PyFrag: streamlining your reaction path analysis!	37
3	The steric nature of the bite angle	39
3.1	Introduction	40
3.2	Stationary points	41
3.3	Bite and twist angle	43
3.4	More ligand effects	50
3.5	Conclusions	59
4	The effect of steric bulk on C–H bond activation	61
4.1	Introduction	62
4.2	Substrates	63
4.3	Stationary points	64
4.4	Activation strain analyses	68
4.5	Conclusions	76
5	The effect of steric bulk on C–C bond activation	77
5.1	Introduction	78
5.2	Substrates	78
5.3	Stationary points	80
5.4	Activation strain analysis	84
5.5	Conclusions	90
6	Analysis of H–AH_n and CH₃–AH_n bonds	91
6.1	Introduction	92
6.2	Results and discussion	93
6.3	Conclusions	99

7	Activation of H-AH_n and CH₃-AH_n bonds	101
7.1	Introduction	102
7.2	Stationary Points	102
7.3	Activation strain analysis	106
7.4	Ligand effects	108
7.5	Conclusions	115
8	Activation of C(sp³)-X, C(sp²)-X, and C(sp)-X bonds.....	117
8.1	Introduction	118
8.2	Stationary points	119
8.3	Activation strain analysis	122
8.4	Ligand effects	124
8.5	Conclusions	130
9	Summary	131
10	Samenvatting	135
11	Dankwoord	139
12	List of publications	141
13	References	143

1 Introduction

1.1 Applied theoretical chemistry

The field of theoretical chemistry is evolving at an increasingly rapid rate. Significant in this development is the exponential increase of the available computing power. For example, the computing power available at the department of Theoretical Chemistry at the Vrije Universiteit, where the work for this thesis took place, has been expanded a number of times. At each increase, the newly installed capacity amounted to more computing power than had been cumulatively present up until that point in time. This increase in computing capacity has made it easier for many chemists to look at chemical reactions with the help of computational chemistry tools. However, as with many things, quantity is not the only important aspect. Above all, a chemist wants to understand why a chemical reaction happens, and be able to talk about this in a qualitative fashion. Many theoretical chemists have developed and employed various analytical tools in order to better understand chemical reactions from a theoretical perspective. This thesis is but one example in a rich history of theoretical investigations into chemical reactivity.

This thesis focuses on the subject of catalysis, in particular homogeneous catalysis (where the reacting species are dissolved in one medium) using palladium as a reducing agent. Although chemists throughout the world continuously progress to understand catalytic processes, it is still often difficult to rationalize the reactivity of catalytic agents. Even more difficult is actually *predicting* the reactivity of a proposed catalyst. A good number of catalytic compounds discovered are found by trial and error, which is of course not the desired way to practice chemistry. The above is true for many areas of chemistry, but is perhaps especially challenging in the field of homogeneous catalysis, in which the role of the various versatile ligand systems can become very complicated.

Through theoretical chemistry, however, we can hope to gain a better insight into the inner workings of reaction mechanisms. In this way, we can hope to expand and improve upon the ‘chemical intuition’ that chemists use to rationalize reactivity. The approach we adopt is one of a gradual increase of insight in the reaction mechanisms, starting from simple model systems. This strategy is previously outlined in earlier work

as the ‘Fragment-oriented Design of Catalysts’,^{1,2} and focuses firstly on the intrinsic reactivity of model systems. On this we can expand by adding effects of ligands on the metal core, or the influence of changes in the substrates undergoing catalytic activation. This allows us to understand the changes in reactivity with relation to the core model system, and provide a more rational basis on which to design catalytic compounds to meet specific criteria for desired reactivity and selectivity.

1.2 Oxidative insertion of palladium

The 2010 Nobel Prize in Chemistry was awarded to Richard F. Heck, Ei-ichi Negishi and Akira Suzuki “*for palladium-catalyzed cross-couplings in organic synthesis*”.³

The choice of the Nobel Prize committee could not have come at a better time regarding the subject of this thesis, and emphasizes the relevance of the work presented in this thesis! These cross-coupling reactions have become an important tool in modern chemistry, and still deserve all the attention they get from

both experimental and theoretical perspectives. The theoretical work presented here tackles one of the fundamental reaction mechanism steps present in palladium-catalyzed cross-couplings: the oxidative insertion (in this thesis often abbreviated as ‘OxIn’, or alternatively: oxidative addition).

By now, it should not be surprising that the catalytic systems covered in this thesis are based on the transition metal palladium (Pd, see Figure 1.1). Palladium is considered a precious metal and is around twenty times more expensive than silver. The largest use of palladium nowadays is in catalytic converters, where, together with platinum and rhodium, it is the primary component that decreases vehicle exhausts emissions of hydrocarbons, carbon monoxides, oxides of nitrogen and other pollutants. Palladium is also widely used in jewelry, electronics, and as a component in alloys used for dentistry. Besides these applications palladium is, in many different forms, a widely used and versatile catalytic reagent in many different chemical processes.⁴ One other reason this thesis focuses on palladium is because it can serve excellently as the desired model system. The atomic ground state of Pd consists of a closed-shell d^{10}



Figure 1.1 Palladium.

configuration, which facilitates comparison with more realistic transition metal complexes used in catalytic bond activation. Besides all that, the fact that palladium “won” the Nobel Prize also confirms that palladium oxidative insertion reactions are highly relevant in catalysis and a logical choice for investigation.

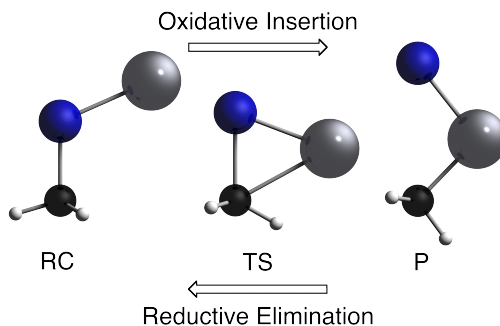


Figure 1.2 The oxidative insertion (OxIn) step, the reverse is called reductive elimination.

The main focus of this thesis is the oxidative insertion reaction, a key step, often rate-determining, in many catalytic cycles, in which a reactant (substrate) adds to a metal complex, forming the reactant complex (RC, see Figure 1.2).⁵⁻⁷ Since it is an important mechanism in catalytic reactions, numerous experimental⁸⁻¹⁵ and theoretical¹⁶⁻²⁶ papers have appeared on this subject. This bond activation mechanism is also present in heterogeneous catalysis where, of course, interesting theoretical research can be found as well.^{27,28} In this step a relatively inert bond of the substrate is broken via a transition state (TS) and the electrons of this bond are formally transferred to the metal center, thereby oxidizing the substrate and forming the product (P). For example, if the C–Cl bond in chloromethane is activated by Pd this leads to the cleavage of the covalent bond between the methyl moiety and the chlorine atom. Simultaneously, two new bonds are formed in the resulting compound $\text{CH}_3\text{-Pd-Cl}$. Because two previously non-bonding electrons of Pd have become involved in order to form these bonds, its formal oxidation state changes from Pd(0) to Pd(II). The formal character should be emphasized since the product should not be regarded as having a very strict internal charge separation of the type $\text{CH}_3\text{-Pd}^{2+}\text{-Cl}^-$. The reverse reaction of oxidative addition is called reductive elimination; both processes are important in a large range of catalytic cycles.

Figure 1.3 shows a schematic example of a catalytic cycle: the aforementioned, Nobel Prize winning, cross-coupling reaction. Here, Pd(0) activates the aryl–X bond in the oxidative addition step, forming the Ar–Pd–X compound. After this, a substitution can occur by a nucleophile, followed by the reverse reaction of reductive elimination. In this step, the product of the catalytic cycle is formed, and simultaneously the catalytic compound Pd(0) is recovered. The first step in the cycle is primarily the breaking of the aryl–X bond, and is thus also often called the bond activating or

bond-breaking step. This bond-breaking step is the part of the catalytic cycle which this thesis focuses on, since it is often not only the rate-determining step, but also important in defining the selectivity of the catalytic process.

Important in the catalytic behavior of the central metal atom is the influence of the ligands. Different ligands can enhance or decrease catalytic activity, but can also steer its selectivity, both by influencing orbital energies and the steric properties of the catalytic compound. In many theoretical investigations the simple analogues of phosphine-based ligands are employed in the form of PH_3 ligands forming $\text{Pd}(\text{PH}_3)_2$.²⁹⁻³⁸ Another ligand that is routinely used in our investigations is anionic Cl^- , which has the overall effect of lowering barriers.³⁹ A recurring theme throughout this thesis will be the steric nature of the geometrical (bite and twist angle) features of phosphine ligand systems.

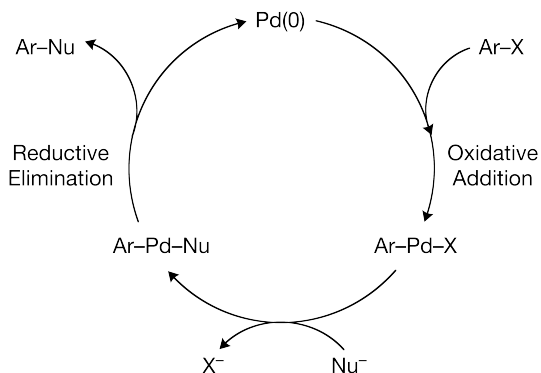


Figure 1.3 A schematic catalytic cycle including an oxidative insertion (OxIn) step of Pd into Ar-X.

1.3 This thesis

As must be clear by now, this thesis concentrates on a theoretical investigation of palladium-mediated bond-activation reactions. This is done by investigating the intrinsic reactivity of palladium toward series of archetypal bonds, and similarly series of archetypal ligands. Before going into the detailed analyses of the reactions, chapter 2 will give a thorough overview of the model analysis that is employed in this thesis: the activation strain model. Correctly understanding this type of analysis is a fundamental aspect, and this thesis will hopefully aid those interested in learning more about the activation strain model. This chapter also introduces the fundamentals of Density Functional Theory (DFT), as well as the computational details of the ADF program that performs the DFT calculations.

Chapter 3 will introduce and investigate the concept of the 'bite angle'; the ligand-metal-ligand angle in bidentate (and PH_3 -bisligated) systems. In the case of the analysis with palladium, phosphines are useful model ligands, and the bite angle becomes

the P–Pd–P angle. Through a series of analyses we elucidate the steric nature of this bite angle, and also that of the related twist angle in the transition state geometry.

Chapter 4 and 5 will introduce a range of CR₃–H and CR₃–CR₃ bonds, with the CR₃ groups becoming increasingly sterically congested. The chapters analyze the effect of an increasing number of sterically hindering substituents that become especially interesting when the bond is fully saturated with these groups.

Chapter 6 and 7 focus on the series of simple second period bonds: H–AH_n and CH₃–AH_n with AH_n = CH₃, NH₂, OH, and F. The first of these two chapters has a slightly different focus, as it shows an analysis of the bonds to explain apparent anomalies in the trends of bond strengths found in these series of increasingly polar bonds across the second period. The second chapter proceeds with the by then familiar treatment of the activation of these bonds by model palladium compounds.

Chapter 8 treats another interesting series of bond activations, comprised of a series of differently hybridized bonds C₂H₅–X, C₂H₃–X, C₂H–X (with X = H, CH₃, Cl). Similar as in the previous chapter, an important aspect of understanding the activation of these bonds lies in the balance between bond strengths (i.e. how difficult is it to break the bond) and the interaction strength between palladium and the substrate. It turns out that there are quite some similarities to be found in this analysis compared to chapter 7.

1.4 This thesis (practicalities)

Supporting information in the form of various videos depicting the reaction paths calculated for the reactions under consideration for each chapter can be found via <http://www.few.vu.nl/~bickel>. It can be very instructive to really ‘see’ the reaction happening, especially since it can often nicely visualize the deformation of catalyst complexes and substrates.

As this thesis will only have a limited hard copy circulation, the emphasis of the distribution will be on the PDF-version. Because of this, the ‘dead-tree edition’ will be a black and white print, and may not display all the nice color graphs as beautifully as compared to the electronic version, which should be preferably viewed on a full color computer screen, eReader, or iPad. The reasons for the limited amount of printed copies are: 1) a desire for a paperless future where hard copies are considered nostalgic; 2) environmental considerations.

2 Theory and methods

Inspired by:

Willem-Jan van Zeist, F. Matthias Bickelhaupt

Org. Biomol. Chem. **2010**, *8*, 3118

Willem-Jan van Zeist, Celia Fonseca Guerra, F. Matthias Bickelhaupt

J. Comput. Chem. **2008**, *29*, 312

Willem-Jan van Zeist, Anton H. Koers, Lando P. Wolters, F. Matthias Bickelhaupt

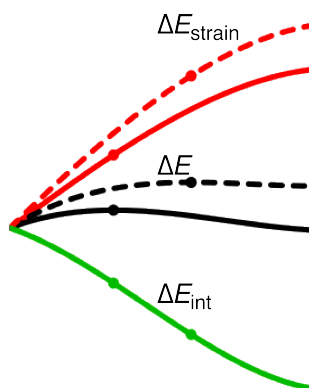
J. Chem. Theory. Comput. **2008**, *4*, 920

Willem-Jan van Zeist, F. Matthias Bickelhaupt

Chem. Eur. J. **2010**, *16*, 5338

Abstract

This chapter describes the general theoretical approach used throughout this thesis. Firstly, an overview is given of the underlying DFT quantum-mechanical approach and the computational details of the level of theory employed for the calculations. After this, the activation strain model is described, which is an analysis tool used extensively in all chapters of this thesis. Examples of the application of the activation strain model on oxidative insertion reactions are given, with an emphasis on best practices and the proper choice of a reaction coordinate. Finally, the PyFrag program is introduced; a small program that helps to easily perform a proper activation strain analysis along the reaction path.



2.1 Density Functional Theory

Density functional theory (DFT)⁴⁰⁻⁴² is a widely used approach adopted in order to calculate the electronic structure, and thus energies and other properties, of chemical systems. The main advantage of the method lies in the fact that the calculations are relatively cheap, especially when compared to higher-level methods. A drawback is that it still has an approximation-based character, making the results inherently relatively inaccurate. This thesis focuses on utilizing the calculations as a means to improve our understanding of chemical processes and will therefore not treat the underlying computational methods in detail. What follows is a short introduction to the principles of DFT. There are of course many excellent textbooks to be found that provide far more thorough accounts.⁴⁰⁻⁴²

The basis of DFT is the expression of the ground state energy as a function of the electron density: $E = E[\rho]$. Kohn and Sham developed a practical application of this theory. They postulated a reference system of N non-interacting electrons, moving in an effective potential. By construction, the density of this non-interacting system equals the real, interacting system. Thus, according to the Kohn-Sham theorem, the exact energy functional can be expressed as

$$E[\rho(\mathbf{r})] = T_S[\rho(\mathbf{r})] + E_{ne}[\rho(\mathbf{r})] + E_C[\rho(\mathbf{r})] + E_{XC}[\rho(\mathbf{r})] \quad (2.1)$$

in which the exact electron density can be expressed as a linear combination of the Kohn-Sham orbital densities:

$$\rho(\mathbf{r}) = \sum_i |\phi_i|^2 \quad (2.2)$$

In equation 2.1, $T_S[\rho(\mathbf{r})]$ represents the kinetic energy of the electrons of the non-interacting reference system. $E_{ne}[\rho(\mathbf{r})]$ is the electrostatic attraction between the electrons and the nuclei, and $E_C[\rho(\mathbf{r})]$ is the classical Coulomb repulsion of the electron cloud with itself. $E_{XC}[\rho(\mathbf{r})]$ is the so-called exchange-correlation energy, which accounts for the self-interaction correction, exchange and Coulomb correlation between electrons, but also includes a correction for the fact that $T_S[\rho(\mathbf{r})]$ differs from the exact kinetic energy $T[\rho(\mathbf{r})]$.

The orbitals ϕ_i are obtained from the one-electron Kohn-Sham equations:

$$h_{\text{eff}} \phi_i = \varepsilon_i \phi_i \quad (2.3)$$

$$\left[\frac{1}{2} \nabla^2 + v_S(\mathbf{r}) \right] \phi_i = \varepsilon_i \phi_i \quad (2.4)$$

The Kohn-Sham potential $v_S(\mathbf{r})$, which the reference electron experiences, comprises the attractive potential, $v_n(\mathbf{r})$, of the nuclei and the classical Coulomb repulsion, $v_C[\rho(\mathbf{r})]$, with the electron density $\rho(\mathbf{r})$, as well as the self-interaction correction and all exchange correlation effects contained in the so-called exchange-correlation potential, $v_{XC}[\rho(\mathbf{r})]$. The latter is not known exactly and is usually ‘simply’ defined as the functional derivative of $E_{XC}[\rho]$ with respect to ρ . The terms v_C and v_{XC} actually depend on the density which they are meant to calculate. This issue is resolved by using the self-consistent field (SCF) procedure in which a ‘guess’ of the density is made to calculate the potential v and solve the Kohn-Sham equations. This yields a set of orbitals ϕ_i from which a better density can be constructed using equation 2.2, which is used as a new ‘guess’ density. This scheme is repeated until the density converges compared to the previous iteration and this results in the Kohn-Sham orbitals for which the energy reaches its lowest value via equations 2.2 and 2.3.

The exact form of the exchange-correlation potential, $v_{XC}[\rho(\mathbf{r})]$, is not known and a large number of approximations to this term have been developed. The main types of functionals that approximate the exchange-correlation potential are the local density approximation (LDA), generalized gradient approximation (GGA), meta-GGA, and hybrid DFT methods. Generally, the approximations used are simple denoted as ‘functionals’ and usually carry short acronyms such as for example the BLYP (Becke-Lee-Yang-Parr) functional that is used in this thesis.⁴³⁻⁴⁵

2.2 Computational details

All calculations in this thesis are based on density functional theory (DFT)^{40-42,46,47} and have been performed using the Amsterdam Density Functional (ADF) program.^{48,49} The specific approach as outlined in the next couple of paragraphs has been validated for the palladium oxidation reactions by previous research in our group. Specifically, the BLYP functional (which is used throughout this thesis) was thoroughly benchmarked against high-level coupled-cluster calculations and shown to be the best functional for the type of reactions covered in this thesis.⁵⁰⁻⁵⁴ The limitations of using DFT are of course obvious, but it should be emphasized that this thesis does not aim to give quantitative exact numbers for the reaction paths described. The DFT method applied, however, does give us a reasonably accurate basis to discuss the trends in energies encountered in comparing different reactions.

MOs were expanded in a large uncontracted set of Slater-type orbitals (STOs).⁵⁵ The basis is of triple- ζ quality and has been augmented with two sets of polarization

functions: $2p$ and $3d$ on hydrogen, $3d$ and $4f$ on carbon, nitrogen, oxygen, fluorine, chlorine, oxygen, and phosphorus, $4d$ and $4f$ on bromine, $5d$ and $4f$ on iodine, and $5p$ and $4f$ on palladium. The core shells of carbon, nitrogen, oxygen, and fluorine ($1s$), phosphorus and chlorine (up to $2p$), bromine (up to $3p$), iodine (up to $4p$), and palladium (up to $3d$) were treated by the frozen-core approximation.⁵⁶ An auxiliary set of s , p , d , f , and g STOs was used to fit the molecular density and to represent the Coulomb and exchange potentials accurately in each SCF cycle.⁵⁷

Geometries and energies were calculated using the generalized gradient approximation (GGA). Exchange is described by Slaters' $X\alpha$ potential, with nonlocal corrections due to Becke.^{43,44} Correlation is treated in the Vosko-Wilk-Nusair (VWN) parameterization using formula V,⁵⁸ with nonlocal corrections due to Lee, Yang and Parr.⁴⁵ This is the BLYP functional, where the local correlation (LDA VWN) is included in the LYP correlation functional. Scalar relativistic effects were taken into account by the zeroth-order regular approximation (ZORA).⁵⁹⁻⁶¹ Taking into account the relativistic effects is important for the accuracy of the results, as demonstrated in earlier work.⁶² All stationary points were additionally obtained (with complete geometrical optimization) including water solvent effects by making use of the conductor-like screening model (COSMO),⁶³⁻⁶⁵ as implemented in the ADF program.⁶⁶ Settings can be found in previous work.⁶⁷ The activation strain analyses employed in this thesis (see the next section) can also be extended to incorporate these solvent effects.⁶⁸ For some stationary points, the QUILD code was used, which is an advanced user option built in the ADF package.⁶⁹

Through vibrational analysis,⁷⁰ all energy minima and transition state structures⁷¹ were confirmed to be equilibrium structures (no imaginary frequencies) or a transition state (one imaginary frequency). The character of the normal mode associated with the imaginary frequency was analyzed to ensure that the correct transition state was found. Where computationally feasible, intrinsic reaction coordinate (IRC)⁷²⁻⁷⁶ calculations were performed to obtain the potential energy surfaces (PES) of the reactions. Otherwise, TV-IRC approximations (explained in paragraph 2.7) to the true IRC were made.⁷⁷ Vibrational energy effects (in particular, zero-point vibrational energy) and entropy effects are generally not considered in this thesis. The values of these effects can be found in the supporting information of the articles that form the basis for this thesis. However they usually have only a small influence on the energies obtained and never change the trends in barriers. Where they are used, enthalpies at 298.15 K and 1

atmosphere (ΔH_{298}) were calculated from electronic energies (ΔE) and our frequency computations using standard statistical-mechanics relationships for an ideal gas.⁷⁸

2.3 Activation strain model

The activation strain model of chemical reactivity provides the ingredients required for a thorough understanding of chemical reactivity and trends therein in terms of the properties of the reactants.^{79,80} In the first place, it relates the height of the activation energy to the rigidity of the reactants and the geometrical deformation that is associated with (and characteristic for) the reaction pathway under consideration. This aspect of geometrical distortion (by definition destabilizing) is expressed in an energy term dubbed the strain energy. The second quantity in this model is related to the bonding capabilities and mutual (potentially destabilizing) interactions between the increasingly deformed reactants along the same pathway, as explained below.

As indicated briefly above, the activation strain model is a fragment-based approach to understanding chemical reactions and the associated barriers. The starting point is the two separate reactants, which approach from infinity and begin to interact. In the case of the oxidative insertion mechanism, this embodies the substrate undergoing the bond

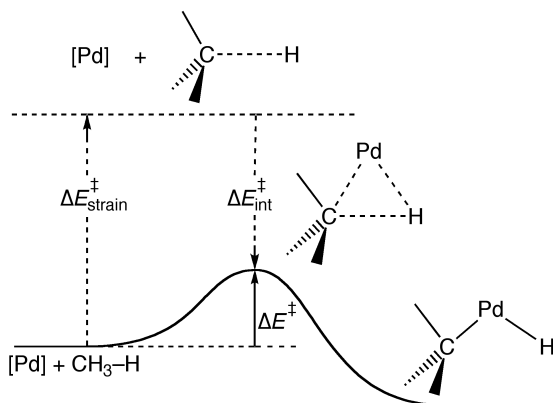


Figure 2.1 Illustration of the activation strain model applied on oxidative insertion into the C–H bond.

addition, and a palladium catalytic complex that is oxidized during the process. As the reaction progresses the reactants increasingly deform each other in order to achieve the overall geometry in the activated complex. In this model, the activation energy ΔE^\ddagger of the transition state (TS) is decomposed into the strain energy $\Delta E^\ddagger_{\text{strain}}$ and the interaction energy $\Delta E^\ddagger_{\text{int}}$:

$$\Delta E^\ddagger = \Delta E^\ddagger_{\text{strain}} + \Delta E^\ddagger_{\text{int}} = \Delta E^\ddagger_{\text{strain}}[\text{sub}] + \Delta E^\ddagger_{\text{strain}}[\text{cat}] + \Delta E^\ddagger_{\text{int}} \quad (2.5)$$

The activation strain $\Delta E^\ddagger_{\text{strain}}$ is the energy associated with deforming the reactants from their equilibrium geometry into the geometry they acquire in the activated complex. One can achieve this by simply calculating the electronic energy of the molecule

in the deformed state, and comparing it to the equilibrium energy. The strain can be divided into a contribution stemming from the catalyst ($\Delta E_{\text{strain}}^{\ddagger}[\text{cat}]$) and the substrate ($\Delta E_{\text{strain}}^{\ddagger}[\text{sub}]$) in the case of catalytic bond activation. The TS interaction $\Delta E_{\text{int}}^{\ddagger}$ is the actual interaction energy between the deformed reactants as they are brought together in the geometry they assume in the activated complex.

The model can be extended to incorporate the entire reaction path (see Figure 2.1).^{39,62,77,79,81-83} The decomposition of the energy $\Delta E(\zeta)$ into strain $\Delta E_{\text{strain}}(\zeta)$ and interaction $\Delta E_{\text{int}}(\zeta)$ is carried out along the reaction coordinate ζ , i.e., from reactants via TS to products. The reaction coordinate, ζ , is usually obtained as the intrinsic reaction coordinate (IRC) calculation.⁷²⁻⁷⁶ The IRC method yields the minimum energy path connecting reactants and products via the paths of steepest descent from the associated transition state. The minimum energy path resulting from the IRC has been successfully used in many studies as a basis of reaction path analysis.⁸⁴ This reaction path, or potential energy surface (PES)⁸⁵, may then be projected onto a critical geometrical parameter, such as the bond that is broken during a bond-activation process. For ADF, the PyFrag program was developed, which acts as a wrap-around for ADF and streamlines performing the activation-strain analysis on, among others, IRC calculations.⁸⁶ More information on PyFrag can be found in section 2.8.

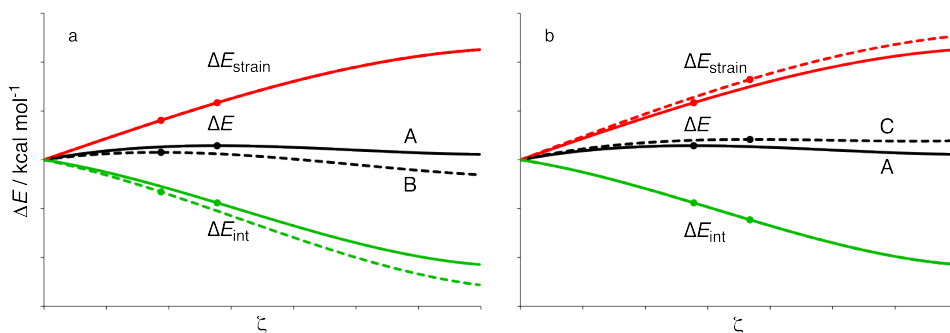


Figure 2.2 Schematic illustration of activation strain analyses for arbitrary reactions A, B and C. (a) From reaction A to B, the interaction energy becomes more stabilizing, which lowers the TS (indicated by a dot) and shifts it towards the educt side, at the left. (b) From reaction A to C, the strain energy becomes more destabilizing, which raises the TS and shifts it towards the product side, at the right.

The values of $\Delta E_{\text{strain}}^{\ddagger}$ and $\Delta E_{\text{int}}^{\ddagger}$ at the TS must be carefully interpreted, since the optimized TS structure is the result of a balance of the components $\Delta E_{\text{strain}}(\zeta)$ and $\Delta E_{\text{int}}(\zeta)$. Along the reaction coordinate, the strain $\Delta E_{\text{strain}}(\zeta)$ increases, in general, because the substrate becomes increasingly deformed (see Figure 2.2). At the same time, the interaction $\Delta E_{\text{int}}(\zeta)$ becomes more stabilizing in most cases. The net result is the

total energy profile $\Delta E(\xi)$ which achieves its maximum (i.e., the TS) at the point along the reaction coordinate where $d\Delta E_{\text{strain}}(\xi)/d\xi = -d\Delta E_{\text{int}}(\xi)/d\xi$.

This highlights the importance of taking into account the behavior of the two components along the reaction coordinate, especially their slopes. A single-point analysis at the TS only, yields values that can be misleading, as can be seen from the activation strain diagrams in Figure 2.2. For example, going from reaction A to reaction B in Figure 2.2a decreases the barrier. A single-point analysis at the respective TSs indicates that this is due to a lower activation strain, not because of a more stabilizing TS interaction. This suggests that the mutual bonding capability of the reactants in reaction B is reduced, but that the barrier is nevertheless lower because of a lower rigidity or a less distortive character of the reaction as compared to reaction A. However, the more complete analysis in Figure 2.2a shows that this is obviously incorrect. The interaction ΔE_{int} of reaction B is *more stabilizing at any given point along the reaction coordinate* than ΔE_{int} of reaction A. The fact that this seems to be reversed in the single-point analyses is because the TS structures of A and B occur at different locations along the reaction path. An equivalent reasoning also applies when going from reaction A to reaction C (Figure 2.2b), where the interaction energy is similar along the entire path, an observation easily overlooked at the TSs only. This important issue is treated in more detail in section 2.5.

Note that in the activation strain diagrams in Figure 2.2, all energy curves start, on the reactant side, at zero kcal mol⁻¹. However, reactions often proceed from a reactant complex that is formed prior to traversing the transition state. Such a precursor complex is then conveniently used as the starting point for the activation strain analysis. Therefore, in practice, the energy curves of an activation strain analysis start at a point in the diagram where the reaction coordinate ξ is already slightly larger than zero (reactant complex formation) and the reactants do already (weakly) interact and deform each other, i.e., $\Delta E(\xi)$, $\Delta E_{\text{strain}}(\xi)$, and $\Delta E_{\text{int}}(\xi)$ may already slightly deviate from zero (see for example Figure 2.6).

The interaction ΔE_{int} between the deformed reactants can be further analyzed in the conceptual framework provided by the Kohn-Sham molecular orbital model.⁴⁷ Thus, $\Delta E_{\text{int}}(\xi)$ is further decomposed into three physically meaningful terms using a quantitative energy decomposition scheme developed by Ziegler and Rauk.^{87,88} Although the decomposition into $\Delta E_{\text{strain}}(\xi)$, and $\Delta E_{\text{int}}(\xi)$ as described earlier can be performed by any quantum mechanical computational program, this is not the case for the interaction energy decomposition analysis, which is only implemented in ADF.

$$\Delta E_{\text{int}}(\xi) = \Delta V_{\text{elstat}}(\xi) + \Delta E_{\text{Pauli}}(\xi) + \Delta E_{\text{oi}}(\xi) \quad (2.6)$$

These three terms allow a thorough assessment of the interaction between the deformed reactants. The term ΔV_{elstat} corresponds to the classical electrostatic interaction between the unperturbed charge distributions of the deformed reactants and is usually attractive. The Pauli repulsion ΔE_{Pauli} comprises the destabilizing interactions between occupied orbitals and is responsible for the steric repulsion. The orbital interaction ΔE_{oi} accounts for charge transfer (interaction between occupied orbitals on one moiety with unoccupied orbitals on the other, including the HOMO–LUMO interactions) and polarization (empty–occupied orbital mixing on one fragment due to the presence of another fragment). The basis of this approach is, in essence, a molecular orbital approach using the (in principle exact) molecular orbitals that originate from the Kohn–Sham DFT calculations of the fragments. It is thus appropriate to view the interaction terms from this perspective, as schematically depicted in Figure 2.3. For the description of the oxidative insertion process, especially the Pauli repulsion, donation, and back-donation terms are important.

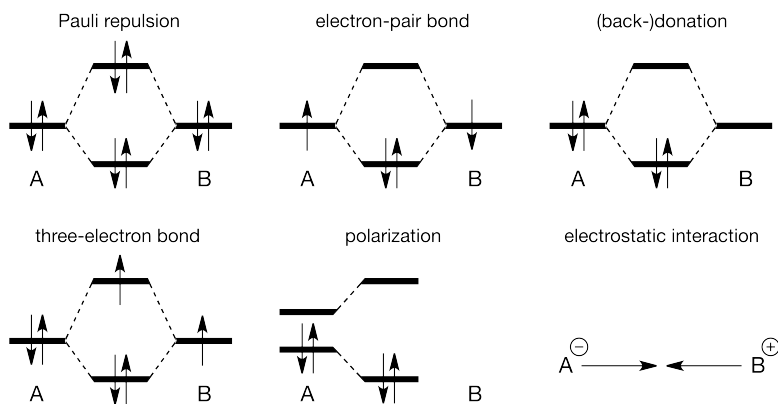


Figure 2.3 Schematic representation of a number of elementary types of interaction between fragments A and B in the Kohn–Sham MO model.

In addition to studying reactions that proceed via energy barriers, the activation strain model can also be applied to simple, barrier-free bond formation reactions: $A + B \rightarrow A-B$. The stability and length of emerging A–B bond are again a result of an interplay between stabilizing and destabilizing forces, very similar to the situation described above for the energy of the TS and its position along the reaction coordinate. Thus, the same precautions should be taken if one attempts to reveal the origin of the strength and length of bonds in stable molecules based solely on the basis of a single-point analysis at the equilibrium geometry. It is always more complete (and often even

crucial) to carry out the analysis along the "reaction coordinate", i.e., as a function of the bond distance under consideration.^{89,90} Chapter 6 of this thesis deals with such analyses across a range of bonds.

A note of caution lies in the analysis of these bond formation reactions, which inherently should use open-shell fragments if an electron-pair bond is formed. In the energy decomposition analysis, open-shell fragments are treated with the spin-unrestricted formalism, but, for technical (not fundamental) reasons, spin polarization is not included. This error causes an electron-pair bond to become too strong in the order of a few kcal mol⁻¹. This is the case in chapter 6 of this thesis. However, this small difference does not in any way affect the qualitative discussion concerning the values of the energy decomposition.

Finally, the activation strain model has evolved from studying bimolecular reactions. It can however also be applied to unimolecular processes, for example, the internal rotation of ethane⁹¹ and biphenyl.⁹² Note that, in the case of unimolecular reactions, one has to make an explicit choice of fragments within the reorganizing species (e.g., the two methyl fragments that rotate with respect to each other in ethane) whereas for bimolecular reactions these fragments are by default the two reactants.

2.4 Example of previous activation strain work

The activation strain model has been thoroughly applied to the oxidative addition step in catalytic bond activation.^{1,2,39,62,68,82,83,93-98} In this section, an example of the activation strain model to an oxidative insertion reaction is given, taken from earlier work on extending the activation strain model.⁸³

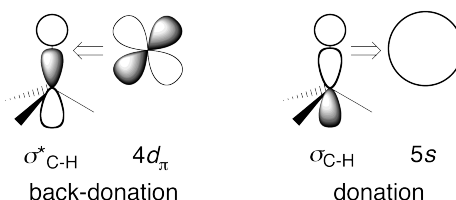


Figure 2.4 Schematic representation of back-donation and donation in the insertion of bare palladium into the methane C–H bond.

Oxidative insertion is essentially a (metal-mediated) bond-breaking process, where the strength of the bond is of obvious importance. The energy related to the bond breaking is reflected by the strain term of the substrate. The bond-breaking process is facilitated by a back-donation interaction of metal *d* orbitals into the empty σ^* antibonding orbital of the activated bond in the substrate (see Figure 2.4). Another contributing factor is the donation from the filled substrate's σ bonding orbital into the empty *s* orbital on palladium. This donation further weakens the bond, but the effect of back-donation is usually the dominant factor.

An interesting example of strain effects on the substrate is the insertion into the C–C bond in cyclopropane (see Figure 2.5). Compared to the C–C bond in ethane, one may expect a relatively easy insertion process due to the weak C–C bond in the highly strained ring system. Indeed, this insertion proceeds without any barrier (except for a small barrier upon breaking

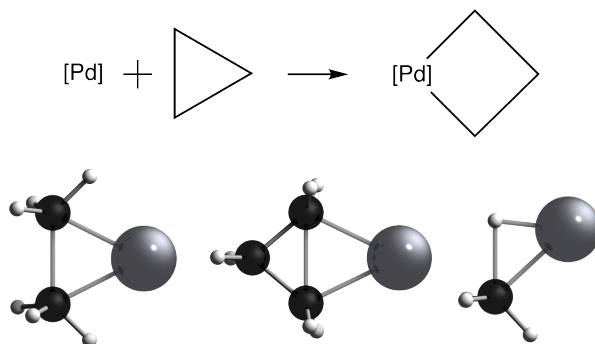


Figure 2.5 Schematic depiction of the oxidative insertion of palladium into the strained C–C bond in cyclopropane. Also shown are the TS structure of the ethane C–C insertion, the cyclopropane insertion progressed to a comparable C–C length, and the C–H insertion TS structure.

free from the reactant complex prior to the insertion). This is a radical change compared to the 18 kcal mol⁻¹ barrier for the insertion into the ethane C–C bond. The activation strain model can straightforwardly show that this decrease in bond strength lowers the insertion barrier because of the lower strain energy term.

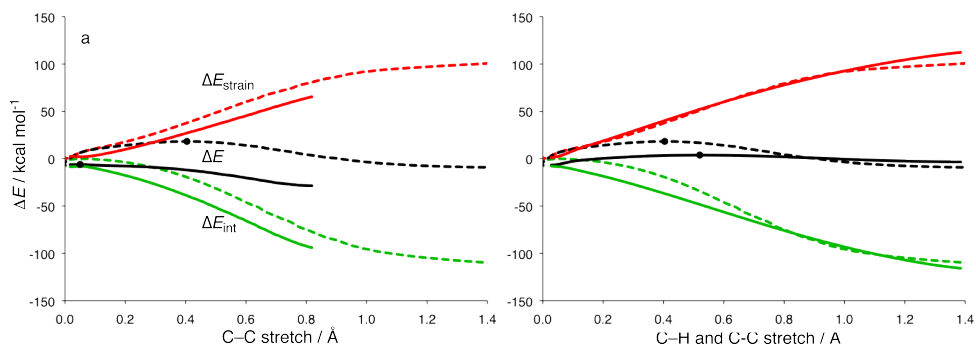


Figure 2.6 Activation strain analyses for oxidative insertion of Pd into (a) the ethane C–C (dashed lines) and cyclopropane C–C bond (solid lines); (b) the ethane C–C (dashed lines) and methane C–H bond (solid lines).

However, the activation strain analyses reveal more features responsible for the lower barrier. Besides the decrease in the strain energy, it appears that the strained system also allows for easier access of the palladium to the C–C bond. In the ethane oxidative insertion, the hydrogens on the methyl groups have to bend away in order to allow contact of palladium with the C–C bond. The interaction with the bond is thus greatly reduced due to steric shielding of the methyl groups. In cyclopropane this bending away of the hydrogens is already built into the geometry of the substrate, thus allow-

ing for stronger interaction early along the reaction path. Both effects can be clearly recognized in Figure 2.6a: both the strain and interaction terms are stabilized for oxidative insertion into cyclopropane (solid lines) as compared to the situation for ethane (dashed lines). The geometries in Figure 2.5 also illustrate this behavior quite clearly.

It is interesting to compare this with the corresponding oxidative insertion into the methane C–H bond, shown in Figure 2.6b. The methane C–H activation barrier is some 14 kcal mol⁻¹ lower despite the fact that this bond is much stronger than the C–C bond. The reason for the low C–H activation barrier is similar to that for the ethane C–C bond in cyclopropane: there is very little steric shielding on the side of the hydrogen, so interaction with the C–H bond proceeds easily, right from the beginning. At variance, the C–C bond is shielded on both ends by the methyl groups which prevent the palladium atom to approach and "electronically touch" the C–C bond for some time.^{32,99} Only after the C–C bond has been sufficiently elongated and the methyl groups have tilted away, there is room for the metal atom to come closer and build up overlap between its *d* orbitals and the $\sigma^*_{\text{C-C}}$ acceptor orbital. The initial delay in metal–substrate interaction ΔE_{int} in the case of the ethane C–C activation can be clearly seen in Figure 2.6b: compare green dashed (C–C) and green solid (C–H) curves.

2.5 Proper analysis along the reaction coordinate

The basis of the activation strain model is simple and appealing, and the result of an analysis can give clear and simple insights. With the help of the PyFrag program (section 2.8), it is easy to quickly apply analyses to a large number of reaction paths. However, one still has to be careful when performing an activation strain analysis, especially when the location along the reaction path becomes an issue.

It is important not to take the results of an analysis of a stationary point such as the TS at face value, as expressed in Figure 2.7. Furthermore, even along the entire reaction path one must be careful not to over-interpret the numerical results obtained from an 'as it is' analysis. The fact is that there will always be some geometrical relaxation effects that can differ between two different reactions, which can change the result of the analysis. This is related to the fact that, at each point on the reaction profile, the geometry is the result of a balance of opposing forces. And this balance can differ within a set of interacting systems. For example, larger steric interactions can push two molecular moieties apart, which can counter-intuitively lead to a case where

the actual Pauli repulsion between the moieties is smaller, due to the more pronounced separation of the moieties.

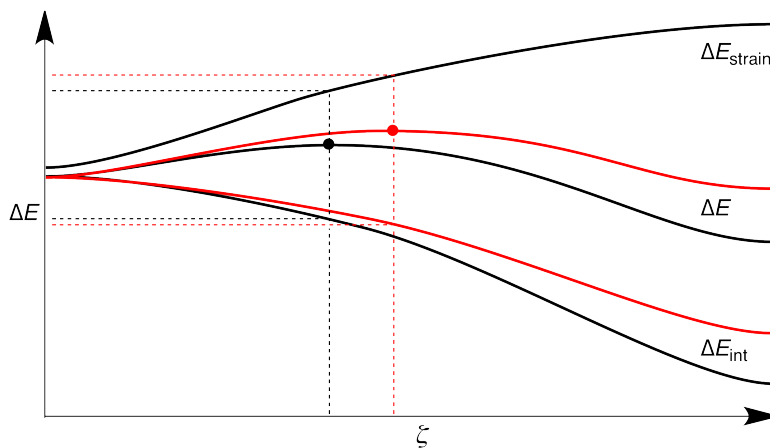


Figure 2.7 Schematic illustration of an activation strain analysis; the energy profile ΔE of two arbitrary reactions is decomposed along reaction coordinate ζ into the strain energy ΔE_{strain} of the increasingly deformed reactants plus the interaction energy ΔE_{int} between these reactants. The strain curves for the two reactions are identical. The fact that the PES and the transition state (indicated with a bullet) of the reaction represented with the red curves is higher than those of the reaction with the black curves is, in this example, entirely due to the weaker interaction in the case of the former. However, decomposition in the TSs alone would erroneously suggest the opposite (see dashed lines).

To circumvent the above problem, one can perform additional analyses with fixed geometries. Using this method, which is applied throughout this thesis, one can eliminate the changing geometrical effects and focus on the exact differences between the substrates or catalysts. After this step, which provides important insights, one can return back to the full reaction path analyses, which then becomes more understandable.

We have treated the aspect of geometrical relaxation in activation strain analyses in detail in a response to a paper by Fernández, Frenking and Uggerud.¹⁰⁰⁻¹⁰² In this paper¹⁰⁰ they conclude that not steric hindrance but reduced electrostatic attraction and reduced orbital interactions are responsible for the S_N2 barrier, in particular in the case of more highly substituted substrates, e.g., $F^- + C(CH_3)_3F$. We disagree with this conclusion, which is the result of neglecting geometry relaxation processes that are induced by increased Pauli repulsion in the sterically congested S_N2 transition state.¹⁰¹ Although these analyses do not focus on the oxidative insertion mechanism, the following hopefully will be an enlightening example of the potential pitfalls related to neglecting geometrical relaxation processes.

The paper in question proclaims the "Myths of steric hindrance" in connection with the reaction barrier associated with S_N2 substitution, i.e., $X^- + CH_3Y \rightarrow XCH_3 + Y^-$. Based on energy decomposition analysis of several S_N2 potential energy surfaces, FFU arrive at a new interpretation of the factors that govern the course of these reactions. In particular, they conclude that *"In contrast with current opinion, energy decomposition analysis shows that the presence of bulky substituents at carbon leads to the release of steric repulsion in the transition state. [...] It is rather the weakening of the electrostatic attraction, and in particular the loss of attractive orbital interactions, that are responsible for the activation barrier."* This conclusion of FFU is somewhat misleading since the geometrical relaxation processes were not considered. The latter are induced by an increasing steric (Pauli) repulsion, between nucleophile and substituents at the substrate, as the S_N2 reaction proceeds towards the sterically crowded, five-coordinate transition state. It is therefore crucial to be aware that the overall effect of steric hindrance (e.g., in equilibrium structures and in transition states) is contained not only in the steric or Pauli repulsion term but also in the changes in other energy terms that are caused by the aforementioned geometric relaxation processes.

In the first place, we have a look at the results of FFU.¹⁰⁰ They have partitioned the S_N2 reaction system into a dianionic fragment consisting of the nucleophile and the leaving group, $[X---Y]^{2-}$, plus a fragment consisting of the central CH_3^+ cation, and then analyze the interaction ΔE_{int} between these fragments along the S_N2 reaction coordinate. The work of FFU concludes with the observation that in the S_N2 transition state the interaction between $[X---Y]^{2-}$ and CH_3^+ has become less stabilizing because electrostatic attraction and bonding orbital interactions have become less stabilizing, *not* because the steric (Pauli) repulsion has become more destabilizing.

Although this observation is as such correct, it does, at variance to the interpretation of FFU, not imply a minor role for (let alone the absence of) steric hindrance. On the contrary, the observed behavior of the energy terms is the direct consequence of increased steric congestion in the five-coordinate S_N2 transition state. In that connection, we must ask the question, not addressed by FFU, *why* the Pauli repulsion decreases in the S_N2 transition state. After all, the latter is sterically more congested (five-coordinate C) than the reactant (four-coordinate C). All previous analyses¹⁰³⁻¹⁰⁵ point to the same conclusion: in the S_N2 transition state $[X-CH_3-Y]^-$, the five substituents around carbon are in direct steric contact. Pushing these substituents in a numerical experiment further together leads to a sharp increase in steric repulsion. Or, putting it the other way around, if the substituents are constrained to preserve the somewhat

shorter bond distances of the four-coordinate CH_3Y fragment while simultaneously forcing the reaction system of $\text{X}^- + \text{CH}_3\text{Y}$ along its $\text{S}_{\text{N}}2$ reaction coordinate, there is an enormous increase of the total energy and thus the reaction barrier because of a truly dramatic increase of the steric (Pauli) repulsion.

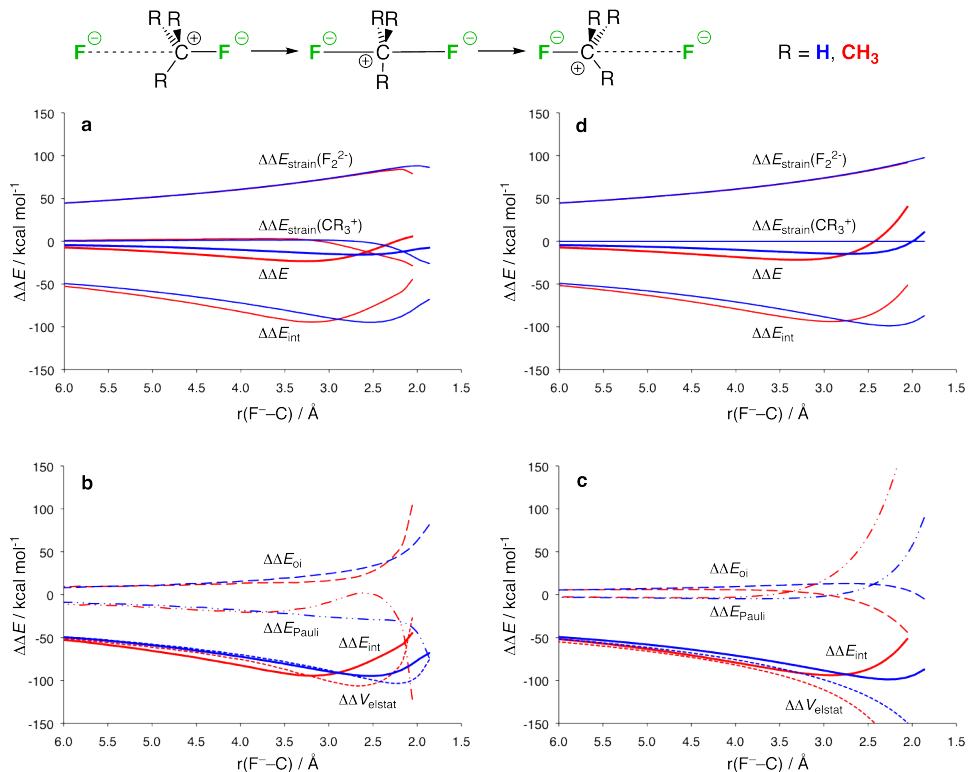


Figure 2.8 Analyses of the potential energy surfaces, $\Delta\Delta E$, for the $\text{S}_{\text{N}}2$ reactions of $\text{F}^- + \text{CH}_3\text{F}$ (blue curves) and $\text{F}^- + \text{C}(\text{CH}_3)_3\text{F}$ (red curves) along the internal reaction coordinate (a, b) and along a constrained reaction coordinate (c, d) projected onto the nucleophile $\text{F}^- - \text{C}$ distance, using the partitioning of FFU into an F_2^{2-} fragment interacting with a CR_3^+ fragment. Energies are computed at OLYP/TZ2P relative to the situation of separate reactants.

The earlier results are based on two ways of partitioning the reaction system: (i) into the original reactants;^{103,105} and (ii) into the central atom plus the ("box" of) five substituents.¹⁰⁴ The former approach is the activation strain model, which is particularly intuitive as it relates all energy changes along the reaction coordinate directly to the original reactants, i.e., without using an external standard. But also if we use the aforementioned partitioning of FFU into one dianionic fragment $[\text{X} \cdots \text{Y}]^{2-}$, consisting of both the nucleophile and leaving group, plus the cation CH_3^+ , we arrive at the same result. To this end, we have carried out new analyses at OLYP/TZ2P for two of the

reactions of FFU, namely, $F^- + CH_3F$ and $F^- + C(CH_3)_3F$, using the same approach as FFU (see Figure 2.8). Thus we follow the energy ΔE along the reaction coordinate given as $\Delta E = \Delta E_{\text{int}} + \Delta E_{\text{strain}} = \Delta E_{\text{int}} + \Delta E_{\text{strain}}(F_2^{2-}) + \Delta E_{\text{strain}}(CR_3^+)$, where ΔE_{int} is the interaction between F_2^{2-} and CR_3^+ ($R = H, Me$), $\Delta E_{\text{strain}}(F_2^{2-})$ is the repulsive interaction between F^- and F^- , and $\Delta E_{\text{strain}}(CR_3^+)$ is the deformation energy of CR_3^+ relative to the planar equilibrium geometry of this cation.

In Figure 2.8, energies are displayed along the S_N2 reaction path (constructed by a series of optimizations at constrained nucleophile–carbon distances) projected onto the separation $r(F^-C)$ between nucleophile F^- and substrate CR_3F ; these energies are taken relative to the situation of infinite separation. As we can see in Figure 2.8a, the reaction profile $\Delta\Delta E$ of $F^- + C(CH_3)_3F$ (red curves) features a somewhat deeper well for the reactant complex and a clearly higher barrier associated with reaching the transition state, as compared to that of $F^- + CH_3F$ (blue curves; see Figure 2.8a). Note that the correct value and shape of $\Delta\Delta E$ differs from the interaction $\Delta\Delta E_{\text{int}}$ because the strain terms are not zero and have the effect of somewhat reducing the barrier height. Nevertheless, it is the interaction $\Delta\Delta E_{\text{int}}$ that sets the trend for $\Delta\Delta E$ and causes a reaction barrier to occur. And the energy decomposition, in Figure 2.8b, reveals that $\Delta\Delta E_{\text{int}}$ becomes less stabilizing near the transition state because the electrostatic attraction $\Delta\Delta V_{\text{elstat}}$ and orbital interaction $\Delta\Delta E_{\text{oi}}$ get less stabilizing, not because of reduced Pauli repulsion $\Delta\Delta E_{\text{Pauli}}$ that indeed becomes less repulsive. This is also what FFU have found.

But *why* is Pauli repulsion reduced as a fifth substituent is approaching the central carbon atom? The answer is that there is in fact more Pauli repulsion at any given geometry of the substrate as the nucleophile is approaching. However, the substrate CR_3F reacts to the approach of this fifth substituent F^- through geometrical relaxation processes [mainly planarization of CR_3 and $C-F$ (leaving group) bond lengthening] which relieve this steric (Pauli) repulsion. Thus, a new equilibrium between repulsive and attractive forces (or energy components) is achieved in which the Pauli repulsion ΔE_{Pauli} drops even below its value in the isolated substrate. Note that this occurs at the expense of making the attractive terms ΔV_{elstat} and ΔE_{oi} less stabilizing. The observed weakening of the latter two is thus also a consequence of the geometric relaxation [in particular, the carbon– F (leaving group) bond lengthening] induced by the initially increased Pauli repulsion. The result is that $\Delta\Delta E$ is less destabilized than without such geometric relaxation but it is still higher in energy than in the absence of the nucleophile. Very recently, Schwarz and co-workers published an excellent discussion of this,

may be somewhat counterintuitive but quite general phenomenon that increasing the repulsion (or another parameter) in an equilibrium system may shift the equilibrium to a new situation in which this repulsion (or other parameter) adopts a smaller value.^{106,107}

The above picture emerges from numerical experiments and analyses in which we artificially suppress the geometric relaxation of the substrate which then retains the equilibrium of isolated CR_3F during the approach of the nucleophile (see Figure 2.8c). Under these circumstances, the Pauli repulsion $\Delta\Delta E_{\text{Pauli}}$ steadily increases as the nucleophile F^- approaches, and it "explodes" near the transition state. At the same time, the electrostatic attraction and bonding orbital interactions become more stabilizing, in particular close to the transition state. Note that these are the exact opposite trends if compared to the systems following the regular (unconstrained) $\text{S}_{\text{N}}2$ reaction paths (see Figure 2.8b). The reason is that by suppressing geometric relaxation, the C–R groups cannot bend away anymore and the leaving group cannot begin to leave a little in the transition state, leading to very close contacts and thus high Pauli repulsion. As a result, the corresponding constrained reaction profiles show dramatically increased fictitious barriers if compared to the unconstrained reaction profiles (compare Figure 2.8d with Figure 2.8a).

In this section we have shown that *increased steric congestion* around the five-coordinate central atom causes the barrier in the $\text{S}_{\text{N}}2$ reaction of $\text{F}^- + \text{CR}_3\text{F}$. There is more Pauli repulsion at any given geometry of the substrate if the fifth substituent (i.e., the nucleophile) approaches. Importantly, however, this increased Pauli repulsion causes the system to geometrically relax toward a new equilibrium between bonding and repulsive forces at which the Pauli repulsion is eventually less than in the original reactants, although at the expense of reduced electrostatic attraction and orbital interaction. The latter behavior should always be included to arrive at a physical understanding of the final emerging values of the decomposition analysis. Because of this, it is often necessary to include this type of ‘fictitious’ analysis presented in this section (and use throughout this thesis) to come to a full, complete picture and to explain why it adopts a particular equilibrium geometry. The final response by FFU¹⁰² explicitly argues against the inclusion of this type of analysis; we think the reasons stated here convincingly show their vital importance in the full activation strain analysis.

2.6 Choosing the reaction coordinate

It is of vital importance to choose the right reaction coordinate, on which to plot the results of the energy decomposition analysis as the reaction progresses. The choice of reaction coordinate, for any type of reaction, is critical for zooming in on the important stage of the reaction and for revealing the origin of trends along series of reactions. Some criteria for a good reaction coordinate are: (i) a large amplitude in coordinates that define the overall reaction, e.g., the C–X bond into which a metal oxidatively inserts; (ii) a large amplitude in the transition vector, i.e., the normal mode associated with a negative force constant that leads from the TS to the steepest descent paths; and (iii) preservation of this amplitude over a sufficiently long interval along the reaction path before and after the TS. In the case of the oxidative additions, the optimal choice is, as mentioned before, the C–X bond stretch of the activated bond in the substrate. In the following section we will put our choice of the reaction coordinate on a more solid basis by examining three perspectives on the reaction profiles (see Figure 2.9): (a) the IRC itself; (b, c) two different projections of the IRC on simple geometry parameters. In all cases, the reaction profiles run from the reactant complex at the left to the product at the right. The substrates used here, ethane C–C bonds with an increasing number of methyl group substituents, will be examined in more detail in Chapter 5.

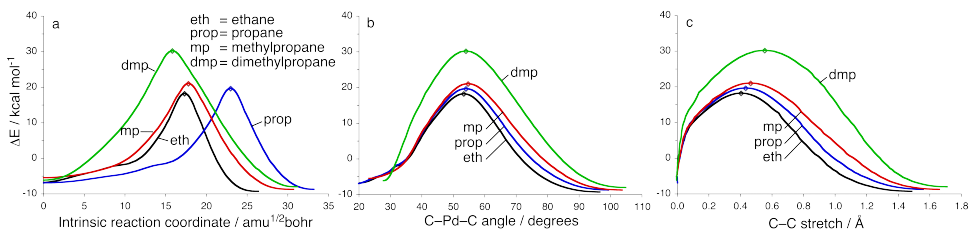


Figure 2.9 Comparison of three reaction coordinates for representing the PES of the oxidative insertion (OxIn) of Pd into the central C–C bond of ethane (black, eth), propane (blue, prop), methylpropane (red, mp) and dimethylpropane (green, dmp): (a) IRC distance (mass-weighted a.u.) starting from the reactant complex; (b) bond angle C–Pd–C (in degrees); (c) C–C bond stretch relative to substrate (in Å).

In Figure 2.9a, the reaction profiles are plotted as functions of the IRC itself as the reaction coordinate. Note that we display the progress of the reaction relative to the reactant complex (RC) and not, as is often done, relative to the transition state which technically is the starting point of an IRC calculation. The reason is that for our purpose, namely, understanding the progress of a reaction and the height of the barrier in

terms of the reactants, it is essential to take these reactants or the precursor complex as the point of reference. The reaction profiles based on the IRC as the reaction coordinate vary rather chaotically from one reaction to the other. This behavior can be explained by the geometry changes along the reaction path. For example, in the case of propane, the TS peak is shifted towards the product side, i.e., to a higher value of the reaction coordinate. The origin of this apparent "irregularity" is that one methyl group rotates freely over large parts of the reaction, thus creating a large coordinate distance in the IRC while influencing the total energy only very little. This also illustrates the main problem: the IRC traces *all* movements of all the nuclei in the reaction whether this is intrinsic to the actual process of bond breaking and insertion or just a derivative of the latter. Although there is some information to be gathered from these graphs they are not really suitable to catch (the trends in) the essence of the various reactions. A more detailed discussion of this issue can be found elsewhere.¹⁰⁸

Next, in our quest for reaction coordinates that uncover the systematic trends in the oxidative insertion process, we examine projections of the IRC onto simple geometry parameters. We recall that the reaction coordinate should have significant amplitude in (and correlate with) the IRC-defined reaction path, such that it is a reliable measure of the progress of the reaction. Also, the reaction coordinate should provide us with insight into when and how the underlying features in the electronic structure (e.g., metal–substrate donation and back-donation orbital interactions) are active and decisive in determining the shape of the PES, in particular, the geometry of the TS and its energy. Two geometry parameters emerge as good candidates for a reaction coordinate: (i) the C–Pd–C angle which increases as palladium approaches and the C–C bond expands; and (ii) (the stretch in) the C–C distance. This is of course not entirely unexpected in view of the fact that: (i) the C–C bond breaking is an essential geometrical deformation which defines the oxidative insertion reaction; and (ii) the C–Pd–C angle strongly correlates with the C–C distance on a large part of the PES.

Figure 2.9b shows the reaction profile as a function of the C–Pd–C angle as the reaction coordinate. It is immediately clear that the resulting reaction profiles (Figure 2.9b) behave much more systematically than in the previous representation. From ethane to propane to methylpropane, there is a systematic and gradual change in the reaction profiles: they all start more or less at the same point but become higher in energy along this series. Furthermore, the TS shifts stepwise to the right, i.e., to the product side. But the reaction profile for dimethylpropane is different, in particular at lower bond angles or, in other words, near the reactant complex. This is because palladium

coordinates in a η^3 manner to the C–H bonds of three different methyl groups of dimethylpropane, as compared to the η^2 coordination with ethane (see Figure 2.10), such that it is from the beginning closer to the C–C bond into which it inserts. Therefore, it has to reorient (and "travel") less in order to reach the TS, as can also be seen in the reaction profile based directly on the IRC as the reaction coordinate (see Figure 2.9a). The C–Pd–C bond angle is a reaction coordinate that magnifies differences in the reactant-complex region, i.e., in early stages of the reaction. The height of the barrier is however determined beyond the RC, at a more advanced stage of the reaction.

Figure 2.9c shows the reaction profile as a function of the C–C bond stretch (relative to the reactants) as the reaction coordinate. The reaction profiles vary very systematically from one reaction to another one. Now, they all start at the same point (in the reactants, the C–C bond is not yet stretched) and there is both a systematic increase in barrier height and a systematic shift to the right of the transition states. The systematic increase in energy and position along the C–C reaction coordinate is intimately connected with how the strain energy of the substrate varies and how the bonding capabilities of the substrate with the metal evolve. This has been previously pointed out in an Activation Strain analysis of C–H and C–C bond activation, and explains the very systematic and smooth change in reaction profiles along the four reactions. A more detailed examination of the geometrical changes along the C–C reaction coordinate shows that this reaction coordinate magnifies the region along the IRC reaction path where the TS is located, i.e., where the height of the barrier is determined, whereas the very early stage near the RC is more compressed. This is due to the fact that during the first part of the reaction, the C–C bond does not change much, whilst the geometry of the reactant complex can change significantly due to migration of the metal from the optimal coordination site towards the point where it starts to insert into the C–C bond.

Next, we compare the oxidative insertion reactions of palladium into the C–H, C–C, C–F, and C–Cl bonds in methane, ethane, fluoromethane and chloromethane, respectively. The resulting PESes are again displayed as a function of the IRC as well as projections thereof onto the C–Pd–X

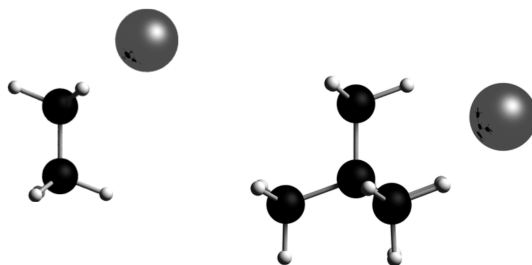


Figure 2.10 η^2 and η^3 coordination in reactant complexes of Pd with ethane and dimethylpropane.

angle and onto the C–X bond stretch relative to the reactant complex (see Figure 2.11). In addition to the energy of the reaction system (i.e., the PES), we plot here also the VDD atomic charge¹⁰⁹ of palladium and the population of the substrate's C–X anti-bonding $\sigma^*_{\text{C-X}}$ acceptor orbital that becomes occupied in the course of the reaction.

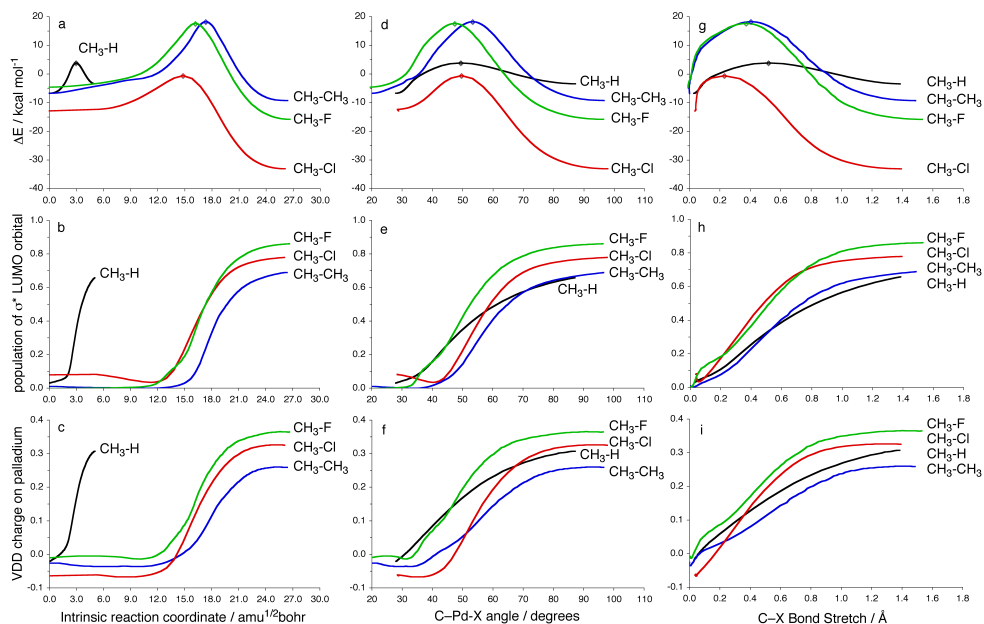


Figure 2.11 Comparison of three reaction coordinates for representing the PES and other properties of the oxidative insertion of Pd into the methane C–H (black), ethane C–C (blue), fluoromethane C–F (green) and chloromethane C–Cl bonds (red): (a, b, c) IRC distance (mass-weighted a.u.) starting from the reactant complex; (d, e, f) bond angle C–Pd–X (in degrees); (g, h, i) C–X bond stretch relative to substrate (in Å). The plots show: (a, d, g) the PES; (b, e, h) the population of the $\sigma^*_{\text{C-X}}$ anti-bonding LUMO; (c, f, i) VDD charge on the Pd atom.

The two main features in the metal–substrate bonding mechanism are, as has been briefly mentioned above: (i) the *back-donation* of charge from the palladium 4*d* orbital into the $\sigma^*_{\text{C-X}}$ anti-bonding orbital of the C–X bond that is being broken; and (ii) the donation of the $\sigma_{\text{C-X}}$ bonding orbital into the 5*s* orbital of palladium. Charge transfer and orbital populations are consequently quantities that are associated with the extent of progress of the oxidative insertion reaction on the level of the electronic structure. The increasing population of the anti-bonding orbital shows in essence the bond breaking process. All these quantities are in the first place dependent on the (stretch in) C–X distance in the substrate. This is nicely illustrated in Figure 2.11 which shows plots of palladium VDD atomic charges and $\sigma^*_{\text{C-X}}$ anti-bonding orbital populations

for each of the reaction coordinates. It is easily seen that the C–X bond stretch allows us to represent the bond breaking process in the most smooth and consistent manner (see Figure 2.11g-i). Choosing the IRC on the horizontal axis again leads to more chaotic variation along the different C–X bonds because the progress of the reaction, i.e., the way in which the energy, atomic charge and orbital population change, is directly linked to the C–X stretch and not to all the other geometry parameters that contribute to the IRC (see Figure 2.11a-c). The C–Pd–X bond angle yields again a more smooth description (see Figure 2.11d-f) but the systematics of the bonding mechanisms underlying the reaction in progress come out best in the plots that are based on the C–X stretch.

Furthermore, the C–X bond stretch is the main (but not the only!) determinant for the strain energy $\Delta E_{\text{strain}}(\xi)$ of the increasingly deformed substrate. Together with the metal–substrate interaction $\Delta E_{\text{int}}(\xi)$, this determines the reaction profile or potential energy surface $\Delta E(\xi) = \Delta E_{\text{strain}}(\xi) + \Delta E_{\text{int}}(\xi)$ along the reaction coordinate ξ . Thus, the C–X stretch emerges as the optimal choice for representing the reaction profile and underlying features in the electronic structure for oxidative insertion reactions.

2.7 Transition vector as approximation to IRC

Vibrational analysis reveals that, for the oxidative insertion reactions the bond stretching (for example the C–C stretch) also has a large amplitude in the transition vector of our oxidative insertion reactions, i.e., the normal mode associated with a negative force constant that leads from the saddle point to the steepest descent paths. Thus, for very large model reaction systems for which IRC calculations become prohibitively expensive (or just impossible), following the path defined by the transition vector (TV) may be used as an approximation of that IRC in the region "around the TS". In fact, we find that the TV path approximates the IRC path very well over a sufficiently long interval to be useful for representing and analyzing the reaction profile of our oxidative insertion reactions. Numerical experiments shows that the reaction profile of oxidative insertion reactions (as function of the C–C stretch and the C–Pd–C angle as the reaction coordinates) generated on the basis of the TV essentially coincides with that generated on the basis of the full IRC over an interval of about 0.5 Å of the C–C reaction coordinate around the TS (see Figure 2.12a and Figure 2.12b). We designate this procedure as the TV-IRC approximation. Since TV-IRC calculations typically require around ten single point calculations only, the computational cost is dramatically decreased as compared to the corresponding partial IRC (let alone a full

IRC), which would then require several constrained geometry optimizations in a stage of the reaction that goes with relatively strong structural reorganization on a shallow saddle region of the PES.

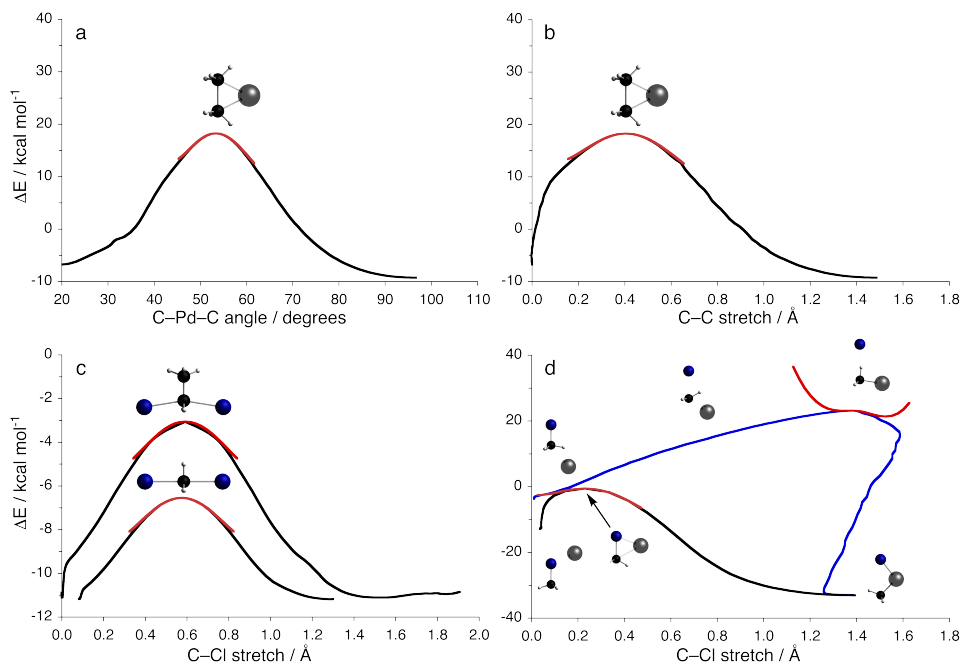


Figure 2.12 Comparison of reaction profiles based on the IRC (black/blue, full curves) and TV-IRC (red, partial curves): (a) OxIn of Pd + ethane with C–Pd–C angle as reaction coordinate; (b) OxIn of Pd + ethane with C–C stretch as reaction coordinate; (c) S_N2 reactions of Cl⁻ + CH₃Cl and Cl⁻ + CH₃CH₂Cl with the C–Cl stretch as reaction coordinate; (d) oxidative insertion versus S_N2 mechanism for OxIn of Pd + CH₃Cl (note the breakdown of the TV-IRC approximation in the case of the latter S_N2 mechanism; see text).

Interestingly, the TV-IRC reaction profile agrees over a longer interval with the IRC reaction profile if it is represented as a function of the C–C stretch (agreement over roughly one third of the entire reaction interval!) than if it is represented as a function of the C–Pd–C angle (agreement over roughly one fifth of the entire reaction interval, compare Figure 2.12a with Figure 2.12b). This is consistent with the fact that the C–C stretch plays a more important role near the TS and that the reaction profile as a function of this reaction coordinate zooms in on the region around the TS. This makes the TV-IRC approach very useful to do a relatively quick and computationally easy analysis on the most important part of the reaction path. Also, in this way one can use this part of the reaction path for activation strain analyses. This eliminates the difficulties

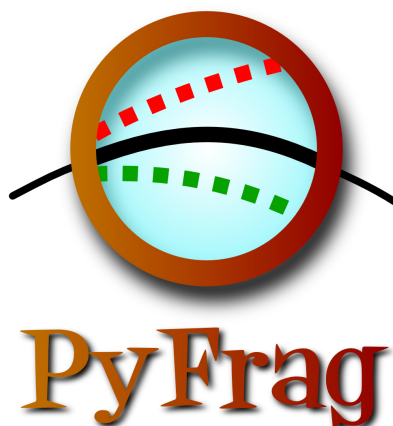
of the changes of the position of TS along the reaction coordinate, when an entire IRC calculation is not feasible.

We have also tested the TV-IRC approximation for other classes of reactions. In Figure 2.12c, we show the reaction profiles for the S_N2 reactions of $Cl^- + CH_3Cl$ and $Cl^- + CH_3CH_2Cl$ as functions of the C–Cl (i.e., carbon–leaving group) stretch. Again, the TV-IRC-based reaction profiles coincide with the IRC-based ones over a range of some 0.5 Å of the reaction coordinate, that is, roughly one third of the entire reaction interval.

Finally, we also wish to stress the situations in which the TV-IRC approximation breaks down. This happens whenever the character of the geometrical deformations changes quickly and/or drastically along the reaction path. Typically, this happens when different elementary steps merge into one reaction step. An example is the alternative S_N2 mechanism for oxidative addition of $Pd + CH_3Cl$. For the oxidative insertion mechanism, as can be seen in Figure 2.12d, the TV-IRC-based reaction profile again nicely coincides with the IRC-based one. At variance, for the alternative S_N2 mechanism, the TV-IRC-based reaction profile is valid only in very narrow interval around the TS. The reason is that the TV is mainly the migratory movement of the expelled chloride leaving group that is hydrogen bonding to one of the C–H bonds.⁸³ But just before this TS, there is a real S_N2 stage in which the IRC has a large component of the characteristic Pd–C–Cl asymmetric stretch in combination with the methyl umbrella mode while directly after the TS, the S_N2 reaction path merges into the regular oxidative insertion path.

2.8 PyFrag: streamlining your reaction path analysis!

PyFrag⁸⁶ is a program designed to make the analysis of a PES with the Amsterdam Density Functional (ADF) package more user-friendly by performing and bringing together all the above-mentioned ADF calculations, for each point on the grid of geometries associated with the PES, in combination with extracting, integrating and post processing the relevant information. Thus, PyFrag de facto extends the fragment-orientated energy decomposition analysis as implemented in the ADF package



from treating single-points to examining entire potential energy surfaces. The program is written in the popular and highly portable Python programming language. The name PyFrag is derived from **P**ython and **F**ragment analysis.

PyFrag is intended as a “wrap-around” for ADF to facilitate fragment analysis calculations along a set of geometry points. It is controlled by an ADF input file augmented with extra statements understandable by PyFrag. The ADF input script is then used as a basis to construct and execute the necessary ADF calculations. The desired molecular coordinates can be read from the result files of intrinsic reaction coordinate (IRC) or (one- or multidimensional) linear transit (LT) calculations. But, reading Cartesian coordinates from an xyz-file containing a series of multiple geometrical structures is also possible, which can be useful in order to scan a multidimensional PES in a series of single point calculations. PyFrag can also generate a series of single-point calculations by introducing variable coordinates within a chosen molecular geometry. The latter facilitates a quick scan and analysis (!) of the PES along one or more coordinates. This was, for example, done in the bonding analyses of chapter 6.

As might be clear, a lot of information can be extracted from the ADF fragment analysis calculations, the principle data being often the energy decomposition terms. These terms will be printed by default into a text-data file. Optional data can be printed for each point along the PES, such as atomic charges,¹⁰⁹ orbital populations, orbital energies, and orbital overlaps. All these quantities can be valuable when trying to understand the behavior of a PES, especially if their behavior as a function of the reaction coordinate is important, which makes the transparent way in which PyFrag structures this data very attractive. The data file can be very easily used in various data plotting programs.

Python is a powerful and highly transferable script language and running PyFrag on various operating systems is easily achieved (given that there is a local copy of the ADF-package present, of course). Besides Python, no extra modules or programs need to be installed to run PyFrag. The output generated by PyFrag can be easily imported into programs such as Excel. It is also possible to generate a file that can be read by gnuplot, an often-used and free data-plotting program. The program, released as PyFrag2007.01, is freely available. The distribution includes the Python source code, documentation and some example scripts and can be downloaded from <http://www.few.vu.nl/~bickel>.

3 The steric nature of the bite angle

Inspired by:

Willem-Jan van Zeist, Ruud Visser, F. Matthias Bickelhaupt

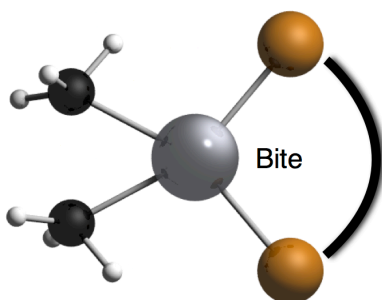
Chem. Eur. J. **2009**, *15*, 6112

Willem-Jan van Zeist, F. Matthias Bickelhaupt

Dalton Trans. **2011**, *40*, 3028

Abstract

The bite angle (ligand–metal–ligand angle) is known to greatly influence the activity of catalytically active transition-metal complexes towards bond activation. Here, we have explored how and why the bite angle has such effects in a wide range of prototypical C–X bonds and palladium complexes. We elucidate the steric nature of the bite angle where smaller bite angles decrease steric interactions and thus reduce barriers. A smaller bite angle makes more room for coordinating a substrate by bending away the ligands. In this light also the ‘building in’ of the catalyst deformation into already strained chelating ligands, which avoids the building up of strain energy, is an important energetic factor. Our model reactions cover the substrates H₃C–X (with X = H, CH₃, Cl) and this series is expanded with, among others, the model catalysts, Pd[PH₂(CH₂)_nPH₂] (with n = 2 - 6) and Pd[PR₂(CH₂)_nPR₂] (n = 2 - 4 and R = Me, Ph, *t*-Bu, Cl), Pd(PH₃)X⁻ (X = Cl, Br, I), as well as palladium complexes of chelating and non-chelating N-heterocyclic carbenes. The wide range of model ligands further consolidates the steric picture by revealing its occurrence in this broader range, but also provides insight into competing electronic factors due to changes in the ligands.



3.1 Introduction

The reaction barrier of oxidative insertions is well known to depend on the ligand–metal–ligand angle, the so-called bite angle (see Figure 3.1).^{110,111} Also for the reverse reaction of reductive elimination the bite angle can play a role.^{112,113} Many pioneering studies have been under-

taken in order to understand how exactly reaction barriers are affected by this and related structural parameters of the catalytically active complex.^{114–124} It is commonly accepted that the effect of the bite angle on the reaction barrier of, for example, C–X bond activation, originates from an electronic factor.

According to this electronic model, the transition state (TS) is stabilized by donor–acceptor interactions from metal d orbitals (specifically, the " $4d_{\pi}$ " orbital, see Figure 3.2) to the substrate σ^*_{C-X} , which becomes more stabilizing as the metal–ligand d hybrid orbital is pushed up in energy, at smaller bite angles.^{35–38} Although the rise in energy of the d orbital can be indeed observed in

calculations, there has been as of yet no direct evidence that it is really this phenomenon that causes the more stabilizing catalyst–substrate interaction at smaller bite angles. In this chapter, the electronic picture of the bite-angle effect is challenged. It will show that mainly steric effects are responsible for the lower oxidative-insertion barrier in the case of catalyst complexes with smaller bite angles. We put this finding on a broad basis with a number of different reactions and provide detailed bonding analyses to elucidate the nature of bite-angle effect. We also connect these analyses to the activation strain of the catalytic compound, which on itself is dependent on the carbon backbone in chelating ligands. Also, we will investigate the steric nature of the related ‘twist angle’ (see Figure 3.1).^{125,126}

We have investigated methane C–H, ethane C–C and chloromethane C–Cl bond activation by oxidative insertion (OxIn) of a variety of model catalysts. The model catalysts are based on Pd, Pd[PH₂(CH₂)_nPH₂] ($n = 2 - 6$, denoted as Pd[P_nP]), which enable us to explore a wide variety in bite angles, ranging from 98° to 156° along $n = 2 - 6$ (see Figure 3.3). The chapter can be divided into a number of topics: (i) through

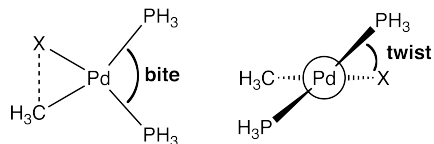


Figure 3.1 Bite angle (left) and twist angle (Newman projection, right) in the transition state geometry of an oxidative insertion of Pd(PH₃)₂ into a H₃C–X bond.

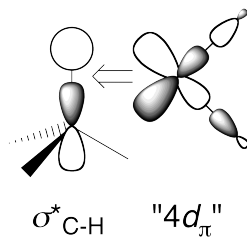


Figure 3.2 Donation from " $4d_{\pi}$ " into empty σ^*_{C-X} .

detailed catalyst–substrate bonding analyses as a function of bite and twist angle and its connection to the catalyst strain; (ii) variation of steric bulk on the catalysts, $\text{Pd}[\text{PR}_2(\text{CH}_2)_n\text{PR}_2]$ ($n = 2 - 4$ and $\text{R} = \text{Me}, \text{Ph}, t\text{-Bu}$), to see how sterically demanding groups on the phosphine ligands compare with the intrinsic steric effect of simple phosphine ligands; (iii) halogen substituent effects on the phosphine ligands; (iv) the effect of an additional anionic halide coordinating to metal and/or the phosphine ligands; (v) palladium complexes of chelating and non-chelating N-heterocyclic carbenes; and (vi) solvent effects for the range of model catalysts Pd , $\text{Pd}(\text{PH}_3)_2$ and $\text{Pd}[\text{PnP}]$ with $n = 2 - 6$.

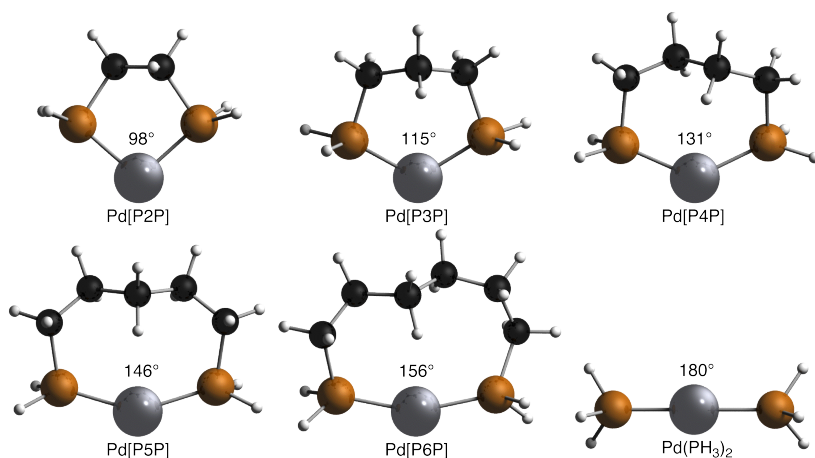


Figure 3.3 $\text{Pd}[\text{PnP}]$ ($n = 2 - 6$) and $\text{Pd}(\text{PH}_3)_2$ catalysts with bite angles (in degrees).

3.2 Stationary points

In the following, we will first focus on oxidative addition to plain palladium diphosphine complexes. After a thorough analysis of the bite and twist angle effects we will continue with ligand substituent effects. Table 3.1 shows the

results of our calculations for the simple model phosphine ligand palladium complexes. The oxidative insertion (OxIn) reactions proceed in principle from the reactants $\text{PdL}_2 + \text{CH}_3\text{X}$ (R), via a reactant complex (RC), to the transition state (TS) and, finally, the product (P). Along the reaction path, the C–X bond is progressively stretched and, finally, fully dissociates. This is illustrated in Figure 3.4 which shows the stationary points for OxIn of palladium into the methane C–H bond. Unlike bare pal-

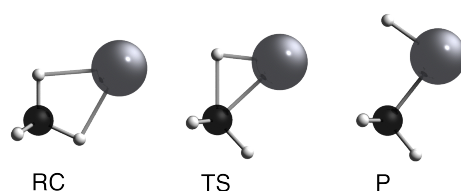


Figure 3.4 Stationary points for the OxIn of palladium into the methane C–H bond.

ladium, the chelate complexes Pd[PnP] and Pd(PH₃)₂ form essentially no stable reactant complex with methane and ethane (except Pd[P2P] which binds very weakly) and only weakly bound ones with chloromethane, via Pd–Cl coordination

Table 3.1 Reaction profiles for oxidative insertion (OxIn) of [Pd] into the H₃C–X bonds. Shown are C–X bond distances (in Å) and energies (kcal mol⁻¹) relative to reactants.^a Values in parenthesis include water solvent effects as obtained by the COSMO method.

		RC			TS			P		
		C–X	ΔE		C–X	ΔE^\ddagger		C–X	ΔE	
H ₃ C–H	Pd	1.123	-6.7	(-9.0)	1.616	3.9	(-0.6)	2.479	-3.4	(-8.3)
	Pd[P2P]	1.108	-1.3	(-2.6)	1.704	18.6	(14.0)	2.473	12.6	(3.3)
	Pd[P3P]	1.102	-0.5	(-1.3)	1.691	22.3	(18.2)	2.479	15.7	(7.0)
	Pd[P4P]	1.097	-0.5	(-1.6)	1.701	25.7	(22.9)	2.453	19.6	(12.5)
	Pd[P5P]	1.096	-0.1	(-1.4)	1.697	29.2	(27.0)	2.437	23.1	(16.8)
	Pd[P6P]	1.096	~0	(~0)	1.705	32.1	(31.0)	2.423	26.4	(21.7)
	Pd(PH ₃) ₂	1.096	~0	(~0)	1.725	32.2	(31.6)	2.432	27.1	(22.8)
H ₃ C–CH ₃	Pd	1.540	-6.8	(-9.0)	1.945	18.3	(15.4)	3.025	-9.3	(-9.9)
	Pd[P2P]	1.541	-1.7	(-3.2)	2.073	38.4	(36.2)	2.861	11.3	(3.7)
	Pd[P3P]	1.540	~0	(~0)	2.078	43.1	(41.2)	2.857	14.3	(7.1)
	Pd[P4P]	1.540	~0	(~0)	2.090	46.3	(45.6)	2.838	18.7	(12.9)
	Pd[P5P]	1.540	~0	(~0)	2.094	49.5	(49.5)	2.825	22.4	(17.6)
	Pd[P6P]	1.540	~0	(~0)	2.107	51.5	(52.3)	2.829	26.0	(22.6)
	Pd(PH ₃) ₂	1.540	~0	(~0)	2.107	51.3	(52.6)	2.836	26.4	(23.0)
H ₃ C–Cl	Pd	1.862	-12.9	(-15.2)	2.054	-0.6	(-2.6)	3.221	-33.1	(-40.0)
	Pd[P2P]	1.856	-6.4	(-7.6)	2.206	14.3	(12.2)	3.175	-27.1	(-41.8)
	Pd[P3P]	1.849	-3.3	(-4.4)	2.217	18.5	(16.1)	3.183	-25.1	(-38.1)
	Pd[P4P]	1.839	-1.4	(-1.6)	2.227	21.7	(20.6)	3.174	-20.3	(-32.2)
	Pd[P5P]	1.828	-0.9	(-1.6)	2.249	25.1	(24.3)	3.191	-17.9	(-27.6)
	Pd[P6P]	1.829	-1.1	(-1.5)	2.240	26.2	(25.4)	3.151	-13.3	(-24.6)
	Pd(PH ₃) ₂	1.828	-0.5	(-1.2)	2.250	27.1	(27.3)	3.148	-11.6	(-20.6)

^a [PnP] = [PH₂(CH₂)_nPH₂]. Reactant complexes essentially unbound (by less than -0.1 kcal mol⁻¹) are indicated as ~0.

A number of general trends can be observed in Table 3.1. Both, the endothermicity and barrier height increase from Pd, along the series Pd[P2P] to Pd[P6P] and Pd(PH₃)₂. This is, in part, caused by a weakening of the catalyst–substrate interaction from bare to coordinated palladium, as suggested by the concomitant loss of stability of the reactant complexes. Our activation strain analyses do confirm this but they also show that a different, steric mechanism mainly responsible for this trend along the various model catalysts. Furthermore, barrier heights increase for all model catalysts as one goes from C–Cl to C–H to C–C activation (see Figure 3.5 for representative TS structures), which was discussed in detail already previously, but mainly for the inser-

tion of uncoordinated Pd atoms.⁸³ Here we find that solvent effects in aqueous solution do not lead to any significant change in the above trends (see Table 3.1). Solvation only causes a slight stabilization of the stationary points and this solvation stabilization increases as the reaction, and thus the Pd–CH₃ and Pd–X charge separation, progresses. Thus, we can treat the influence of solvation effects as a mild perturbation on the gas-phase results, and we will base our analyses on these gas-phase calculations.

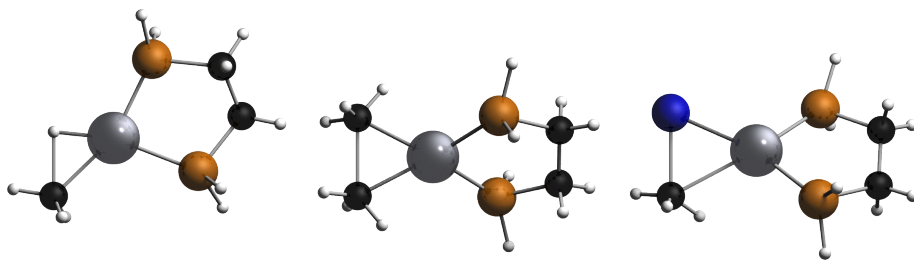


Figure 3.5 TS geometries for insertion of Pd[P2P] into C–H, C–C, and C–Cl bonds (TS geometries for other Pd[PnP] are similar).

3.3 Bite and twist angle

Table 3.2 shows the activation strain analysis at the transition states. In all cases, there is a pronounced correlation between an increase of the bite angle in the model catalyst (values in parentheses in Table 3.2) and an increase in reaction barrier ΔE^\ddagger as well as in the twist angle. Thus, Pd(PH₃)₂ has both, the largest bite angle, 180°, and the highest barrier, whereas this barrier decreases monotonically as the number of methylene units in the model catalyst's bidentate ligand shrinks from $n = 6$ to 2 and forces the bite angle down to 98°. As the bite angle decreases, also the twist angles in the transition state geometries of the C–C and C–Cl insertion reactions decrease. All C–H transition states are planar, see for example Figure 3.5.

The main source of the barrier rise from Pd to Pd(PH₃)₂ insertion is, in all cases, a steric mechanism. This shows up in the increased activation strain $\Delta E_{\text{strain}}^\ddagger$ (see Table 3.2). For example, from Pd to Pd(PH₃)₂ + methane, the activation strain terms $\Delta E_{\text{strain}}^\ddagger[\text{substr}]$ and $\Delta E_{\text{strain}}^\ddagger[\text{cat}]$ increase by some 10 and 17 kcal mol⁻¹, respectively, whereas the catalyst–substrate interaction $\Delta E_{\text{int}}^\ddagger$ is weakened by less than 1 kcal mol⁻¹. Together, this yields the observed increase of the overall barrier by some 28 kcal mol⁻¹ (from 3.9 to 32.2 kcal mol⁻¹). The strain of the methane substrate mainly stems from C–H bond expansion. The strain of the Pd(PH₃)₂ model catalyst is generated nearly exclusively through the bending of the phosphine ligands, away from the substrate. This causes the P–Pd–P angle to decrease from 180° in the free Pd(PH₃)₂ complex to

108° in the TS for insertion into the methane C–H bond. The barrier for the Pd[P2P] insertion, however, lies significantly lower, at 18.6 kcal mol⁻¹. This is mainly due to a sharp decrease of $\Delta E_{\text{strain}}^{\ddagger}[\text{cat}]$ to 6.0 kcal mol⁻¹, because the P–Pd–P bite angle changes far less, as it goes from 98° in the free Pd[P2P] to 85° in the TS.

Table 3.2 Geometry (in Å, deg) and activation strain analysis of transition states (in kcal mol⁻¹) for Pd-induced C–X bond activation.^a

		bite ^b	twist	C–X	$\Delta E_{\text{int}}^{\ddagger}$	$\Delta E_{\text{strain}}^{\ddagger}[\text{substr}]$	$\Delta E_{\text{strain}}^{\ddagger}[\text{cat}]$	ΔE_{\ddagger}
H ₃ C–H	Pd	- (-)	-	1.616	-48.4	52.2	0.0	3.9
	Pd[P2P]	85 (98)	2	1.704	-48.4	61.0	6.0	18.6
	Pd[P3P]	95 (115)	0	1.691	-46.7	59.9	9.0	22.2
	Pd[P4P]	103 (131)	2	1.701	-46.3	60.9	11.0	25.7
	Pd[P5P]	109 (146)	2	1.697	-45.6	60.6	14.2	29.2
	Pd[P6P]	119 (156)	1	1.705	-44.5	61.2	15.3	32.1
	Pd(PH ₃) ₂	108 (180)	0	1.725	-47.8	63.3	16.7	32.2
H ₃ C–CH ₃	Pd	- (-)	-	1.945	-19.6	37.9	0.0	18.3
	Pd[P2P]	87 (98)	49	2.073	-16.7	50.7	4.3	38.4
	Pd[P3P]	97 (115)	48	2.078	-15.1	51.4	6.8	43.1
	Pd[P4P]	105 (131)	49	2.090	-14.6	52.6	8.3	46.3
	Pd[P5P]	115 (146)	56	2.094	-13.7	52.8	10.5	49.5
	Pd[P6P]	126 (156)	62	2.107	-13.3	53.6	11.2	51.5
	Pd(PH ₃) ₂	113 (180)	56	2.107	-15.8	53.7	13.4	51.3
H ₃ C–Cl	Pd	- (-)	-	2.054	-10.5	9.9	0.0	-0.6
	Pd[P2P]	89 (98)	43	2.206	-9.1	20.3	3.1	14.3
	Pd[P3P]	101 (115)	48	2.217	-7.7	21.5	4.6	18.5
	Pd[P4P]	111 (131)	52	2.227	-6.7	22.7	5.8	21.7
	Pd[P5P]	128 (146)	72	2.249	-6.2	25.4	5.9	25.1
	Pd[P6P]	137 (156)	88	2.240	-5.0	25.8	5.3	26.2
	Pd(PH ₃) ₂	123 (180)	68	2.250	-7.6	25.6	9.1	27.0

^a [PnP] = [PH₂(CH₂)_nPH₂]. ^b Bite angle in TS and, in parentheses, in isolated PdL₂.

Numerical experiments show that the energetically unfavorable geometrical deformation of the catalyst along the insertion process occurs in reaction to the even more destabilizing steric (Pauli) repulsion that would be experienced if the catalyst fragment would retain its linear geometry during the approach to the substrate. Thus, using the various TS geometries of Pd(PH₃)₂ inserting into the C–H, C–C and C–Cl bonds, we have analyzed the catalyst–substrate interaction ΔE_{int} as a function of varying the P–Pd–P angle, under the constraint that all other geometry parameters are kept frozen to their value in the TS stationary point. The results are shown in Figure 3.6. Note that this analyses focuses on how and why the catalyst–substrate interaction changes during a well-defined but fictitious deformation, leaving out the associated strain energy

in the catalyst which one would have to add in order to arrive at the total energy. Figure 3.6 shows that the interaction ΔE_{int} becomes less stabilizing if the P–Pd–P angle is increased. Interestingly, this is so because of increased steric Pauli repulsion ($\Delta E_{\text{Pauli Total}}$ in Figure 3.6). It is not because of a weakening in the orbital interaction ΔE_{oi} . The latter would be expected if one proceeds from the traditional electronic model for bite-angle effects, owing to the reduced back-donation from the metal "4d π " orbital to the substrate $\sigma^*_{\text{C-X}}$ orbital (see Figure 3.7, left).³⁵⁻³⁸ This decrease in back-donation can be easily seen in population analyses; for example the $\sigma^*_{\text{C-H}}$ population drops from 0.54 to 0.41 from 60 to 180 degrees bite angle; not particularly large for such a sizeable geometrical change. The orbital overlaps have a small role in this, which do not correlate directly with the bite angle and vary little.

However, Figure 3.6 clearly shows unexpected behavior of the orbital interaction: ΔE_{oi} becomes *more stabilizing* (not less stabilizing) as the P–Pd–P angle approaches 180°. The reason is that more severe Pauli repulsion also induces secondary stabilizing relaxation effects in ΔE_{oi} that, here, dominate and thus mask the effect of a weakening in the (first-order) back-donation. Preliminary calculations on non-bonding systems show this relaxation of the orbital interaction falls within the range associated with this level of increased repulsion. This analysis was done by performing a number of energy decomposition analyses on pairs of approaching noble gasses, which indeed show a secondary stabilization of orbital interactions in the region of 20 to 30 kcal mol⁻¹ for a Pauli repulsion that increases around 150 kcal mol⁻¹.

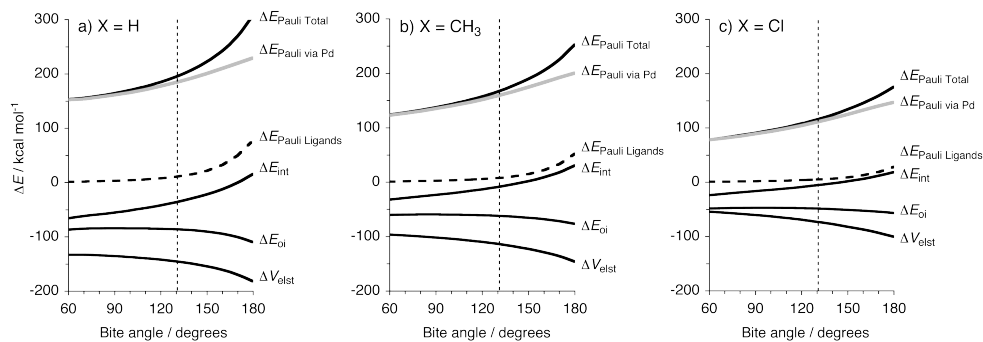


Figure 3.6 Energy decomposition analysis of the catalyst–substrate interaction ΔE_{int} as a function of the bite angle, with all other geometry parameters kept frozen to their values in the TS structures for Pd(PH₃)₂ insertion into three different H₃C–X bonds (see text).

We have also estimated to which extent the trend in total Pauli repulsion is determined: (i) directly by overlap between the ligands and the substrate; and (ii) indirectly by ligand-induced changes in the palladium electronic structure. To this end, the

analyses have been repeated for the exact same set of geometries and deformations of the reaction system, however, with the palladium atom removed. Now, the remaining Pauli repulsion stems entirely from direct steric contact between ligands and substrate ($\Delta E_{\text{Pauli Ligands}}$ in Figure 3.6). The difference $\Delta E_{\text{Pauli via Pd}} = \Delta E_{\text{Pauli Total}} - \Delta E_{\text{Pauli Ligands}}$ is an estimate of the Pauli repulsion that occurs between the palladium atom in the catalyst complex and the substrate. The steric (Pauli) repulsion $\Delta E_{\text{Pauli Ligands}}$ between ligands and substrate is approximately zero for small bite angles. But, at bite angles larger than 130 degrees, $\Delta E_{\text{Pauli Ligands}}$ suddenly increases rapidly. This is when the ligands come "too" close to the substrate and cause direct steric repulsion. Interestingly, this result nicely matches the experimental observation that many catalyst complexes have bite angles below 130°. ¹⁰⁴ The more continuous increase estimated for $\Delta E_{\text{Pauli via Pd}}$ is related to the fact that a "4d_σ" orbital is pushed up in energy and better overlaps with the occupied substrate $\sigma_{\text{C-X}}$ bond orbital as the bite angle decreases (e.g., for C–H activation, the overlap increases from 0.02 to 0.27 if one goes from 60° to 180°).

As mentioned above, the tendency of the twist angle to deviate in the TS from 0° becomes stronger as the bite angle in the catalyst complex increases (see Table 3.2). The trend is most pronounced in the case of oxidative insertion into the C–Cl bond. Thus, in the reactions of Pd[PnP] + CH₃Cl, along n = 2 - 6, the twist angle in the TS increases from 43° to 88° while the bite angle in the isolated catalyst complex increases from 98° to 156° (see Table 3.2: in the TS the corresponding bite angle values are somewhat smaller, 89° - 137°). This correlation between bite angle and twist angle turns out to be again a consequence of the system's attempt to avoid steric repulsion between the ligands and the substrate.

Twist angle: The twist angle is in fact determined by the balance between two counteracting mechanisms: (i) an electronic one that favors a planar four-coordinate Pd complex; and (ii) the already alluded steric mechanism. The electronic mechanism is the donor–acceptor interaction between the occupied metal–ligand "4d_π" hybrid orbital of

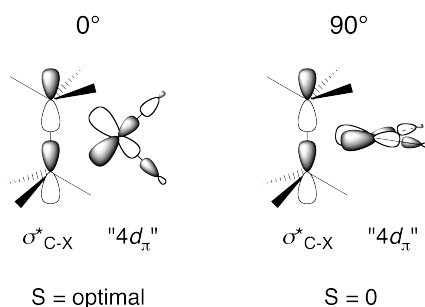


Figure 3.7 Back-donation from PdL₂ "4d_π" orbital to substrate $\sigma_{\text{C-X}}^*$ acceptor orbital (left). The $\langle "4d_{\pi}" | \sigma_{\text{C-X}}^* \rangle$ overlap is optimal for a twist angle of 0° (left) and minimal for a twist angle of 90° (right).

the catalyst complex and the unoccupied σ^*_{C-X} orbital of the substrate. This orbital interaction is most stabilizing for a planar TS geometry because the $\langle "4d\pi" | \sigma^*_{C-X} \rangle$ overlap is optimal at a twist angle of 0° and minimal at 90° (see Figure 3.7). This is also confirmed by a quantitative energy decomposition analysis: proceeding from the various TS geometries of $\text{Pd}(\text{PH}_3)_2$ inserting into the C–H, C–C and C–Cl bonds, we have analyzed the catalyst–substrate interaction ΔE_{int} as a function of varying the twist angle between the catalyst and the substrate, under the constraint that all other geometry parameters are kept frozen to their value in the TS stationary point. The results in Figure 3.8 show that indeed the orbital interaction ΔE_{oi} is in all cases most stabilizing for a planar TS geometry (0° and 180°) and least stabilizing at a twist angle of 90° .

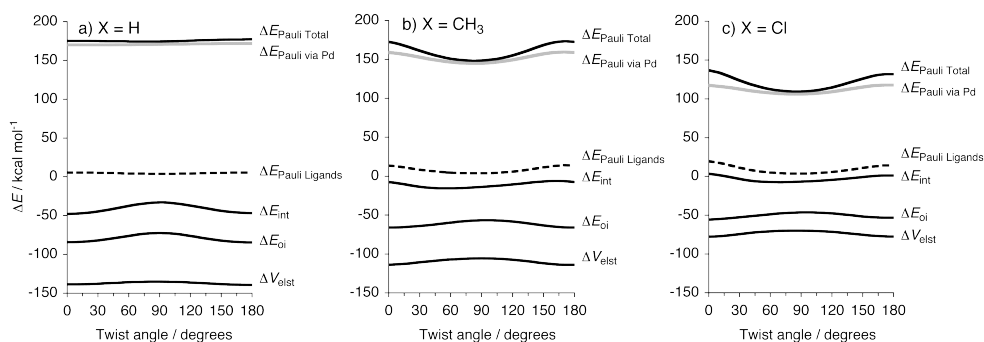


Figure 3.8 Energy decomposition analysis of the catalyst–substrate interaction ΔE_{int} as a function of the twist angle, with all other geometry parameters kept frozen to their values in the TS structures for $\text{Pd}(\text{PH}_3)_2$ insertion into three different $\text{H}_3\text{C}-\text{X}$ bonds (see text).

The electronic mechanism becomes more dominant as the reaction progresses and the C–X bond lengthens, since this decreases the energy of the substrate σ^*_{C-X} and makes it a better acceptor orbital for electrons of the catalyst "4d π " orbital. This results in a planar geometry for all the product complexes. For a given model catalyst, the twist angle in the TS decreases along the substrates CH_3Cl , CH_3CH_3 and CH_4 (e.g., from 68° to 56° to 0° in the case of $\text{Pd}(\text{PH}_3)_2$) because along this series the TS is located increasingly later along the reaction path, resembling more closely the situation in the products. This is again reflected in Figure 3.8 which shows that the "rotational barrier" in the orbital interaction, i.e., $\Delta\Delta E_{\text{oi}}(180^\circ \rightarrow 90^\circ)$, increases from 7 to 9 to 12 kcal mol⁻¹ along the OxIn reactions of C–Cl to C–C to C–H.

The steric mechanism stems from Pauli repulsion between the catalyst complex and the substrate. The larger the bite angle, i.e., along $\text{Pd}[\text{P2P}]$ to $\text{Pd}[\text{P6P}]$ to $\text{Pd}(\text{PH}_3)_2$, the more the steric mechanism opposes the electronic one leading to in-

creasingly non-planar TS geometries (see Table 3.2). In Figure 3.8, we see how the Pauli repulsion $\Delta E_{\text{Pauli Total}}$ achieves indeed a minimum at a twist angle of 90° . A separation of the Pauli repulsion into direct ligand–substrate repulsion $\Delta E_{\text{Pauli Ligands}}$ + palladium–substrate repulsion $\Delta E_{\text{Pauli via Pd}}$ (related to the destabilizing " $4d_\sigma$ " orbital) furthermore shows that both terms contribute approximately equally (see Figure 3.8). Note that for insertion into the C–H bond, the Pauli repulsion $\Delta E_{\text{Pauli Total}}$ is *high* but has a shallow minimum as function of the twist angle. The ligands–substrate repulsion $\Delta E_{\text{Pauli Ligands}}$ is however *lower* for this reaction than for insertion into the C–C and C–Cl bonds. The reason for the different behavior in the OxIn reaction of C–H is the very small effective size of the H atom in this bond.

The above bite and twist angle analyses show that the effect of the bite angle has a steric nature: a smaller bite angle corresponds to less steric repulsion between the catalyst complex and substrate since the ligands have been bent away from the substrate's coordination site at the catalyst complex. This picture is further consolidated in three additional numerical experiments. First, we have repeated the above twist-angle analysis for Pd[P2P], which has a much smaller bite angle (results not shown). In that case, the steric effect is indeed smaller and, consequently, the balance shifts towards a more planar transition state geometry (see Table 3.2). Second, we have optimized the TS of Pd(PH₃)₂ inserting into the ethane C–C bond under the constraint that the P–Pd–P bite angle is frozen to a smaller (80°) or larger value (150°) than the one it really adopts in an unconstrained TS optimization (113°). In line with the steric bite-angle mechanism, the twist angle reacts by also becoming smaller (48°) and larger (82°), respectively, than in the fully optimized TS geometry (56° ; data of constraint optimizations not shown in Table 3.2).

Third, we have extended our activation strain analyses along the entire reaction coordinate for the OxIn reactions of Pd, Pd(PH₃)₂ and Pd[P2P] into the methane C–H, ethane C–C, and chloromethane C–Cl bonds (see Figure 3.9). This allows for a more easy visualization of the strain energy along the reaction coordinate. As discussed in section 2.6, the reaction coordinate is chosen as the stretch of the C–X bond relative to the substrate. The reaction profiles in Figure 3.9a again show the dramatic increase by almost 30 kcal mol⁻¹ from uncoordinated Pd (black curve) to Pd(PH₃)₂ (blue curve) and the substantial drop in energy from Pd(PH₃)₂ to the geometrically confined Pd[P2P] complex with its small bite angle (red curve). Comparison of the activation strain diagrams of Pd and Pd(PH₃)₂ + CH₄ in Figure 3.9d reveals that the main reason for the higher reaction barrier for Pd(PH₃)₂ is a substantial destabilization

of the strain curve ΔE_{strain} . A weakening in the interaction curve ΔE_{int} also contributes but is almost two times smaller. And, finally, comparison of the activation strain diagrams of $\text{Pd}(\text{PH}_3)_2$ and $\text{Pd}[\text{P}2\text{P}] + \text{CH}_4$ in Figure 3.9g shows that the accompanying drop in reaction barrier is indeed nearly exclusively caused by a corresponding reduction in the strain curve. Note that the interaction curves for $\text{Pd}(\text{PH}_3)_2$ and $\text{Pd}[\text{P}2\text{P}]$ practically coincide. The corresponding analyses for the C–C and C–Cl bond give similar results, as can be seen in corresponding graphs in Figure 3.9. However, in these cases, the interaction energy clearly changes more dramatically upon moving to $\text{Pd}(\text{PH}_3)_2$. This is a consequence of the increased difficulty the catalyst has in approaching these more sterically crowded bonds which delays the interaction (see also section 2.4).

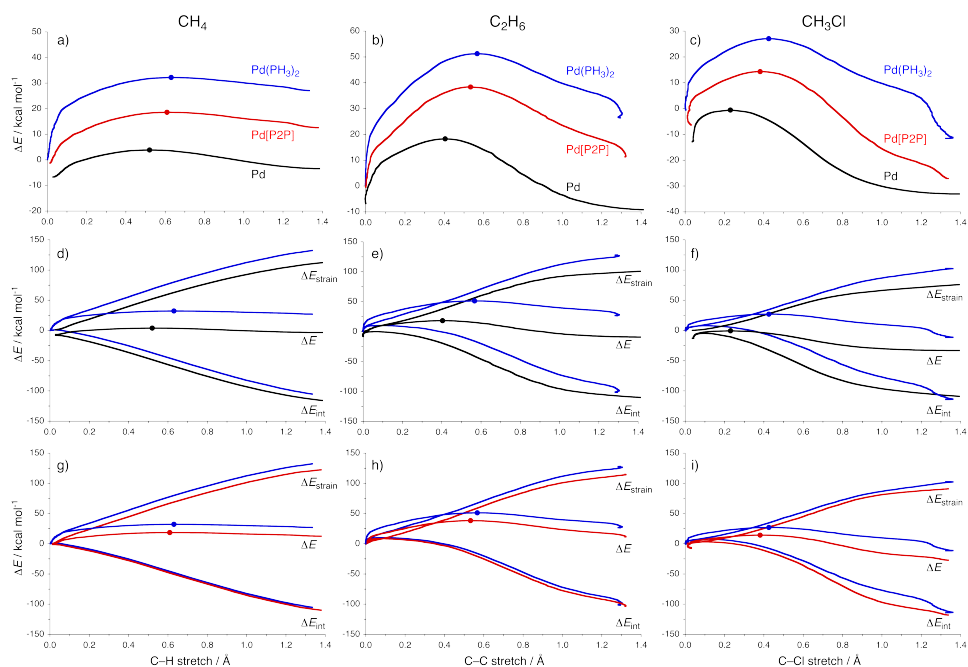


Figure 3.9 Activation strain analyses for the OxIn reactions of Pd (black), $\text{Pd}(\text{PH}_3)_2$ (blue) and $\text{Pd}[\text{P}2\text{P}]$ (red) with CH_4 (a, d, g), C_2H_6 (b, e, h) and CH_3Cl (c, f, i): Potential energy surfaces ΔE (a, b, c); Activation strain diagrams $\Delta E = \Delta E_{\text{strain}} + \Delta E_{\text{int}}$ comparing Pd and $\text{Pd}(\text{PH}_3)_2$ (d, e, f); Activation strain diagrams comparing $\text{Pd}(\text{PH}_3)_2$ and $\text{Pd}[\text{P}2\text{P}]$ (g, h, i). Dots indicate TS.

These results confirm the steric nature of bite-angle effects. Importantly, they also show that catalytic bond activation can be promoted by taking away destabilizing strain from the reaction profile. This is achieved by building it, right from the beginning, into the catalytically active transition metal complex (e.g., as in $\text{Pd}[\text{P}2\text{P}]$) instead

of letting it build up during the reaction (e.g., as in Pd(PH₃)₂). Interestingly, the increased strain in short-bridged palladium chelate complexes has also been demonstrated and applied in a related but different context, namely, catalyst selection through mass spectrometry, based on the catalyst's intrinsic stability.¹²⁷

3.4 More ligand effects

Bulky ligands: We have further explored the validity and applicability of the steric bite-angle model by examining the effect of introducing bulky substituents R = Me, Ph, *t*-Bu (instead of H) in our catalyst complexes Pd(PR₃)₂ and Pd[PR₂(CH₂)_nPR₂] with n = 2 - 4 (see Figure 3.10). The latter are designated Pd[P_nP]^R. The results of activation strain analyses for OxIn reactions with ethane are compared with those of the unsubstituted systems (R = H) in Table 3.3 and Table 3.4. Bite angles in the isolated catalyst complexes slightly but consistently widen if we go from the R = H to the bulky ligands (R = Me, Ph, *t*-Bu) but all changes remain within 5°. Importantly, the analyses in Table 3.3 and Table 3.4 confirm an important impact of steric factors. First, for a given type of catalyst complex, we find that the barrier, as well as the twist angle, increases together with the bite angle. This confirms again the increasing steric effects at larger bite angles.

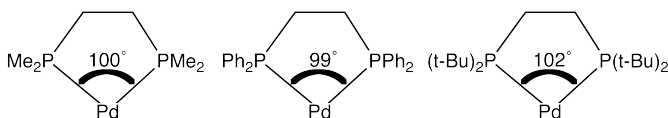


Figure 3.10 Pd[P₂P]^R (R = Me, Ph, *t*-Bu) with bite angles.

For a given bite angle (i.e., for a given length of the poly-methylene bridge), the barrier increases if the substituent becomes sterically more demanding. For example, in the OxIn reactions of Pd(PR₃)₂ + H₃C–CH₃, the barrier increases from 51 to 56 to 57 to 72 kcal mol⁻¹ along R = H, Me, Ph, *t*-Bu. The activation strain analyses in Table 3.4 show that both a weakening in the catalyst–substrate TS interaction $\Delta E_{\text{int}}^{\ddagger}$ and an increase in the catalyst activation strain $\Delta E_{\text{strain}}^{\ddagger}[\text{cat}]$ are responsible for this trend. For example, going from R = H to *t*-Bu in the OxIn reactions of Pd(PR₃)₂ + H₃C–CH₃, $\Delta E_{\text{int}}^{\ddagger}$ is weakened from -16 to -7 kcal mol⁻¹ and $\Delta E_{\text{strain}}^{\ddagger}[\text{cat}]$ is raised from 13 to 24 kcal mol⁻¹. Moreover, the effect of introducing more bulky ligands is larger if the bite angle in the catalyst complex is larger. Thus, it is sizable for Pd(PR₃)₂ (bite angle ~ 180°; the barrier increases by up to 21 kcal mol⁻¹ on substituting R = *t*-Bu for R = H), and it is relatively small for Pd[P₂P]^R (barrier increases by no more than 3 kcal mol⁻¹, on substituting R = *t*-Bu for R = H; see Table 3.4).

Besides the steric effects of the phosphine R substituents, which are particularly important for the sterically more crowded TSs of the C–C insertions, there is also an electronic effect: the bulky substituents R push the palladium *d* orbitals up in energy which causes a more stabilizing catalyst–substrate interaction and thus a lower reaction barrier ΔE^\ddagger . This effect on barrier heights can be nicely seen in Table 3.3 and Table 3.4. Note however that the strengthening in the catalyst–substrate interaction does not appear in the TS interaction $\Delta E_{\text{int}}^\ddagger$. The reason is that the more stabilizing (and steeper) catalyst–substrate interaction curve $\Delta E_{\text{int}}(\xi)$ induces a shift of the TS towards the reactant side (see also section 2.3). This indirect, structural effect is reflected nicely by the shorter C–C and C–H bonds in the TSs involving bulky phosphine substituents R. The consequence of having an earlier TS is that, despite a strengthening at a given point along ξ , the catalyst–substrate TS interaction $\Delta E_{\text{int}}^\ddagger = \Delta E_{\text{int}}^\ddagger(\xi^{\text{TS}})$ ends up being weaker because $\xi^{\text{TS}}(\text{R} = \text{Bulky}) < \xi^{\text{TS}}(\text{R} = \text{H})$.

Table 3.3 Geometry (in Å, deg) and activation strain analysis of transition states (in kcal mol⁻¹) for Pd[PnP]^R-induced H₃C–H bond activation with bulky ligands.

		bite ^a	twist ^a	C–X	$\Delta E_{\text{int}}^\ddagger$	$\Delta E_{\text{strain}}^\ddagger[\text{substr}]$	$\Delta E_{\text{strain}}^\ddagger[\text{cat}]$	ΔE^\ddagger
R = H	Pd[P2P]	85 (98)	2	1.70	-48.4	61.0	6.0	18.6
	Pd[P3P]	95 (115)	0	1.69	-46.7	59.9	9.0	22.2
	Pd[P4P]	103 (131)	2	1.70	-46.3	60.9	11.0	25.7
	Pd(PH ₃) ₂	108 (180)	0	1.73	-47.8	63.3	16.7	32.2
R = Me	Pd[P2P] ^{Me}	87 (100)	3	1.64	-44.3	55.0	6.1	16.7
	Pd[P3P] ^{Me}	98 (118)	0	1.64	-42.5	54.5	9.3	21.3
	Pd[P4P] ^{Me}	111 (136)	4	1.65	-41.7	56.0	11.9	26.3
	Pd(PMe ₃) ₂	117 (180)	1	1.66	-41.5	56.9	18.7	34.0
R = Ph	Pd[P2P] ^{Ph}	87 (99)	3	1.65	-44.1	55.6	5.5	17.0
	Pd[P3P] ^{Ph}	98 (118)	1	1.66	-43.2	56.4	8.8	21.9
	Pd[P4P] ^{Ph}	108 (136)	1	1.69	-43.9	59.3	11.9	27.3
	Pd(PPh ₃) ₂	117 (179)	2	1.74	-46.2	64.8	18.0	36.6
R = <i>t</i> -Bu	Pd[P2P] ^{<i>t</i>Bu}	89 (102)	1	1.63	-42.2	53.5	6.1	17.5
	Pd[P3P] ^{<i>t</i>Bu}	101 (120)	3	1.65	-42.1	56.0	8.9	22.8
	Pd[P4P] ^{<i>t</i>Bu}	114 (138)	7	1.71	-43.7	62.8	12.4	31.5
	Pd(P(<i>t</i> -Bu) ₃) ₂	129 (179)	7	1.85	-51.0	78.1	26.8	53.9

^a Bite and twist angle in TS and, in parentheses, in isolated PdL₂.

One can reveal the stabilizing electronic effect more directly by comparing the TS interaction $\Delta E_{\text{int}}^\ddagger$ for the bulky R with the catalyst–substrate interaction with the catalyst–substrate interaction in exactly the same, frozen TS structure (and thus at the same point along ξ) through replacing the bulky substituent R by R = H (and only optimizing the position of these R = H). Thus, for example, along the OxIn reactions

of Pd[P2P]^{Me} and Pd[P2P]^{tBu} + H₃C–H, the catalyst–substrate interaction drops from $\Delta E_{\text{int}}^{\ddagger} = -44.3$ and -42.2 kcal mol⁻¹, respectively, in the TS of the full systems (see Table 2a) down to -41.1 and -38.5 kcal mol⁻¹, respectively, in the same, frozen structures in which R has become H (not shown in the Tables). The electronic effect of the bulky R substituents is also reflected by a higher extent of charge transfer from metal *d* orbitals to substrate $\sigma_{\text{C-X}}^*$ acceptor orbitals (not shown in the Tables).

Table 3.4 Geometry (in Å, deg) and activation strain analysis of transition states (in kcal mol⁻¹) for Pd-induced H₃C–CH₃ bond activation with bulky ligands.

		bite ^a	twist ^a	C–C	$\Delta E_{\text{int}}^{\ddagger}$	$\Delta E_{\text{strain}}^{\ddagger}[\text{substr}]$	$\Delta E_{\text{strain}}^{\ddagger}[\text{cat}]$	ΔE^{\ddagger}
R = H	Pd[P2P]	87 (98)	49	2.07	-16.7	50.7	4.3	38.4
	Pd[P3P]	97 (115)	48	2.08	-15.1	51.4	6.8	43.1
	Pd[P4P]	105 (131)	49	2.09	-14.6	52.6	8.3	46.3
	Pd(PH ₃) ₂	113 (180)	56	2.11	-15.8	53.7	13.4	51.3
R = Me	Pd[P2P] ^{Me}	88 (100)	42	2.05	-14.1	48.9	4.8	39.5
	Pd[P3P] ^{Me}	100 (118)	48	2.06	-12.7	49.8	7.2	44.2
	Pd[P4P] ^{Me}	111 (136)	51	2.08	-12.0	51.5	9.6	49.1
	Pd(PMe ₃) ₂	120 (180)	56	2.09	-11.3	52.6	14.8	56.0
R = Ph	Pd[P2P] ^{Ph}	88 (99)	37	2.05	-13.6	48.9	4.6	39.9
	Pd[P3P] ^{Ph}	100 (118)	45	2.06	-13.2	50.4	7.3	44.5
	Pd[P4P] ^{Ph}	108 (136)	46	2.08	-13.7	51.6	10.1	48.0
	Pd(PPh ₃) ₂	122 (179)	62	2.13	-13.1	55.8	14.3	56.9
R = <i>t</i> -Bu	Pd[P2P] ^{tBu}	90 (102)	50	2.04	-12.2	48.1	5.3	41.2
	Pd[P3P] ^{tBu}	102 (120)	54	2.06	-10.9	50.4	7.6	47.0
	Pd[P4P] ^{tBu}	117 (138)	76	2.12	-12.0	55.8	12.1	56.0
	Pd(P(<i>t</i> -Bu) ₃) ₂	133 (179)	79	2.12	-6.9	55.0	24.0	72.1

^a Bite and twist angle in TS and, in parentheses, in isolated PdL₂.

The electronic effect of the R substituents is more pronounced for insertion into C–H bonds than into C–C bonds because the catalyst–substrate interaction is intrinsically more stabilizing in the case of the former. Thus, in the case of small bite angles, this larger back-donation substantially lowers the barriers for C–H insertion. However, if one goes towards systems with larger bite angles, the barrier-lowering electronic effect, although still present, is masked by a stronger steric destabilization resulting in the net effect that the barrier *increases*. This is particularly apparent in the CH₄ series for which all transition states involving Pd[PnP]^R are slightly (ca 2 kcal mol⁻¹) stabilized compared to those involving Pd[PnP] in the case of n = 2 whereas they become destabilized by a similar amount if we go along n = 2, 3 and 4 (see in Table 3.3).

Halophosphine ligands: We have also investigated the effect of introducing electron-*withdrawing* substituents R = F, Cl, Br and I on the phosphine groups of our

model catalysts. First, we examine the reactions of Pd[PdCl₂(CH₂)_nPdCl₂] with n = 2 - 4 (see Table 3.5). Interestingly, Pd(PCl₃)₂ behaves quite differently and is discussed hereafter. The introduction of the chlorine substituents stabilizes the phosphine lone-pair orbital, which translates into the palladium *d* orbitals being stabilized compared to the catalysts without halogen substitution.¹²¹ This has two important, mutually counteracting, effects: (i) less stabilizing back-donation from the catalyst's "4d_π" to the substrate's σ*_{C-X} orbital; and (ii) less Pauli repulsion between the catalyst's "4d_σ" orbital and closed shells on the substrate, e.g., the σ_{C-X} bond orbital.

Table 3.5 Geometry (in Å, deg) and activation strain analysis of transition states (in kcal mol⁻¹) for Pd-induced C–X bond activation with chlorine substituents.

		bite ^a	twist ^a	C–H	ΔE [‡] _{int}	ΔE [‡] _{strain} [substr]	ΔE [‡] _{strain} [cat]	ΔE [‡]
H ₃ C–H	Pd[P2P] ^{Cl}	85 (96)	1	1.82	-52.9	71.6	6.2	24.8
	Pd[P3P] ^{Cl}	93 (111)	12	1.82	-53.1	71.2	9.0	27.1
	Pd[P4P] ^{Cl}	101 (125)	11	1.80	-52.4	70.4	12.8	30.8
	Pd(PCl ₃) ₂	107 (149)	0	1.86	-55.6	75.1	9.6	29.1
H ₃ C–CH ₃	Pd[P2P] ^{Cl}	87 (96)	40	2.14	-20.7	55.9	3.5	38.8
	Pd[P3P] ^{Cl}	96 (111)	43	2.13	-19.8	56.1	5.7	42.0
	Pd[P4P] ^{Cl}	106 (125)	47	2.15	-19.5	57.4	8.7	46.5
	Pd(PCl ₃) ₂	111 (149)	55	2.16	-23.0	57.6	7.4	42.0
H ₃ C–Cl	Pd[P2P] ^{Cl}	88 (96)	36	2.27	-12.8	25.1	3.2	15.5
	Pd[P3P] ^{Cl}	98 (111)	38	2.28	-11.7	25.8	4.6	18.7
	Pd[P4P] ^{Cl}	111 (125)	54	2.30	-11.1	27.9	7.7	24.4
	Pd(PCl ₃) ₂	111 (149)	51	2.29	-13.8	27.6	6.9	20.6

^a Bite and twist angle in TS and, in parentheses, in isolated PdL₂.

The electronic effect of a reduced back-donation dominates and shows up again pronouncedly in the case of C–H bond activation because, as mentioned in the previous section, this process is characterized by a strongly stabilizing catalyst–substrate interaction. This causes a 3 - 6 kcal mol⁻¹ higher reaction barrier and a shift of the TS towards the reactant side (compare Table 3.5 and Table 3.1 for H₃C–H + Pd[P_nP] with n = 2 - 4). The latter, i.e., the structural effect, is hiding again that, at a fixed point ζ along the reaction coordinate, the interaction ΔE_{int}(ζ) is weakened because it brings the system to a later stage of the insertion process at which all interactions become stronger.

The same electronic effect also occurs in the case of C–C and C–Cl activation but is cancelled here, because the counteracting effect of a reduced Pauli repulsion between the catalyst's "4d_σ" orbital and closed shells on the substrate is more important

in these reactions than in C–H activation. Thus, C–C and C–Cl activation barriers are hardly affected by introducing chlorine substituents on the phosphine ligands.

As alluded to above, the effect of introducing R = Cl on phosphine ligands in Pd(PCl₃)₂ is quite different. This time, the effect is a pronounced *reduction* of the barrier by 7 - 9 kcal mol⁻¹ (see Table 3.5). The reason turns out to be an increased flexibility of Pd(PCl₃)₂ towards bending as a result of the fact that, upon bending the complex, the palladium "4d_π" is pushed up less by the lower-energy PCl₃ lone pairs (*vide supra*).¹²¹ In fact, we find that the isolated complex is no longer linear but has a bite angle of 149° (the linear structure is only 1 kcal mol⁻¹ higher in energy). Consequently, the activation strain stemming from the catalyst complex drops substantially (e.g., from 13.4 to 7.4 kcal mol⁻¹ in the case of C–C activation) which leads to lower barriers (compare Table 3.5 and Table 3.1). This mechanism of lowering OxIn barriers, by taking away the catalyst bending strain, is reminiscent of what we proposed earlier in this chapter; in that case, catalyst strain was taken out of the reaction profile by building it from the beginning into the catalyst complex. In the present case, the bending strain is reduced by making the catalyst complex more flexible.

Table 3.6 Geometry (in Å, deg) and activation strain analysis of transition states (in kcal mol⁻¹) for Pd-induced C–X bond activation with chlorine substituents.

		bite ^a	twist ^a	C–X	$\Delta E_{\text{int}}^{\ddagger}$	$\Delta E_{\text{strain}}^{\ddagger}[\text{substr}]$	$\Delta E_{\text{strain}}^{\ddagger}[\text{cat}]$	ΔE^{\ddagger}
H ₃ C–H	Pd[P2P]	85 (98)	2	1.70	-48.4	61.0	6.0	18.6
	Pd[P2P] ^F	85 (97)	1	1.78	-52.3	68.1	7.0	22.7
	Pd[P2P] ^{Cl}	85 (96)	1	1.82	-52.9	71.6	6.2	24.8
	Pd[P2P] ^{Br}	84 (95)	1	1.85	-53.3	73.7	6.0	26.4
	Pd[P2P] ^I	84 (95)	2	1.87	-53.6	75.4	5.9	27.7
H ₃ C–CH ₃	Pd[P2P]	87 (98)	49	2.07	-16.7	50.7	4.3	38.4
	Pd[P2P] ^F	87 (97)	43	2.13	-19.6	55.4	4.1	39.9
	Pd[P2P] ^{Cl}	87 (96)	40	2.14	-20.7	55.9	3.5	38.8
	Pd[P2P] ^{Br}	86 (95)	36	2.14	-21.2	56.5	3.5	38.8
	Pd[P2P] ^I	86 (95)	33	2.15	-21.7	56.9	3.5	38.7
H ₃ C–Cl	Pd[P2P]	89 (98)	43	2.21	-9.1	20.3	3.1	14.3
	Pd[P2P] ^F	88 (97)	39	2.27	-12.2	24.9	3.8	16.5
	Pd[P2P] ^{Cl}	88 (96)	36	2.27	-12.8	25.1	3.2	15.5
	Pd[P2P] ^{Br}	87 (95)	27	2.28	-13.1	25.3	3.1	15.3
	Pd[P2P] ^I	87 (95)	23	2.28	-13.8	25.5	2.9	14.6

^a Bite and twist angle in TS and, in parentheses, in isolated PdL₂.

Table 3.6 shows the results when employing catalyst complexes Pd[P2P]^R with R = F, Cl, Br, and I, the result of which is an increased stabilization of the *d* orbitals, decreasing the back-donation. We attribute this stabilization to a decreased anti-bonding

overlap with the lone pairs on the phosphine, which have increasingly smaller sp^3 -type lone-pair amplitude on the phosphine and more on the increasingly larger halogen substituents. Again, the steric hindrance is also decreased, mainly via the stabilization of the repulsive " $4d_\sigma$ " orbital, which negates of less efficient back-donation mostly for C–C and C–Cl. For C–H the interaction component is dominant, and the barrier is increasingly destabilized by 4 kcal mol⁻¹ for Pd[P2P]^F up to 9 kcal mol⁻¹ for Pd[P2P]^I. On the other hand, the C–C and C–Cl insertion barriers hardly change when adding the halogen substituents. Again the TSs shift to the reactant side due to stronger orbital interactions. These results again clearly show how the two different aspects compete to determine the eventual change in barrier height.

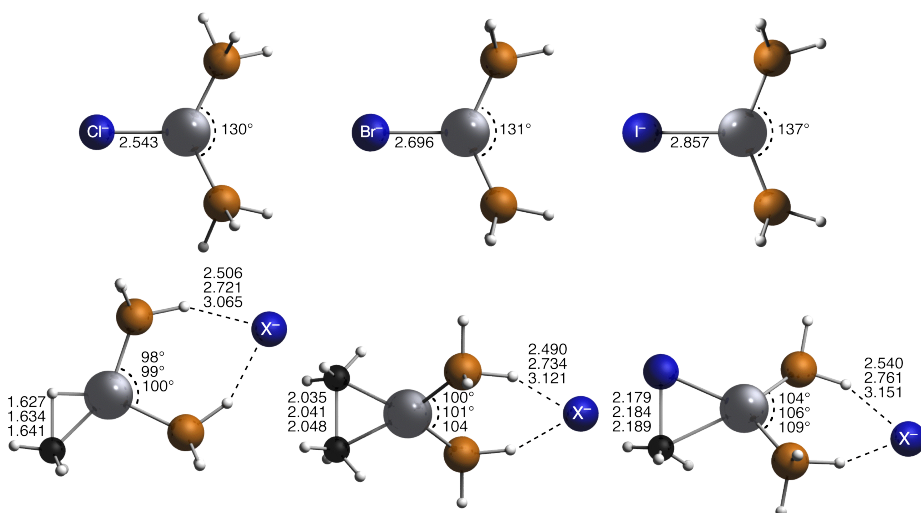


Figure 3.11 Pd(PH₃)₂X⁻ catalyst complexes and their TS for insertion into C–H, C–C and C–Cl bonds. Stacks of values for geometry parameters (in Å, deg.) refer to X⁻ = Cl⁻, Br⁻ and I⁻.

Anion assistance: The introduction of an additional halide X⁻ on PdL₂ can promote oxidative addition of a C–X bond to the resulting catalyst complex PdL₂X⁻. An interesting perspective, in the present context of a steric bite-angle mechanism, is to conceive the mechanism of this anion assistance as stemming from the fact that in the TS, the halide no longer coordinates to palladium but connects the two phosphine moieties through a P–H•••Cl•••H–P bridge (see the TS geometries in Figure 3.11).¹²⁸⁻¹³⁰ Kozuch et al.³⁸ proposed that this structural arrangement turns the [L₂X⁻] ligand system effectively into one chelating ligand with a smaller bite angle and that this lowers the barrier through the electronic mechanism of a more stabilizing catalyst-substrate back-donation (see introduction). We have analyzed this issue for oxidative addition to the model catalysts Pd(PH₃)₂X⁻ with X⁻ = F⁻, Cl⁻, Br⁻ and I⁻. In the course of the

reaction, fluoride abstracts a proton from a phosphine group, which makes it difficult to compare this reaction with the others. Therefore, X⁻ = F⁻ is left out in the following analyses.

Table 3.7 Geometry (in Å, deg) and activation strain analysis of transition states (in kcal mol⁻¹) for Pd-induced C–X bond activation, including anion halide effects.

		bite ^a	twist ^a	C–X	$\Delta E_{\text{int}}^{\ddagger}$	$\Delta E_{\text{strain}}^{\ddagger}[\text{substr}]$	$\Delta E_{\text{strain}}^{\ddagger}[\text{cat}]$	ΔE^{\ddagger}
H ₃ C–H	Pd(PH ₃) ₂	108	0	1.73	-47.8	63.3	16.7	32.2
	Pd(PH ₃) ₂ Cl ⁻	98	0	1.63	-41.3	52.8	22.2	33.7
	Pd(PH ₃) ₂ Br ⁻	99	0	1.63	-41.6	53.5	21.6	33.5
	Pd(PH ₃) ₂ I ⁻	100	0	1.64	-42.1	54.4	22.1	34.4
	Pd[P2P]	85	2	1.70	-48.4	61.0	6.0	18.6
	Pd[P2P]Cl ⁻	85	4	1.63	-43.4	52.9	21.3	30.9
H ₃ C–CH ₃	Pd(PH ₃) ₂	113	56	2.11	-15.8	53.7	13.4	51.3
	Pd(PH ₃) ₂ Cl ⁻	100	50	2.04	-10.6	47.1	20.1	56.5
	Pd(PH ₃) ₂ Br ⁻	101	50	2.04	-10.9	47.6	19.4	56.1
	Pd(PH ₃) ₂ I ⁻	104	52	2.05	-11.4	48.3	19.7	56.6
	Pd[P2P]	89	49	2.07	-16.7	50.7	4.3	38.4
	Pd[P2P]Cl ⁻	86	49	2.03	-12.5	46.1	19.9	53.5
H ₃ C–Cl	Pd(PH ₃) ₂	123	68	2.25	-7.6	25.6	9.1	27.0
	Pd(PH ₃) ₂ Cl ⁻	104	46	2.18	-5.2	17.8	17.1	29.7
	Pd(PH ₃) ₂ Br ⁻	106	48	2.18	-5.2	18.4	16.4	29.5
	Pd(PH ₃) ₂ I ⁻	109	51	2.19	-5.3	19.1	16.4	30.2
	Pd[P2P]	89	43	2.21	-9.1	20.3	3.1	14.3
	Pd[P2P]Cl ⁻	89	26	2.18	-8.8	16.6	18.6	26.4

^a Bite and twist angle in TS and, in parentheses, in isolated PdL₂.

Inspection of the results in Table 3.7 leads to two observations: (i) an additional halide ion raises the barrier for bond activation instead of reducing it; and (ii) the reason for this is that the catalyst strain $\Delta E_{\text{strain}}^{\ddagger}[\text{cat}]$ *increases* instead of dropping as one would expect for a rigid, chelate-like bidentate ligand with a short bridge between the phosphine moieties. This effect is quite similar for all halides, Cl⁻, Br⁻ and I⁻. What happens is that the negative charge of the additional halide destabilizes the metal *d* orbitals which leads to a more stabilizing back-donation into the $\sigma_{\text{C-X}}^*$ orbital of the substrate, in line with earlier work.^{23,24} This effect is hidden again because, as before, the steeper interaction curve $\Delta E_{\text{int}}^{\ddagger}(\xi)$ shifts the TS towards the reactant side at which all interactions are weaker. Note however that this indirect geometry effect shows up clearly in the up to 0.1 Å shorter C–X bond distances in the transition states in the case of anion assistance (see Table 3.7).

Most importantly, however, the stabilizing electronic effect is dominated by a substantial destabilization of the catalyst activation strain. Apparently, the $[L_2X^-]$ system is not behaving the same way as a regular bidentate ligand such as $[PnP]$, even though the phosphine units in $[L_2X^-]$ are indeed connected by a $P-H\cdots Cl\cdots H-P$ bridge (see Figure 3.11). The explanation is simple: the catalyst activation strain $\Delta E_{\text{strain}}^\ddagger[\text{cat}]$ is increased from $\text{Pd}(\text{PH}_3)_2$ to $\text{Pd}(\text{PH}_3)_2\text{X}^-$ because, in the course of the OxIn reaction, the halide–metal coordination bond in $\text{Pd}(\text{PH}_3)_2\text{X}^-$ has to dissociate to make room for the substrate that is oxidatively added to the metal center. The dissociation of the palladium–halide coordination bond is associated with an energy penalty that shows up as the increased activation strain. We find the same behavior if a halide ion is introduced as a third ligand on the chelate complex $\text{Pd}[P2P]$ (see Figure 3.12). Thus, the barriers for C–X bond activation increase from $\text{Pd}[P2P]$ to $\text{Pd}[P2P]\text{X}^-$ because the catalyst activation strain $\Delta E_{\text{strain}}^\ddagger[\text{cat}]$ increases due to the need to dissociate the palladium–halogen coordination bond as the substrate is oxidatively added. This happens despite a substantial strengthening of the catalyst–substrate back-donation caused by the charge effect of the halide ion. The balance can, however, shift to a situation in which the charge effect dominates and lowers the barriers. This happens, for example, in the case of the oxidative insertion into the chlorobenzene C–Cl bond, which, as described by Kozuch et al.,³⁸ proceeds more facile when adding chloride. It is clear from our analysis, however, that this is not due to a chelating ligand effect, neither through the classical electronic bite-angle effect nor through the steric bite-angle effect. Instead, anion assistance of this aryl C–Cl bond activation is brought about by the charge effect, i.e., the negative electrostatic potential of the halide anion.

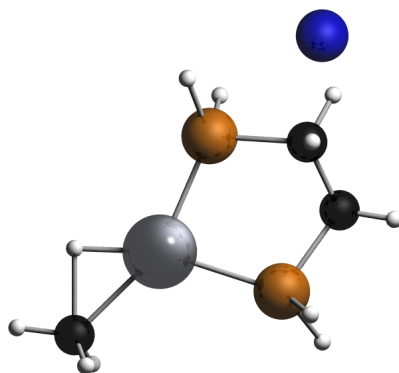


Figure 3.12 TS for OxIn of $\text{Pd}[P2P]\text{Cl}^-$ into the C–H bond.

N-heterocyclic carbene ligands: Finally, to illustrate a more general applicability, we have transferred our approach from diphosphorus to dicarbon ligands, that is, N-heterocyclic carbene (NHC) ligands which currently receive much attention in transition metal catalysis.¹³¹⁻¹³⁶ Our model catalysts comprise palladium–NHC chelate complexes $\text{Pd}[\text{CnC}]$, with $n = 2 - 5$, as well as monodentate $\text{Pd}(\text{NHC})_2$ complexes (see

Figure 3.13). Note that $n = x + 2$ equals again the number of atoms in the bridge connecting, in this case, two coordinating C atoms.

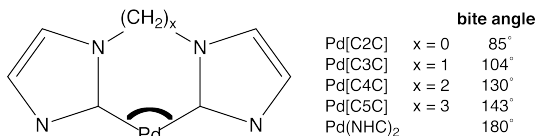


Figure 3.13 Pd[CnC] catalysts with bite angles.

The activation strain analysis of the OxIn reactions of Pd[CnC] and Pd(NHC)₂ with methane C–H and ethane C–C bonds once more confirm the steric nature of the bite-angle effects (see Table 3.8 and Figure 3.14). Thus, along the series Pd(NHC)₂ to Pd[C5C] to Pd[C2C], again the bite angle becomes smaller (from 180° to 85°) and the barrier lower (from 40 to 8 kcal mol⁻¹ for insertion into C–H), mainly, because the catalyst activation strain $\Delta E_{\text{strain}}^\ddagger[\text{cat}]$ is lowered (from 30.3 to 5.7 kcal mol⁻¹ for insertion into C–H). This is the same trend and the same steric mechanism, even more pronounced so, as found in the analyses of the corresponding Pd(PH₃)₂ and Pd[PnP] complexes (compare Table 3.2 and Table 3.8).

Table 3.8 Geometry (in Å, deg) and activation strain analysis of transition states (in kcal mol⁻¹) for Pd-induced C–X bond activation, using chelating NHC ligands.

		bite ^a	twist ^a	C–H	$\Delta E_{\text{int}}^\ddagger$	$\Delta E_{\text{strain}}^\ddagger[\text{substr}]$	$\Delta E_{\text{strain}}^\ddagger[\text{cat}]$	ΔE^\ddagger
H ₃ C–H	Pd[C2C]	77 (85)	13	1.53	-40.1	42.2	5.7	7.9
	Pd[C3C]	88 (104)	6	1.52	-37.0	41.5	8.8	13.2
	Pd[C4C]	102 (130)	3	1.49	-32.6	37.6	15.6	20.6
	Pd[C5C]	93 (143)	2	1.54	-36.9	44.0	18.8	25.9
	Pd(NHC) ₂	112 (180)	0	1.55	-34.2	44.3	30.3	40.4
H ₃ C–CH ₃	Pd[C2C]	78 (85)	18	1.98	-12.4	41.7	3.4	32.8
	Pd[C3C]	89 (104)	44	1.98	-9.1	42.1	6.4	39.3
	Pd[C4C]	106 (130)	31	1.98	-4.8	41.6	11.3	48.0
	Pd[C5C]	96 (143)	43	2.00	-7.8	44.8	14.8	51.8
	Pd(NHC) ₂	125 (180)	48	2.06	-4.0	49.7	19.2	64.8

^a Bite and twist angles in TS and, in parentheses, in isolated PdL₂.

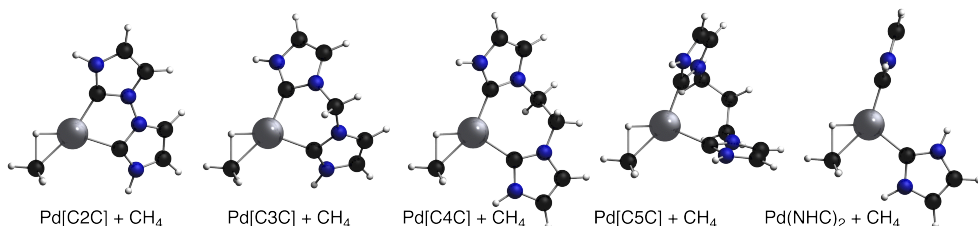


Figure 3.14 TS geometries for insertion of Pd[CnC] and Pd(NHC)₂ into the methane C–H bond (similar TS geometries for other bonds).

The overall barriers ΔE^\ddagger are somewhat higher in the case of the dicarbene complexes. An in-depth analysis reveals an interplay of factors responsible for this difference. The

dominant effect is that the dicarbene complexes Pd[CnC] are sterically more demanding than the simple Pd[PnP] complexes. In addition, they are also somewhat less flexible. This translates into more catalyst activation strain $\Delta E_{\text{strain}}^{\ddagger}[\text{cat}]$ and thus a higher barrier (compare Table 3.2 and Table 3.8).

Interestingly, the electronic mechanism does show up here and it counteracts the steric mechanism. Thus, the catalyst–substrate interaction is more stabilizing in the case of the NHC ligands because the latter push up the back-donating " $4d_{\pi}$ " orbital more than the phosphine ligands do. This effect does however not overrule the steric effect (i.e., the barrier is raised, not lowered). The strengthening of the back donation does not show up in the form of a more stabilizing catalyst–substrate TS interaction $\Delta E_{\text{int}}^{\ddagger}$ in Table 3.8. The reason is that the steeper slope of ΔE_{int} along the reaction coordinate shifts all transition states towards the reactant side at which all energy terms are smaller. This geometrical consequence, finally, is clearly visible: the C–X bonds in the transition states of the dicarbene complexes have been expanded much less (e.g., C–H = 1.53 Å in TS of Pd[C2C] + H₃C–H, see Table 3) than in the corresponding transition states of the diphosphine complexes (e.g., C–H = 1.70 Å in TS of Pd[P2P] + H₃C–H, see Table 3.2).

3.5 Conclusions

We show, based on activation strain analyses, that the well-known dependence of a catalyst's activity in C–H, C–C and C–Cl bond activation on the ligand-metal-ligand bite angle has a primarily steric origin: by bending the catalyst a priori, e.g., in chelate complexes, one avoids unfavorable non-bonded interactions with the substrate which cause the catalyst to deform and build up strain. In a sense, our steric model comes down to "taking away" destabilizing strain (i.e., catalyst deformation due to steric repulsion with substrate) from the reaction profile by building it, right from the beginning, into the catalytically active transition metal complex. We find this steric mechanism to be active in all model catalysts in this study. They cover a broad spectrum of monodentate and chelate complexes of palladium with simple, bulky and halogen-substituted diphosphine as well as N-heterocyclic carbene ligands. Anion assistance by halide ions is shown to lower barriers because of a more stabilizing catalyst–substrate back donation, not because of the fact that the halide ion adopts a bridging position between two phosphine ligands in the catalyst complex.

The fact that steric factors play a key role in the effect of the bite-angle on the barrier height does not imply the absence of π back-donation from the metal " d_{π} " to the

substrate σ^*_{C-X} acceptor orbital, as has also been pointed out, recently, by Kamer and coworkers.¹³⁷ In our present collection of model reactions, this electronic mechanism reveals itself, among others, through a shift in TS geometries if one goes from the diphosphorus to the dicarbene catalyst complexes.

Our results show how bending a PdL_2 catalyst towards smaller bite angle increases its activity through a steric mechanism. But they also show how electronic effects can modulate the activity in a selective manner. A characteristic of C–H activation is that it goes with relatively strong catalyst–substrate interaction and the introduction of electron-pushing substituents R on the phosphine ligands in the catalyst complex will translate in even more stabilizing catalyst–substrate interaction and thus lower barriers. On the other hand, C–C activation is characterized by a sterically more crowded TS and here the steric bulk of substituents R will be often the dominant factor, leading to more steric repulsion and thus higher barriers. But the relative importance of such electronic and steric factors also depends on other parameters, such as, indeed, the bite angle: small bite angles make electronic effects relatively more important whereas larger bite angles lead to a more dominant role of the steric effects of substituents.

6 Analysis of H-AH_n and CH₃-AH_n bonds

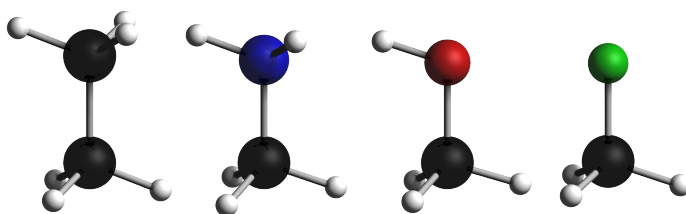
Inspired by:

Willem-Jan van Zeist, F. Matthias Bickelhaupt

Phys. Chem. Chem. Phys. **2009**, *11*, 10317

Abstract

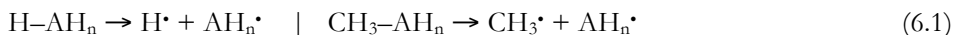
Along the series of H-AH_n bonds, with AH_n = CH₃, NH₂, OH, and F, the bond dissociation energies show a steady increase as can be expected from the increasing difference in electronegativity along this series. However, in the same series for CH₃-AH_n the bond strength first decreases from CH₃-CH₃ to CH₃-NH₂ and only thereafter increases again along CH₃-NH₂, CH₃-OH and CH₃-F. To understand the origin of the apparent anomaly occurring for the trend in C-A bond strengths, we have analyzed the bonding mechanism in H-AH_n, CH₃-AH_n and other model systems. We recover that increasing electronegativity difference across a bond causes an increasing stability. But we also find that the nature of the bond changes qualitatively for AH_n = CH₃ due to the saturation of A with hydrogens. The need of the methyl group to adopt an umbrella shaped geometry plays a key role in the difference between bonds with CH₃ and other second period AH_n radicals.



6.1 Introduction

The breaking and making of bonds are obviously important concepts in chemistry. It is therefore logical that a great deal of effort has been spent on a better understanding of the chemical bond. Still, there is debate as to why certain bonds have certain strengths.¹³⁹⁻¹⁴² An important quantity in this context is the bond dissociation energy (BDE, see equation 6.1), which identifies the strength of the chemical bond.¹³⁸ The BDE concept is of importance, not only for the stability of a specific bond, but also for its reactivity, when it is broken or formed in a chemical reaction. In order to understand trends in reactivity along different bonds, it is important to not only look at the absolute bond strengths, but also at how the bond strength changes along the series of bonds, as the relative order of strengths will play a role in the selectivity of chemical reactions. Obviously a lot of effort has been spent to correctly describe and understand BDE values.¹⁴³⁻¹⁵¹

In the series of second period bonds in H-AH_n and $\text{CH}_3\text{-AH}_n$ ($\text{AH}_n = \text{CH}_3, \text{NH}_2, \text{OH},$ and F), we came across an interesting trend in bond strengths. There is an increase in the H-A bond strength along $\text{AH}_n = \text{CH}_3, \text{NH}_2, \text{OH},$ and F . However, when turning to the $\text{CH}_3\text{-AH}_n$ bond, there is first a *decrease* from $\text{CH}_3\text{-CH}_3$ to $\text{CH}_3\text{-NH}_2$ after which the bond strength increases again. Interestingly, in both cases the bond distances do systematically decrease in going down the second period. See Table 6.1 for experimental¹³⁸ and calculated values.



In the case of H-AH_n , the steady *increase* in bond strength along $\text{AH}_n = \text{CH}_3, \text{NH}_2, \text{OH},$ and F , is as might be expected from the increasing electronegativity along $\text{C}, \text{N}, \text{O},$ and F which in Pauling units adopts the values, 2.55, 3.05, 3.44, and 3.98, respectively.^{152,153} This trend, which leads to an *increasing difference* in electronegativity across H-AH_n or $\text{CH}_3\text{-AH}_n$ bonds, derives from the $n\bar{p}$ (or $n\bar{p}$ -derived) singly-occupied molecular orbital (SOMO) of the effective electronegative $\text{AH}_n\cdot$ fragment. This SOMO constitutes the main component of the H-AH_n or $\text{CH}_3\text{-AH}_n$ electron-pair bonding molecular orbital (MO) of the overall molecule and a decrease of its energy (i.e., an increase in the electronegativity of A) translates, in general, directly into a stronger bond.^{154,155} This is what happens, e.g., for the present H-AH_n bonds or the carbon-halogen bonds in CH_3X as X varies along $\text{At}, \text{I}, \text{Br}, \text{Cl},$ and F .^{68,156}

Simply thinking, one would expect this trend also to occur for the series of $\text{CH}_3\text{-AH}_n$ bonds. However, we find a discrepancy in the case of $\text{AH}_n = \text{CH}_3$ where, apparently, the completely apolar C–C bond is not, as expected, weaker but instead stronger than the polar C–N bond. In fact, if we look closer, there appear to be signs of a similar anomaly also for the H-AH_n series. Here, the BDE still becomes stronger

from H-CH_3 to H-NH_2 . Note however that this step is associated with the smallest change in BDE along the series, merely $2.6 \text{ kcal mol}^{-1}$ (see Table 6.1), whereas the change in electronegativity from $\text{AH}_n = \text{CH}_3$ to NH_2 is the largest.

To fully understand these trends in bond strengths and, in particular, the anomaly from $\text{CH}_3\text{-CH}_3$ to $\text{CH}_3\text{-NH}_2$, we have carefully analyzed the H–A and C–A bonding mechanism in our H-AH_n and $\text{CH}_3\text{-AH}_n$ model systems. In addition, we have analyzed the H–A and C–A bonds in the unsubstituted $\text{H-A}^m\cdot$ and $\text{CH}_3\text{-A}^m\cdot$ radicals. This enables us to isolate the intrinsic influence of the electronegativity of the atom $\text{A} = \text{C, N, O}$ and F , i.e., in the absence of steric or other effects stemming from the hydrogen atoms at AH_n . Indeed, as we will show, the aforementioned anomaly is caused by the saturation of coordination space around A in the case of carbon. Thus, the $\text{AH}_n\cdot = \text{CH}_3\cdot$ fragment appears to interact with the other radical fragment ($\text{H}\cdot$ or $\text{CH}_3\cdot$) qualitatively different if compared to the other $\text{AH}_n\cdot = \text{NH}_2\cdot, \text{OH}\cdot,$ and $\text{F}\cdot$.

6.2 Results and discussion

Table 6.1 shows the experimental as well as our calculated values of the H-AH_n and $\text{CH}_3\text{-AH}_n$ bond dissociation enthalpies. Our BLYP/TZ2P approach somewhat underestimates the bond strengths by a few kcal mol^{-1} . Note however that it nicely reproduces the trends in bond strengths, which is our prime interest. Table 6.2 shows the decomposition of the bond dissociation energy BDE (ΔE) into strain (ΔE_{strain}) and interaction (ΔE_{int}) for all the H-AH_n and $\text{CH}_3\text{-AH}_n$ bonds. Note that ΔE is the change in total *energy* and not the enthalpy, as used in Table 6.1.

Table 6.1 H-AH_n and $\text{CH}_3\text{-AH}_n$ bond distances and bond dissociation enthalpies at 298 K.

	Calculated ^b		Experimental
	H–A, C–A	ΔH_{298}	ΔH_{298}^c
H–CH ₃	1.095	102.2	105.0
H–NH ₂	1.022	104.2	107.6
H–OH	0.972	115.9	118.8
H–F	0.936	135.6	136.3
CH ₃ –CH ₃	1.540	83.2	90.1
CH ₃ –NH ₂	1.480	78.4	85.2
CH ₃ –OH	1.443	87.9	92.1
CH ₃ –F	1.413	110.4	115

^a In Å and kcal mol^{-1} . ^b This work: calculated at BLYP/TZ2P.

^c Experimental values taken from Blanksby and Ellison.¹³⁸

From Table 6.2, it is easily seen that the largest contribution to the BDE is the interaction energy ΔE_{int} . What also becomes clear, now, is that the interaction energy shows the anomaly of a weakening not only from $\text{CH}_3\text{-CH}_3$ to $\text{CH}_3\text{-NH}_2$, as observed also for the BDE, but also from H-CH_3 to H-NH_2 . Also the strain energy shows an anomaly in the case

Table 6.2 H-AH_n and CH₃-AH_n bond distances and activation strain analysis.^a

	H-A, C-A	ΔE	ΔE_{strain}	ΔE_{int}
H-CH ₃	1.095	-109.7	7.2	-116.9
H-[CH ₃] ^b	1.141	-89.3	0.1	-89.3
H-NH ₂	1.022	-112.1	0.3	-112.4
H-OH	0.972	-122.5	0.1	-122.6
H-F	0.936	-140.3	0.0	-140.3
CH ₃ -CH ₃	1.540	-89.9	18.4	-108.4
CH ₃ -[CH ₃] ^b	1.677	-63.0	8.5	-71.4
CH ₃ -NH ₂	1.480	-85.4	9.4	-94.8
CH ₃ -OH	1.443	-93.8	8.1	-101.9
CH ₃ -F	1.413	-114.4	6.3	-120.7

^a In Å and kcal mol⁻¹, calculated at BLYP/TZ2P. ^b Optimized while keeping one methyl group fixed in a planar geometry (see text).

of AH_n = CH₃. In all bonds involving AH_n = NH₂, OH, and F, the strain energy is constantly low, practically zero for H-AH_n and 6 - 9 kcal mol⁻¹ for CH₃-AH_n. As soon as AH_n = CH₃, the strain energy jumps up, from ~0 to 7 kcal mol⁻¹ for H-AH_n and from 9 to 18 kcal mol⁻¹ for CH₃-AH_n. This originates from the fact that the CH₃• radical fragment is the only one that is deformed substantially from its planar equilibrium geometry to the pyramidal geometry it has in the overall molecule.

To further investigate the effect that CH₃ pyramidalization has on the H-CH₃ and CH₃-CH₃ bonding mechanism, we have optimized the geometry of these species under the constraint that AH_n = CH₃ (i.e., the CH₃ group in methane and one of the two CH₃ groups in ethane) is kept planar while *all* other geometry parameters are included in the optimization. This computational experiment leads to a number of interesting phenomena: (i) the H-C and C-C bonds elongate; (ii) the strain energy drops to a value that is in the same range as found for the other H-AH_n and CH₃-AH_n systems; and (iii) now, the interaction energy *does* follow the expected trend (i.e., it increases as the electronegativity difference across the H-A or C-A bond increases) because the interaction of H or CH₃ with the *planar* AH_n = CH₃ is *less stabilizing* than with the NH₂ moiety.

Each of the three phenomena above can be easily explained and this leads us to understand the trends, and anomalies therein, in H-AH_n and CH₃-AH_n bond strengths. We begin with the latter observation, namely, that a planar AH_n moiety leads to the regular trend of a strengthening in the H-A and C-A interaction throughout the series of AH_n = CH₃, NH₂, OH and F.

To separate the electronegativity effect of the central atom A and the effect of hydrogen substitution at AH_n , we first focus solely on the former by removing all the hydrogen substituents from the AH_n moieties. This results in the series $H-A^{m\bullet} = HC^\bullet$, HN^\bullet , HO^\bullet , HF , and $CH_3-A^{m\bullet} = CH_3C^\bullet$, CH_3N^\bullet , CH_3O^\bullet , CH_3F , all in their ground state configurations. Thus, we analyze the electron-pair bonding interaction of H^\bullet (with its $1s$ SOMO) and of CH_3^\bullet (with its $2p_z$ -derived sp^3 hybrid SOMO) with the singly occupied $2p_z$ AO on $A^{(m+1)\bullet} = C^\bullet$ ($2s^2 2p_x^1 2p_y^0 2p_z^1$), N^\bullet ($2s^2 2p_x^1 2p_y^1 2p_z^1$), O^\bullet ($2s^2 2p_x^2 2p_y^1 2p_z^1$), F^\bullet ($2s^2 2p_x^2 2p_y^2 2p_z^1$). The results of these analyses are shown in Figure 6.1 and Figure 6.3.

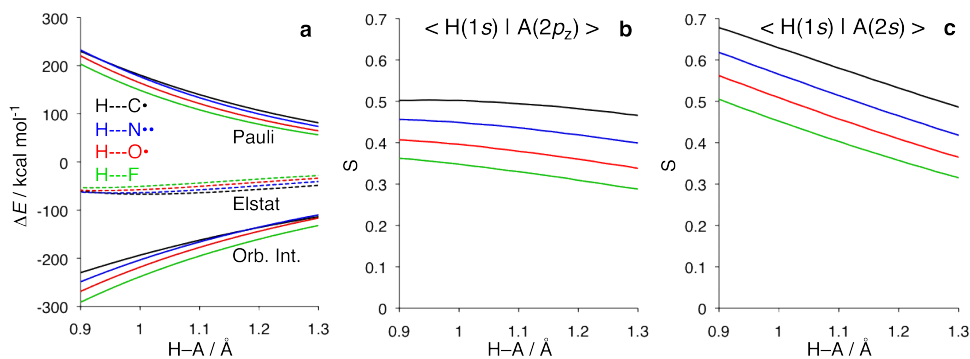


Figure 6.1 Analysis of H-A bonds in $H-A^{m\bullet}$ as a function of the bond distance. $A^{(m+1)\bullet} = C^\bullet$ (black), N^\bullet (blue), O^\bullet (red), F^\bullet (green). (a) decomposition of interaction into Pauli repulsion, electrostatic interactions, and orbital interactions. (b) Bond overlap between the $H(1s)$ and $A(2p_z)$ SOMO orbitals. (c) Repulsive overlap between $H(1s)$ and $A(2s)$ orbitals.

Figure 6.1a shows the interaction curves and decomposition analysis for the unsubstituted $H-A^{m\bullet}$ systems as a function of the H-A distance. This graph shows us a quite straightforward picture. Firstly, the orbital-interaction curves are lowered, i.e., they become more stabilizing, along $H-C^\bullet$, $H-N^\bullet$, $H-O^\bullet$, and $H-F$. This conforms to the expectations based on electronegativity differences. Indeed, upon formation of the electron pair bond, there is an increasing stabilization along C, N, O, and F because the $2p_z$ SOMO of these atoms is more and more stabilized along this series (from -5.9 to -8.1 to -10.7 to -13.4 eV, respectively). Note that this strengthening in orbital interactions is established despite the fact that the binding overlap counteracts, i.e., decreases along the series (see Figure 6.1b), due to the more and more compact nature of the $2p$ SOMO as one goes along the second period towards fluorine (see Figure 6.2).

Another, somewhat smaller, effect that also contributes to the trend of a strengthening in $H-A^{m\bullet}$ interaction along $A = C, N, O,$ and F is a decrease in Pauli repulsion.

This originates again from the decreasing size of the $2s$ orbitals (see Figure 6.2) which, in turn, yields a smaller destabilizing $\langle H(1s) | A(2s) \rangle$ overlap (see Figure 6.1c).

In the corresponding $\text{CH}_3\text{-A}^{m*}$ bonds, the latter trend of decreasing Pauli repulsion becomes the dominant effect in determining the strengthening along $A = \text{C, N, O}$ and F (compare

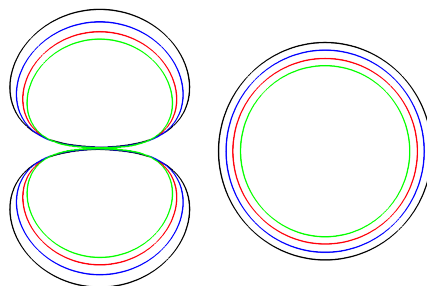


Figure 6.2 The $2p_z$ (left) and $2s$ (right) atomic orbitals of C^* (black), N^{**} (blue), O^{**} (red), F^* (green); 0.05 contour lines.

Figure 6.1a and Figure 6.3a). Here, in addition to the overlap of the carbon $2p_z$ -derived CH_3 SOMO with the closed-shell $2s$ orbital on A (see Figure 6.3c), we have also Pauli-repulsion due to overlap of the closed-shell carbon $2s$ -derived orbital on CH_3 with the $2p_z$ SOMO on A (not shown in Figure 6.3). This extra Pauli repulsion mechanism in the $\text{CH}_3\text{-A}^{m*}$ systems has also the "side-effect" of attenuating the trend of increasing orbital interactions (compare Figure 6.1a and Figure 6.3a). The reason is that the decrease in the $2p_z$ SOMO energy along $A = \text{C, N, O}$ and F is effectively counteracted as this orbital approaches from above the occupied carbon $2s$ -derived CH_3 orbital and is, therefore, more and more pushed up by the latter. Such an effect is not present in the H-A^{m*} systems.

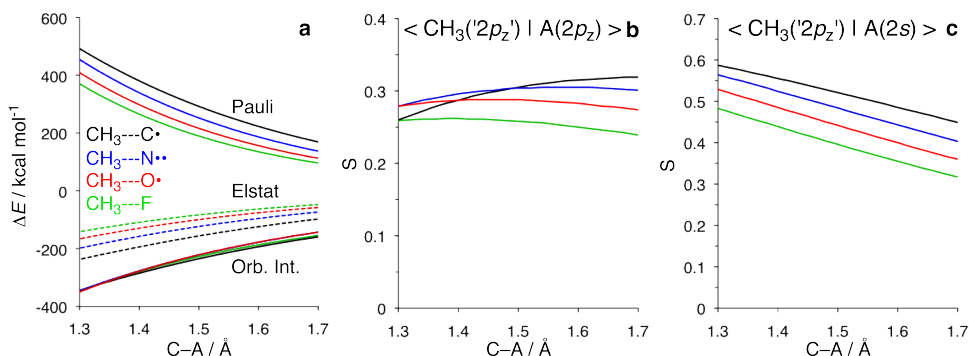


Figure 6.3 Analysis of C-A bonds in $\text{CH}_3\text{-A}^{(m+1)*}$ as a function of the bond distance. $\text{A}^{(m+1)*} = \text{C}^*$ (black), N^{**} (blue), O^{**} (red), F^* (green). (a) decomposition of into Pauli repulsion, electrostatic interactions, and orbital interactions. (b) Bond overlap between the $\text{CH}_3(2p_z)$ and $\text{A}(2p_z)$ SOMO orbitals. (c) Repulsive overlap between $\text{CH}_3(2p_z)$ and $\text{A}(2s)$ orbitals.

Next, in a second step, the hydrogen substituents are re-introduced. However, in order to separate electronic from steric and deformation effects, we have conducted the bond analysis of the H-AH_n and $\text{CH}_3\text{-AH}_n$ systems with H-A-H and C-A-H angles,

respectively, kept at 90° . These partially frozen systems are designated $\text{H}-[\text{AH}_n]$ and $\text{CH}_3-[\text{AH}_n]$. This ensures that the electron-pair bond coincides with the z -axis of the AH_n $2p_z$ SOMOs, perpendicular to the plane defined by AH_n . In the case of $\text{A} = \text{CH}_3$, this corresponds to keeping the CH_3^\bullet moiety planar, which results in the SOMO having pure $2p_z$ character also for this AH_n fragment. Figure 6.4 shows the energy decomposition analysis of these systems, again as a function of bond distance.

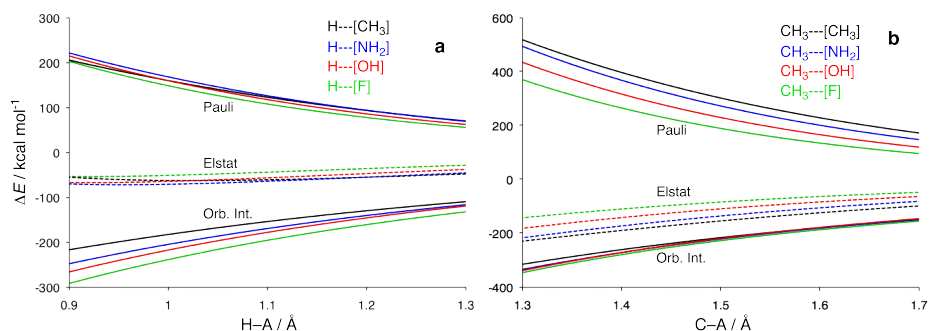


Figure 6.4 Energy decomposition analysis of (a) the $\text{H}-[\text{AH}_n]$ and (b) the $\text{CH}_3-[\text{AH}_n]$ bonds. The $\text{H}-\text{A}-\text{H}$ and $\text{CH}_3-\text{A}-\text{H}$ angles, respectively, are constrained at 90° , see also text. $\text{AH}_n = \text{CH}_3$ (black), NH_2 (blue), OH (red), F (green).

Remarkably, the trends for $\text{H}-[\text{AH}_n]$ and $\text{CH}_3-[\text{AH}_n]$ are very similar to that of the unsubstituted $\text{H}-\text{A}^{\text{m}\bullet}$ and $\text{CH}_3-\text{AH}^{\text{m}\bullet}$ systems. The reason is that $[\text{AH}_n]$ in this numerical experiment still forms electron-pair bonds with its essential carbon $2p_z$ -derived orbital and because the pyramidalization effect in the case of $[\text{CH}_3]$ has been switched off. Thus, we observe the basic principle of increasing orbital interactions due to electronegativity differences, combined with decreasing Pauli repulsive effects due to smaller destabilizing orbitals along $[\text{AH}_n] = [\text{CH}_3], [\text{NH}_2], [\text{OH}]$ and $[\text{F}]$ (see Figure 6.4). Note that the total interaction energy ΔE_{int} in these series still follows the trend originating from the differences in electronegativity (a trend similar as in Table 6.2). We can conclude that adding hydrogen substituents does not intrinsically alter the interaction compared to the atoms. It is apparently the geometrical deformation that is induced, in particular in the case of $\text{AH}_n = \text{CH}_3$, that brings about the anomaly of a decreasing $\text{H}-\text{A}$ and $\text{C}-\text{A}$ interaction energy from $\text{A} = \text{C}$ to N .

Finally, we compare the constrained $\text{H}-[\text{AH}_n]$ and $\text{CH}_3-[\text{AH}_n]$ with the $\text{H}-\text{AH}_n$ and CH_3-AH_n bonds we were originally interested in. Thus, we return to the original series of molecules in their ground state equilibrium geometry. We again perform the energy decomposition by varying the $\text{H}-\text{A}$ and $\text{C}-\text{A}$ bond distances from the $\text{H}-\text{AH}_n$ and CH_3-AH_n , this time with the CH_3 and AH_n fragments in their $\text{H}-\text{AH}_n$ or CH_3-

AH_n equilibrium structures (see Figure 6.5).^{*} The striking differences between the constrained and the optimized H-AH_n or $\text{CH}_3\text{-AH}_n$ systems occur for $\text{AH}_n = \text{CH}_3$, not so much for the other AH_n . Thus, for $\text{AH}_n = \text{CH}_3$, the Pauli repulsion drops significantly in the analyses of the fully optimized molecules. The orbital interaction behaves more or less as in the previous analyses: they become more stabilizing from $\text{AH}_n = \text{CH}_3$ to F.

It is clear that methyl pyramidalization (i.e., for $\text{AH}_n = \text{CH}_3$) has a great influence on the H-CH_3 and $\text{CH}_3\text{-CH}_3$ bonding mechanism, the main effect being a drop in steric (Pauli) repulsion upon going towards pyramidal CH_3 (compare Figure 6.4 and Figure 6.5). Although the pyramidalization of the methyl radical is associated with a cost in strain energy,¹⁵⁷ there is a net gradient towards this deformation because of the aforementioned reduction in Pauli repulsion (for a given C-C distance) and the resulting shortening of the C-C bond from 1.677 Å in $\text{CH}_3\text{-[CH}_3]$ to 1.540 Å in $\text{CH}_3\text{-CH}_3$ (see Table 6.2).

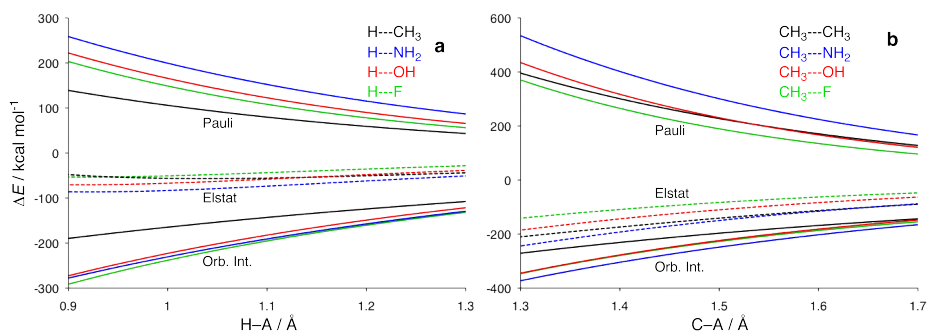


Figure 6.5 Energy decomposition analysis of the H-AH_n and $\text{CH}_3\text{-AH}_n$ bonds as a function of the bond distance. $\text{AH}_n = \text{CH}_3$ (black), NH_2 (blue), OH (red), F (green).

Thus, the methyl group gains overall H-CH_3 or $\text{CH}_3\text{-CH}_3$ bonding stabilization by reducing steric (Pauli) repulsion through bending the C-H bonds away from the other fragment. Why do similar effects not occur for the other AH_n groups, i.e., NH_2 , OH and F ? In the latter, there is also Pauli repulsion with N-H and O-H bonding orbitals that could be reduced by bending these bonds away. In fact, they do bend away, but only slightly and essentially without a net gain in stability. The reason is that in the case of NH_2 , OH and also F , there is also Pauli repulsion with the lone-pair orbitals at

^{*} The analyses for $\text{AH}_n = \text{NH}_2$ and OH are not uniquely defined. In these cases, the approach of H^\bullet (or CH_3^\bullet) is not exactly aligned with the $2p_z$ -derived SOMO of OH^\bullet and NH_2^\bullet that form the electron pair bond. This gives rise to a small increase in orbital interaction and Pauli repulsion. These changes are, however, not large, as can be seen by comparing the results in Figure 6.5 with those of the constrained analyses in Figure 6.4.

the central atom. But, at variance to the corresponding bond orbitals, these lone pairs do not involve any substituent atoms (e.g., the H atoms in AH_n) that could be bent away. Interestingly, this makes that, for example, in $H-[NH_2]$ and $CH_3-[NH_2]$, the ΔE_{Pauli} curve is actually *less destabilizing* due to a diminished overlap with the $[NH_2]$ lone-pair orbital) than the ΔE_{Pauli} curve in the real $H-NH_2$ and CH_3-NH_2 in which the N–H bonds can bend away from the approaching H and CH_3 group, respectively (compare Figure 6.4 and Figure 6.5).

6.3 Conclusions

The intrinsic $H-A^{m*}$ and CH_3-A^{m*} bond strengths increase systematically along $A = C, N, O$ and F because: (i) the increasing electronegativity difference across the bond (dominant factor for $H-A$ bond), and (ii) the decreasing Pauli repulsion with the smaller and smaller atom A (dominant factor for $C-A$ bond). Interestingly, the fact that the $H-AH_n$ and CH_3-AH_n bond energy increases only slightly from $H-CH_3$ to $H-NH_2$ and even *decreases* (i.e., shows an inverted trend) from CH_3-CH_3 to CH_3-NH_2 is due to the pyramidalization that occurs uniquely for the methyl group. This pyramidalization is associated with a deformation strain energy which is however (more than) compensated by the concomitant relieve in Pauli repulsion and the resulting bond contraction and strengthening.

In the other $H-AH_n$ and CH_3-AH_n bonds there is also Pauli repulsion with $A-H$ bond orbitals and lone pairs. But here, bending away the $A-H$ bonds (which would be the equivalent to methyl pyramidalization) does not yield a reduction in Pauli repulsion. The reason is that the lone-pair orbitals at the central atom of NH_2 , OH and also F do not involve any substituent atoms (e.g., the H atoms in AH_n) that could be bent away.

9 Summary

This thesis deals with theoretical studies on oxidative insertion reactions of catalytically active palladium compounds into archetypal bonds of model substrates. Oxidative insertion is the first and usually rate-determining bond activating step in the (Nobel Prize winning) cross-coupling reaction, which is an important tool in transition metal mediated organic synthesis. The focus is on understanding trends in activation barriers upon variation of either the catalyst or substrate structure.

The approach adopted to investigate the mechanism of these bond activations is the activation strain model, employed by means of Density Functional Theory (DFT) calculations with the ADF program. This model allows us to analyze the geometry and energy of the transition states, but also the behavior along the reaction path, from the perspective of the original reactants. As these reactants approach each other, they will start to interact and thus deform. The total energy and, in particular, the activation energy can thus be divided into contributions from the deformation of the reactants (the strain energy) and their mutual interaction (the interaction energy). The interaction energy, analyzed with the ADF energy decomposition analysis, comprises stabilizing orbital interactions, electrostatic interactions and destabilizing Pauli repulsion.

It is essential to consider both the strain and interaction energy along the entire potential energy surface because, due to their mutual interplay, changes in one or both of the terms leads in general to a shift in the location of the transition state along the reaction path. This is exactly where the activation strain model plays an important and clarifying role.

The third chapter of this thesis deals with the 'steric nature of the bite angle'. The size of the ligand-metal-ligand bite angle is often considered an important parameter for the determination of catalytic activity. A smaller bite angle usually translates to lower activation barriers, a behavior traditionally ascribed to an electronic mechanism in which the back-donation from the " $4d_{\pi}$ " orbital increases as it is pushed up in energy at smaller bite angles. In contrast with this, our analyses show how the bite angle has a primarily steric origin: by bending the catalyst a priori, e.g., in chelate complexes, one avoids unfavorable nonbonded interactions with the substrate, which cause the catalyst to deform and build up strain. In a sense, our steric model comes down to "taking away" destabilizing strain (i.e., catalyst deformation due to steric repulsion

with substrate) from the reaction profile by building it, right from the beginning, into the catalytically active transition metal complex.

Our results also show how electronic effects can modulate the activity in a selective manner. For example, the introduction of electron-pushing substituents on the phosphine ligands reinforces the back-donation, and this stabilizing effect is especially strong for C–H activation, where the intrinsic catalyst–substrate interaction is large. On the other hand, for the more sterically crowded C–C activation, the destabilizing steric bulk of substituents will be often the dominant factor. But the relative importance of such electronic and steric factors also depends on other parameters, such as, indeed, the bite angle: small bite angles make electronic effects relatively more important whereas larger bite angles lead to a more dominant role of the steric effects of substituents. This type of behavior, where the effect of ligands is influenced by the intrinsic reactivity towards different bonds, is seen throughout this thesis across a wide range of substrates and structural motifs in the catalyst.

Chapters 4 and 5 address the effect of steric bulk in the substrate on the activation of alkane C–H and C–C bonds, respectively. Although the bonds become weaker upon increased substitution by bulky methyl groups, the barriers for their activation increase. The fully substituted bonds have the highest barriers, because a methyl group hinders an effective interaction of the catalyst with the bond. The substrate has to deform before a favorable, stabilizing interaction can be established. The catalyst has increasing difficulty to approach the bond. Such a delay in the catalyst–substrate interaction results in a raise of the barrier height. Another weakening of the interaction energy is caused by less favorable back-bonding from Pd to the bond. The reason for this is that the energies of the σ^* LUMO orbitals in the more bulky substrates decrease less fast along the reaction path.

Chapters 6 and 7 deal with a series of hydrogen–element and carbon–element bonds in H–AH_n and CH₃–AH_n (AH_n = CH₃, NH₂, OH, and F), covering two series of increasingly polar bonds along the second period. Chapter 6 investigates the trends in bond strengths for these substrates and describes how the CH₃ moiety behaves differently compared to the other second period bonds, due to the bending of the methyl radical into the umbrella shape that it acquires in the overall molecule. The main difference with the other H–AH_n and CH₃–AH_n bonds is that, instead of A–H bonds, they have lone pairs on A which can not be bent away by moving back a hydrogen nucleus. The result is lower Pauli repulsive interactions, making the bonds involving

the methyl moiety stronger than would be expected on the basis of electronegativity differences.

Chapter 7 investigates the activation of these series of increasingly polar bonds. The bond strengths along the series are dominant in determining the trends in rising activation barriers for these bonds by bare palladium. The effect of the trends in bond dissociation energies is to some extent counteracted by an increase of back-donation capability into the lower-lying σ^* LUMO of the more polar bonds. Regarding the cases where $\text{AH}_n = \text{CH}_3$, we can conclude that the more sterically demanding methyl group always induces higher strain than would be expected based on the bond strength. This behavior, when moving to a fully substituted moiety induces a sharp increase in the strain energy, is similar to that of going to the fully substituted alkane bonds as seen in chapters 4 and 5.

Chapter 8 deals with a series of differently hybridized bonds, and looks at the activation of $\text{C}(\text{sp}^3)\text{-X}$, $\text{C}(\text{sp}^2)\text{-X}$, and $\text{C}(\text{sp})\text{-X}$ bonds in X-substituted ethane, ethylene, and acetylene, respectively, with $\text{X} = \text{H}$, CH_3 , and Cl . In this series, we observe a steady decrease in barrier heights for their activation by palladium, despite the fact that the bonds become stronger. There are two important reasons for this behavior: 1) in going from sp^3 to sp hybridization, back-donation is increased due to lower lying $\sigma^*_{\text{C-X}}$ LUMO orbitals on the substrate, and to a lesser extent, due to interactions with the $\pi_{\text{C-C}}$ and $\pi^*_{\text{C-C}}$ orbitals; 2) decreased steric repulsion as the activated C-X bond becomes sterically less shielded in going towards sp hybridization.

10 Samenvatting

Dit proefschrift beschrijft theoretische studies naar oxidatieve-insertiereacties van katalytisch actieve palladium-complexen in archetypische bindingen van modelsubstraten. Het oxidatieve-insertiemechanisme is de eerste en normaal gesproken snelheidsbepalende bindingsactiveringsstap in de (Nobelprijs-winnende) ‘cross-coupling’ reacties, welke een belangrijk gereedschap zijn in de organische synthese. De klemtoon ligt op het begrijpen van de trends in activeringsbarrières wanneer de structuur van de katalysator of het substraat gevarieerd wordt.

De aanpak om het mechanisme van deze bindingsactiveringen te onderzoeken is het ‘activation strain’ model, dat wordt toegepast door middel van Dichtheidsfunctio-naaltheorie (DFT) berekeningen met het ADF-programma. Dit model stelt ons in staat om de geometrie en energie van de overgangstoestanden, maar ook het gedrag langs het reactiepad, te analyseren vanuit het perspectief van de oorspronkelijke reactanten. Wanneer de reactanten elkaar naderen, beginnen ze te wisselwerken en elkaar te vervormen. De totale energie en in het bijzonder de activeringsenergie kan dus opgesplitst worden in bijdragen van de deformatie van de reactanten (de deformatie- of spanningsenergie) en hun onderlinge interactie (de interactie-energie). De interactie-energie, die geanalyseerd kan worden met behulp van een energie-decompositie analyse binnen ADF, bestaat uit stabiliserende orbitaal-interacties, electrostatische interacties en destabiliserende Pauli repulsie.

Het is van vitaal belang om zowel de spanning als interactie langs het hele reactiepad te beschouwen; door hun wederzijdse interactie leiden veranderingen in de termen gewoonlijk tot een verschuiving van de locatie van de overgangstoestand langs het reactiepad. Dit is precies het gebied waarin het ‘activation strain’ model een belangrijke en verhelderende rol speelt.

Het derde hoofdstuk behandelt de ‘sterische aard van de bite angle’. De grootte van de ligand-metaal-ligand hoek, of ‘bite angle’, wordt vaak als een belangrijke parameter gezien wat betreft de bepaling van katalytische activiteit. Een kleinere bite angle vertaalt zich normaal gesproken naar lagere activeringsbarrières, iets wat traditioneel wordt toegeschreven aan een electronisch mechanisme waarin de electrondonatie vanuit de " $4d_{\pi}$ " orbitaal verbetert, omdat deze in energie omhoog geduwd wordt bij kleinere bite angles. In tegenstelling tot dit beeld, laat onze analyse zien hoe de bite

angle een primair sterische oorsprong heeft: door het a priori buigen van de katalysator, zoals in chelerende complexen, vermijdt men ongunstige niet-bindende interacties met het substraat, die de liganden anders zouden wegbuigen waardoor meer spanning zou ontstaan. In zekere zin komt ons sterische model neer op het “wegnemen” van destabiliserende deformatie (oftewel de deformatie van de katalysator door sterische repulsie met het substraat) uit het reactieprofiel door deze spanning, vanaf het begin, in te bouwen in het katalytisch actieve overgangsmetaalcomplex.

Onze resultaten laten ook zien hoe elektronische effecten de activiteit op een selectieve manier kunnen bijstellen. De introductie van elektronenstuwende substituenten op de fosfineliganden versterkt bijvoorbeeld de elektronendonatie vanaf het palladium, en dit stabiliserende effect is vooral sterk voor C–H activering. Dit komt omdat de C–H activering gepaard gaat met een sterke interactie tussen katalysator en substraat. Aan de andere kant, voor de sterisch meer gehinderde C–C activering, is de destabiliserende sterische bulk van het substraat vaak de dominerende factor. Maar de relatieve invloed van deze elektronische en sterische factoren hangt ook af van andere parameters zoals, inderdaad, de bite angle: bij kleinere bite angles zijn de elektronische effecten relatief belangrijk, terwijl bij grotere bite angles de sterische factoren een prominentere rol spelen. Dit type gedrag, waarbij het effect van de liganden beïnvloed wordt door de intrinsieke reactiviteit van een bepaalde binding, komen we in dit proefschrift bij veel substraten en structurele motieven in de katalysator tegen.

Hoofdstukken 4 en 5 concentreren zich op het effect van sterische bulk in het substraat op de activering van C–H en C–C bindingen in alkanen. Alhoewel de bindingen zwakker worden bij een verhoging van het aantal methylsubstituenten, stijgen de barrières voor hun activering. De volledig gesubstitueerde bindingen geven de hoogste barrières. De reden voor de hogere activeringsbarrières van de zwakkere bindingen is dat de methylgroepen de effectieve interactie van de katalysator met de binding hinderen. Het substraat moet deformeren om ruimte te maken voor het metaal, voordat een bevorderlijke, stabiliserende interactie plaats kan vinden. De interactie wordt verder ook verzwakt door een geringere elektronendonatie van palladium naar de binding. Dit komt door de energieën van de σ^* orbitalen, die voor substraten met meer sterische bulk minder snel dalen langs het reactiepad.

Hoofdstukken 6 en 7 gaan over een serie waterstof-element en koolstof-element bindingen in $H-AH_n$ and CH_3-AH_n ($AH_n = CH_3, NH_2, OH,$ and F), welke twee reeksen van toenemend polaire bindingen in de tweede periode voorstellen. Hoofdstuk 6 behandelt de trends in bindingssterktes voor deze substraten en beschrijft hoe de CH_3

groep zich anders gedraagt dan de rest van de tweede periode AH_n -groepen, doordat het methylradicaal weg buigt naar de parapluvorm die het heeft in het overall molecuul. Het belangrijkste verschil met de andere $H-AH_n$ en CH_3-AH_n bindingen is dat ze vrije elektronenparen op A hebben die niet, zoals de $A-H$ bindingen, kunnen weg buigen door een waterstofkern te verplaatsen. Het resultaat is een lagere Pauli repulsie, waardoor de bindingen met de methylgroep sterker zijn dan verwacht op basis van verschillen in electronegativiteit.

Hoofdstuk 7 behandelt de activering van deze serie van toenemend polaire bindingen door ongecoördineerd palladium. De bindingssterktes zijn overheersend in de bepaling van de trends: een meer polaire binding is sterker en heeft een hogere activeringsspanning en dus een hogere activeringsbarrière. Het effect hiervan wordt tot op zeker hoogte tegengegaan door een verbeterde electronendotatie van palladium naar de lager liggende σ^* LUMO orbitalen van de meer polaire bindingen. In gevallen waar $AH_n = CH_3$, kunnen we concluderen dat de sterisch meer gehinderde methylgroep altijd een hogere activeringsspanning induceert dan verwacht zou worden op basis van de bindingssterktes. Dit gedrag, waarbij de stap naar een volledig gesubstitueerde groep ineens een sterke verhoging van de spanningsenergie veroorzaakt, is vergelijkbaar met de stap naar de volledig gesubstitueerde alkaanbindingen in hoofdstukken 4 en 5.

Hoofdstuk 8 behandelt de activering van de verschillend gehybridiseerde bindingen $C(sp^3)-X$, $C(sp^2)-X$, and $C(sp)-X$ in X -gesubstitueerd ethaan, etheen en ethyn, met $X = H, CH_3,$ and Cl . In deze serie observeren we een trend van dalende barrièrehogtes bij activering door palladium, ondanks het feit dat de bindingen sterker worden. Er zijn twee belangrijke redenen voor dit gedrag: 1) van sp^3 naar sp hybridisatie, verbetert de electronendotatie vanuit palladium door de lager liggende σ^*_{C-X} LUMO orbitaal op het substraat, en in mindere mate door interactie met de π_{C-C} and π^*_{C-C} orbitalen; 2) verminderde sterische repulsie omdat de geactiveerde $C-X$ binding sterisch minder gehinderd wordt wanneer het koolstofatoom van sp^3 naar sp hybridisatie gaat.

11 Dankwoord

In dit traditioneel meest gelezen onderdeel van een proefschrift hoort eigenlijk een uitgebreide persoonlijke en intieme uiteenzetting te staan over eenieder die mij heeft bijgestaan, geïnspireerd en/of gemotiveerd gedurende mijn promotietijd. Uiteraard zijn er genoeg mensen die hiervoor in aanmerking komen, maar die weten zelf heel goed dat ik ze dankbaar ben; een droge opsomming lijkt me hier dus niet erg nuttig. Dit gebrek aan een publieke uiting van dank is echter hopelijk voor mensen die mij goed genoeg kennen alleen maar vanzelfsprekend en zou niet als schofferend ervaren hoeven te worden. Desalniettemin ben ik uiteraard nooit te beroerd om mensen tegemoet te komen die behoefte hebben aan een persoonlijk dankwoordje.

Verder blijft bij gebrek aan poëtische inspiratie van mijn kant een algemene lofrede helaas ook uit en ben ik, hoe betreurenswaardig dit ook moge zijn, genoodzaakt het kort te houden.

Dus bij deze richt ik mij aan iedereen die een persoonlijk dankbetuiging van mij verdient om wat voor reden dan ook: Dank!

Cheers,

WJ

12 List of publications

1. "Phosphaspiropentene as a transient intermediate"
J. C. Slootweg, W.-J. van Zeist, F. J. J. de Kanter, M. Schakel, A. W. Ehlers, M. Lutz, A. L. Spek, K. Lammertsma
Organometallics **2005**, *24*, 5172
2. "PyFrag - Streamlining your reaction path analysis"
W.-J. van Zeist, C. Fonseca Guerra, F. M. Bickelhaupt
J. Comput. Chem. **2008**, *29*, 312
3. "Reaction Coordinates and the Transition-Vector Approximation to the IRC"
W.-J. van Zeist, A. H. Koers, L. P. Wolters, F. M. Bickelhaupt
J. Chem. Theory. Comput. **2008**, *4*, 920
4. "Linkage Isomerism of Nitriles in Rhodium Half-Sandwich Metallacycles"
L. Orian, W.-J. van Zeist, F. M. Bickelhaupt
Organometallics **2008**, *27*, 4028
5. "Tricarbonylchromium Complexes of [5]- and [6]Metacyclophane: An Experimental and Theoretical Study"
M. J. van Eis, S. van Loon, M. Lutz, A. L. Spek, W. H. de Wolf, F. Bickelhaupt, W.-J. van Zeist, F. M. Bickelhaupt
Tetrahedron **2008**, *64*, 11641
6. "The Steric Nature of the Bite Angle"
W.-J. van Zeist, R. Visser, F. M. Bickelhaupt
Chem. Eur. J. **2009**, *15*, 6112
7. "Trends and anomalies in H–AH_n and CH₃–AH_n bond strengths (AH_n = CH₃, NH₂, OH, F)"
W.-J. van Zeist, F. M. Bickelhaupt
Phys. Chem. Chem. Phys. **2009**, *11*, 10317
8. "Halogen versus halide electronic structure"
W.-J. van Zeist, Y. Ren, F. M. Bickelhaupt
Sci. China Ser. B-Chem. **2009**, *53*, 210

9. "Comment on "The Interplay between Steric and Electronic Effects in S_N2 Reactions""
W.-J. van Zeist, F. M. Bickelhaupt
Chem. Eur. J. **2010**, *16*, 5538
10. "The Activation Strain Model of Chemical Reactivity"
W.-J. van Zeist, F. M. Bickelhaupt
Org. Biomol. Chem. **2010**, *8*, 3118
11. "Survival of the Weakest: Catalyst Selection based on Intermediate Stability measured by Mass Spectrometry"
J. Wassenaar, E. Jansen, W.-J. van Zeist, F. M. Bickelhaupt, M. A. Siegler, A. L. Spek, J. N. H. Reek
Nature Chem. **2010**, *2*, 417
12. "Mass Spectrometry of Silver-Adducted Ferrocenyl Catalyst Complexes in Continuous-Flow Reaction Detection Systems. Part. I: Fragmentation in MS^n "
C. T. Martha, W.-J. van Zeist, F. M. Bickelhaupt, H. Irth, W. M. A. Niessen
J. Mass Spectrom. **2010**, *45*, 1332
13. "Steric Nature of the Bite Angle. A Closer and a Broader Look"
W.-J. van Zeist, F. M. Bickelhaupt
Dalton Trans. **2010**, *40*, 3028
14. "The effect of steric bulk on Pd(0)-catalyzed C–H bond activation: Perspectives from an extended activation strain model"
J. N. P. van Stralen, D. P. Geerke, W.-J. van Zeist, F. M. Bickelhaupt
To be submitted
15. "The effect of steric bulk on Pd(0)-catalyzed C–C bond activation: Perspectives from an extended activation strain model"
W.-J. van Zeist, J. N. P. van Stralen, D. P. Geerke, F. M. Bickelhaupt
To be submitted
16. "Trends in Pd(0) catalytic bond activation of H– AH_n and CH_3 – AH_n bonds (AH_n = CH_3 , NH_2 , OH , and F)"
W.-J. van Zeist, A. H. Koers, L. P. Wolters, F. M. Bickelhaupt
In preparation
17. "The effects of substrate hybridization on model palladium oxidative insertion reactions"
W.-J. van Zeist, F. M. Bickelhaupt
In preparation

13 References

1. A. Diefenbach *Fragment-orientated Design of Catalysts. A theoretical study on bond activation*, Doctoral Dissertation, Philipps-Universität, Marburg, 2000.
2. G. Th. de Jong *Theoretical Studies on Catalytic Bond Activation*, Doctoral Dissertation, Vrije Universiteit, Amsterdam, 2007.
3. "The Nobel Prize in Chemistry 2010". Nobelprize.org. 9 Oct 2010, http://nobelprize.org/nobel_prizes/chemistry/laureates/2010/index.html.
4. J. C. Fiaud, J.-L. Malleron, J. Y. Legros, *Handbook of Palladium Catalyzed Organic Reactions*. Academic Press: 1997.
5. J. P. Collman, L. S. Hegedus, J. R. Norton, R. G. Finke, *Principles and Applications of Organotransition Metal Chemistry*. University Science Books: Mill Valley, CA, 1987.
6. C. Elschenbroich, *Organometallics*. 3rd ed.; Wiley-VCH: Weinheim, 2006.
7. M. B. Smith, *March's advanced organic chemistry: reactions, mechanisms, and structure*. 5 ed.; Wiley: New York, 2001.
8. R. H. Crabtree, *J. Organomet. Chem.* **2004**, *689*, 4083.
9. M. Lersch, M. Tilset, *Chem. Rev.* **2005**, *105*, 2471.
10. A. E. Shilov, G. B. Shul'pin, *Chem. Rev.* **1997**, *97*, 2879.
11. M. E. van der Boom, D. Milstein, *Chem. Rev.* **2003**, *103*, 1759.
12. J. C. Weisshaar, *Acc. Chem. Res.* **1993**, *26*, 213.
13. K. C. Nicolaou, P. G. Bulger, D. Sarlah, *Angew. Chem.* **2005**, *117*, 4516.
14. J. Y. Corey, J. Braddock-Wilking, *Chem. Rev.* **1999**, *99*, 175.
15. R. H. Crabtree, *Chem. Rev.* **1995**, *95*, 987.
16. J. J. Carroll, K. L. Haug, J. C. Weisshaar, M. R. A. Blomberg, P. E. M. Siegbahn, M. Svensson, *J. Phys. Chem.* **1995**, *99*, 13955.
17. A. Dedieu, *Chem. Rev.* **2000**, *100*, 543.
18. T. R. Griffin, D. B. Cook, A. Haynes, J. M. Pearson, D. Monti, G. E. Morris, *J. Am. Chem. Soc.* **1996**, *118*, 3029.
19. H. Heiberg, O. Gropen, O. Swang, *Int. J. Quant. Chem.* **2003**, *92*, 391.
20. S. Q. Niu, M. B. Hall, *Chem. Rev.* **2000**, *100*, 353.
21. P. E. M. Siegbahn, *J. Am. Chem. Soc.* **1996**, *118*, 1487.
22. M. Torrent, M. Solà, G. Frenking, *Chem. Rev.* **2000**, *100*, 439.
23. J. C. Cramer, D. G. Truhlar, *Phys. Chem. Chem. Phys.* **2009**, *11*, 10757.
24. A. M. C. Wittborn, M. Costas, M. R. A. Blomberg, P. E. M. Siegbahn, *J. Chem. Phys.* **1997**, *107*, 4318.
25. T. Ziegler, *Chem. Rev.* **1991**, *91*, 651.
26. L. Xue, Z. Lin, *Chem. Soc. Rev.* **2010**, *39*, 1692.
27. B. Bunnik, G. Kramer, R. van Santen, *Top. Catal.* **2010**, *53*, 403.
28. A. Michaelides, Z.-P. Liu, C. J. Zhang, A. Alavi, D. A. King, P. Hu, *J. Am. Chem. Soc.* **2003**, *125*, 3704.
29. A. Ariafard, Z. Y. Lin, *Organometallics* **2006**, *25*, 4030.
30. A. C. Balazs, K. H. Johnson, G. M. Whitesides, *Inorg. Chem.* **1982**, *21*, 2162.
31. J. M. Gonzales, D. G. Musaev, K. Morokuma, *Organometallics* **2005**, *24*, 4908.
32. J. J. Low, W. A. Goddard III, *Organometallics* **1986**, *5*, 609.
33. J. J. Low, W. A. Goddard, *J. Am. Chem. Soc.* **1986**, *108*, 6115.
34. S. Sakaki, M. Ogawa, M. Kinoshita, *J. Phys. Chem.* **1995**, *99*, 9933.
35. M. D. Su, S. Y. Chu, *Inorg. Chem.* **1998**, *37*, 3400.
36. P. Hofmann, H. Heiss, G. Müller, *Zeitschrift fuer Naturforschung, B: Chemical Sciences* **1987**, *42*, 395.
37. S. Sakaki, B. Biswas, M. Sugimoto, *J. Chem. Soc., Dalton Trans.* **1997**, 803.
38. S. Kozuch, C. Amatore, A. Jutand, S. Shaik, *Organometallics* **2005**, *24*, 2319.
39. A. Diefenbach, G. Th. de Jong, F. M. Bickelhaupt, *J. Chem. Theory Comput.* **2005**, *1*, 286.

40. R. Dreizler, E. Gross, *Density Functional Theory*. Plenum Press: New York, 1995.
41. W. Koch, M. C. Holthausen, *A Chemist's Guide to Density Functional Theory*. 2 ed.; Wiley-VCH: Weinheim, 2002.
42. R. G. Parr, W. Yang, *Density-Functional Theory of Atoms and Molecules*. Oxford University Press: New York, 1989.
43. A. D. Becke, *J. Chem. Phys.* **1986**, *84*, 4524.
44. A. D. Becke, *Phys. Rev. A* **1988**, *38*, 3098.
45. C. T. Lee, W. T. Yang, R. G. Parr, *Phys. Rev. B* **1988**, *37*, 785.
46. E. J. Baerends, O. V. Gritsenko, *J. Phys. Chem. A* **1997**, *101*, 5383.
47. F. M. Bickelhaupt, E. J. Baerends, Kohn-Sham density functional theory: Predicting and understanding chemistry. In *Rev. Comput. Chem.*, Lipkowitz, K. B.; Boyd, D. B., Eds. VCH Publishers Inc.: New York, 2000; Vol. 15, pp 1.
48. E. J. Baerends, T. Ziegler, J. Autschbach, D. Bashford, A. Bérces, F. M. Bickelhaupt, C. Bo, P. M. Boerrigter, L. Cavallo, D. P. Chong, L. Deng, R. M. Dickson, D. E. Ellis, M. v. Faassen, L. Fan, T. H. Fischer, C. F. Guerra, A. Ghysels, A. Giammona, S. J. A. v. Gisbergen, A. W. Götz, A. Groeneveld, O. V. Gritsenko, M. Grüning, S. Gusarov, F. E. Harris, P. v. d. Hoek, C. R. Jacob, H. Jacobsen, L. Jensen, J. W. Kaminski, G. v. Kessel, F. Kootstra, A. Kovalenko, M. V. Krykunov, E. v. Lenthe, D. A. McCormack, A. Michalak, M. Mitoraj, J. Neugebauer, V. P. Nicu, L. Noodleman, V. P. Osinga, S. Patchkovskii, P. H. T. Philipsen, D. Post, C. C. Pye, W. Ravenek, J. I. Rodríguez, P. Ros, P. R. T. Schipper, G. Schreckenbach, J. S. Seldenthuis, M. Seth, J. G. Snijders, M. Solà, M. Swart, D. Swerhone, G. te Velde, P. Vernooijs, L. Versluis, L. Visscher, O. Visser, F. Wang, T. A. Wesolowski, E. M. v. Wezenbeek, G. Wiesenekker, S. K. Wolff, T. K. Woo, A. L. Yakovlev *ADF2009.01, SCM, Theoretical Chemistry, Vrije Universiteit, Amsterdam, The Netherlands*, <http://www.scm.com>, SCM: Amsterdam.
49. G. te Velde, F. M. Bickelhaupt, E. J. Baerends, C. Fonseca Guerra, S. J. A. van Gisbergen, J. G. Snijders, T. Ziegler, *J. Comput. Chem.* **2001**, *22*, 932.
50. G. Th. de Jong, F. M. Bickelhaupt, *J. Chem. Theory Comput.* **2006**, *2*, 322.
51. G. Th. de Jong, F. M. Bickelhaupt, *J. Phys. Chem. A* **2005**, *109*, 9685.
52. G. Th. de Jong, D. P. Geerke, A. Diefenbach, F. M. Bickelhaupt, *Chem. Phys.* **2005**, *313*, 261.
53. G. Th. de Jong, D. P. Geerke, A. Diefenbach, M. Solà, F. M. Bickelhaupt, *J. Comput. Chem.* **2005**, *26*, 1006.
54. G. Th. de Jong, M. Solà, L. Visscher, F. M. Bickelhaupt, *J. Chem. Phys.* **2004**, *121*, 9982.
55. J. G. Snijders, E. J. Baerends, P. Vernooijs, *At. Data Nucl. Data tables* **1982**, *26*, 483.
56. E. J. Baerends, D. E. Ellis, P. Ros, *Chem. Phys.* **1973**, *2*, 41.
57. J. Krijn, E. J. Baerends, *Fit-functions in the HFS-method (Internal Report in Dutch)* **1984**.
58. S. H. Vosko, L. Wilk, M. Nusair, *Can. J. Phys.* **1980**, *58*, 1200.
59. C. Chang, M. Péliissier, P. Durand, *Phys. Scr.* **1986**, *34*, 394.
60. E. van Lenthe, E. J. Baerends, J. G. Snijders, *J. Chem. Phys.* **1994**, *101*, 9783.
61. E. van Lenthe, R. van Leeuwen, E. J. Baerends, J. G. Snijders, *Int. J. Quant. Chem.* **1996**, *57*, 281.
62. A. Diefenbach, F. M. Bickelhaupt, *J. Chem. Phys.* **2001**, *115*, 4030.
63. A. Klamt, *J. Phys. Chem.* **1995**, *99*, 2224.
64. A. Klamt, V. Jones, *J. Chem. Phys.* **1996**, *105*, 9972.
65. A. Klamt, G. Schüürman, *J. Chem. Soc. Perkin Trans. 2* **1993**, 799.
66. C. C. Pye, T. Ziegler, *Theor. Chem. Acc.* **1999**, *101*, 396.
67. M. Swart, E. Rösler, F. M. Bickelhaupt, *Eur. J. Inorg. Chem.* **2007**, 3646.
68. G. Th. de Jong, F. M. Bickelhaupt, *J. Chem. Theory Comput.* **2007**, *3*, 514.
69. M. Swart, F. M. Bickelhaupt, *J. Comput. Chem.* **2008**, *29*, 724.
70. L. Fan, L. Versluis, T. Ziegler, E. J. Baerends, W. Ravenek, *Int. J. Quant. Chem.* **1988**, 173.
71. L. Fan, T. Ziegler, *J. Chem. Phys.* **1990**, *92*, 3645.
72. K. Fukui, *J. Phys. Chem.* **1970**, *74*, 4161.
73. K. Ishida, K. Morokuma, A. Komornicki, *J. Chem. Phys.* **1977**, *66*, 2153.
74. K. Fukui, *Acc. Chem. Res.* **1981**, *14*, 363.
75. C. Gonzalez, H. Schlegel, *J. Phys. Chem.* **1990**, *94*, 5523.
76. L. Deng, T. Ziegler, L. Fan, *J. Chem. Phys.* **1993**, *99*, 3823.
77. W.-J. van Zeist, A. H. Koers, L. P. Wolters, F. M. Bickelhaupt, *J. Chem. Theory Comput.* **2008**, *4*, 920.

78. P. W. Atkins, *Physical Chemistry*. Oxford University Press: Oxford, 1998.
79. F. M. Bickelhaupt, *J. Comput. Chem.* **1999**, *20*, 114.
80. W.-J. van Zeist, F. M. Bickelhaupt, *Org. Biomol. Chem.* **2010**, *8*, 3118.
81. F. M. Bickelhaupt, E. J. Baerends, N. M. M. Nibbering, *Chem. Eur. J.* **1996**, *2*, 196.
82. J. N. P. van Stralen, F. M. Bickelhaupt, *Organometallics* **2006**, *25*, 4260.
83. G. Th. de Jong, F. M. Bickelhaupt, *ChemPhysChem* **2007**, *8*, 1170.
84. D. Heidrich, *The Reaction Path in Chemistry: Current Approaches and Perspectives*. Kluwer Academic Publishers: Dordrecht, The Netherlands, 1995.
85. T. Ziegler, J. Autschbach, *Chem. Rev.* **2005**, *105*, 2695.
86. W.-J. van Zeist, C. Fonseca Guerra, F. M. Bickelhaupt, *J. Comput. Chem.* **2008**, *29*, 312.
87. T. Ziegler, A. Rauk, *Theor. Chim. Acta* **1977**, *46*, 1.
88. T. Ziegler, A. Rauk, *Inorg. Chem.* **1979**, *18*, 1558.
89. A. Krapp, F. M. Bickelhaupt, G. Frenking, *Chem. Eur. J.* **2006**, *12*, 9196.
90. W.-J. van Zeist, F. M. Bickelhaupt, *Phys. Chem. Chem. Phys.* **2009**, *11*, 10317.
91. F. M. Bickelhaupt, E. J. Baerends, *Angew. Chem. Int. Edit.* **2003**, *42*, 4183.
92. J. Poater, M. Solà, F. M. Bickelhaupt, *Chem. Eur. J.* **2006**, *12*, 2889.
93. A. Diefenbach, F. M. Bickelhaupt, *J. Phys. Chem. A* **2004**, *108*, 8460.
94. W.-J. van Zeist, R. Visser, F. M. Bickelhaupt, *Chem. Eur. J.* **2009**, *15*, 6112.
95. A. Diefenbach, G. Th. de Jong, F. M. Bickelhaupt, *Mol. Phys.* **2005**, *103*, 995.
96. G. Th. de Jong, F. M. Bickelhaupt, *Can. J. Chem.* **2009**, *87*, 806.
97. G. Th. de Jong, A. Kovács, F. M. Bickelhaupt, *J. Phys. Chem. A* **2006**, *110*, 7943.
98. G. Th. de Jong, R. Visser, F. M. Bickelhaupt, *J. Organomet. Chem.* **2006**, *691*, 4341.
99. P. E. M. Siegbahn, M. R. A. Blomberg, *J. Am. Chem. Soc.* **1992**, *114*, 10548.
100. I. Fernández, G. Frenking, E. Uggerud, *Chem. Eur. J.* **2009**, *15*, 2116.
101. W.-J. van Zeist, F. M. Bickelhaupt, *Chem. Eur. J.* **2010**, *16*, 5538.
102. I. Fernández, G. Frenking, E. Uggerud, *Chem. Eur. J.* **2010**, *16*, 5542.
103. A. P. Bento, F. M. Bickelhaupt, *J. Org. Chem.* **2007**, *72*, 2201.
104. S. C. A. H. Pierrefixe, C. Fonseca Guerra, F. M. Bickelhaupt, *Chem. Eur. J.* **2008**, *14*, 819.
105. M. A. van Bochove, M. Swart, F. M. Bickelhaupt, *J. Am. Chem. Soc.* **2006**, *128*, 10738.
106. J. Poater, R. Visser, M. Solà, F. M. Bickelhaupt, *J. Org. Chem.* **2007**, *72*, 1134.
107. S.-G. Wang, Y.-X. Qiu, W. H. E. Schwarz, *Chem. Eur. J.* **2009**, *15*, 6032.
108. A. Taichibana, K. Fukui, *Theor. Chim. Acta* **1979**, *51*, 189.
109. C. Fonseca Guerra, J.-W. Handgraaf, E. J. Baerends, F. M. Bickelhaupt, *J. Comput. Chem.* **2004**, *25*, 189.
110. P. W. N. M. van Leeuwen, P. C. J. Kamer, J. N. H. Reek, P. Dierkes, *Chem. Rev.* **2000**, *100*, 2741.
111. M. Birkholz (nee Gensow), Z. Freixa, P. W. N. M. van Leeuwen, *Chem. Soc. Rev.* **2009**, *38*, 1099.
112. D. C. Graham, K. J. Cavell, B. F. Yates, *Dalton Trans.* **2005**, 1093.
113. E. Zuidema, P. W. N. M. van Leeuwen, C. Bo, *Organometallics* **2005**, *24*, 3703.
114. C. A. Tolman, *Chem. Rev.* **1977**, *77*, 313.
115. S. Otsuka, *J. Organomet. Chem.* **1980**, *200*, 191.
116. J. J. Low, W. A. Goddard, *J. Am. Chem. Soc.* **1984**, *106*, 6928.
117. P. Dierkes, P. W. N. M. van Leeuwen, *J. Chem. Soc., Dalton Trans.* **1999**, 1519.
118. Z. Freixa, P. W. N. M. van Leeuwen, *Dalton Trans.* **2003**, 1890.
119. J. Hageman, J. Westerhuis, H. Frühauf, G. Rothenberg, *Adv. Synth. Catal.* **2006**, *348*, 361.
120. V. P. Ananikov, D. G. Musaev, K. Morokuma, *Eur. J. Inorg. Chem.* **2007**, 5390.
121. R. Fazaeli, A. Ariafard, S. Jamshidi, E. S. Tabatabaie, K. A. Pishro, *J. Organomet. Chem.* **2007**, *692*, 3984.
122. N. Fey, J. N. Harvey, G. C. Lloyd-Jones, P. Murray, A. G. Orpen, R. Osborne, M. Purdie, *Organometallics* **2008**, *27*, 1372.
123. N. Fey, A. G. Orpen, J. N. Harvey, *Coordin. Chem. Rev.* **2009**, *253*, 704.
124. S. Kozuch, S. Shaik, *J. Mol. Cat. A* **2010**, *324*, 120.
125. S. Sakaki, N. Mizoe, Y. Musashi, B. Biswas, M. Sugimoto, *J. Phys. Chem. A* **1998**, *102*, 8027.
126. T. Matsubara, K. Hirao, *Organometallics* **2002**, *21*, 4482.
127. J. Wassenaar, E. Jansen, W. J. van Zeist, F. M. Bickelhaupt, A. L. Siegler, A. L. Spek, J. N. H. Reek, *Nature Chem.* **2010**, *2*, 417.

128. C. Amatore, A. Jutand, *Acc. Chem. Res.* **2000**, *33*, 314.
129. C. A. Caputo, A. L. Brazeau, Z. Hynes, J. T. Price, H. M. Tuononen, N. D. Jones, *Organometallics* **2009**, *28*, 5261.
130. S. Kozuch, S. Shaik, A. Jutand, C. Amatore, *Chem. Eur. J.* **2004**, *10*, 3072.
131. C. M. Crudden, D. P. Allen, *Coordin. Chem. Rev.* **2004**, *248*, 2239.
132. E. Peris, R. Crabtree, *Coordin. Chem. Rev.* **2004**, *248*, 2239.
133. J. A. Mata, M. Poyatos, E. Peris, *Coordin. Chem. Rev.* **2007**, *251*, 841.
134. S. Díez-González, S. P. Nolan, *Coordin. Chem. Rev.* **2007**, *251*, 874.
135. P. de Fremont, N. Marion, S. P. Nolan, *Coordin. Chem. Rev.* **2009**, *253*, 862.
136. M. Poyatos, J. A. Mata, E. Peris, *Chem. Rev.* **2009**.
137. J. A. Gillespie, D. L. Dodds, P. C. J. Kamer, *Dalton Trans.* **2010**, *39*, 2751.
138. S. J. Blanksby, G. B. Ellison, *Acc. Chem. Res.* **2003**, *36*, 255.
139. S. Gronert, *J. Org. Chem.* **2006**, *71*, 1209.
140. S. Gronert, *Chem. Eur. J.* **2009**, *15*, 5372.
141. K. U. Ingold, G. A. DiLabio, *Org. Lett.* **2006**, *8*, 5923.
142. M. D. Wodrich, C. S. Wannere, Y. Mo, P. D. Jarowski, K. N. Houk, P. v. R. Schleyer, *Chem. Eur. J.* **2007**, *13*, 7731.
143. M. L. Coote, A. Pross, L. Radom, *Org. Lett.* **2003**, *5*, 4689.
144. F. De Vleeschouwer, V. Van Speybroeck, M. Waroquier, P. Geerlings, F. De Proft, *J. Org. Chem.* **2008**, *73*, 9109.
145. Y. Fu, X. Y. Dong, Y. M. Wang, L. Liu, Q. X. Guo, *Chin. J. Chem.* **2005**, *23*, 474.
146. S. Grimme, *J. Comput. Chem.* **2006**, *27*, 1787.
147. K. U. Ingold, J. S. Wright, *J. Chem. Educ.* **2000**, *77*, 1062.
148. E. I. Izgorodina, M. L. Coote, L. Radom, *J. Phys. Chem. A* **2005**, *109*, 7558.
149. D. Kaur, R. P. Kaur, R. Kaur, *J. Mol. Struct. (Theochem)* **2007**, *803*, 95.
150. O. Mo, M. Yanez, M. Eckert-Maksic, Z. B. MAKŠIĆ, I. Alkorta, J. Elguero, *J. Phys. Chem. A* **2005**, *109*, 4359.
151. Y. Zhao, D. G. Truhlar, *Acc. Chem. Res.* **2008**, *41*, 157.
152. A. L. Allred, *J. Inorg. Nucl. Chem.* **1961**, 215.
153. L. Pauling, *J. Am. Chem. Soc.* **1931**, *53*, 1367.
154. F. M. Bickelhaupt, H. L. Hermann, G. Boche, *Angew. Chem. Int. Edit.* **2006**, *45*, 823.
155. F. M. Bickelhaupt, M. Solà, C. Fonseca Guerra, *Inorg. Chem.* **2007**, *46*, 5411.
156. L. Q. Deng, V. Branchadell, T. Ziegler, *J. Am. Chem. Soc.* **1994**, *116*, 10645.
157. F. M. Bickelhaupt, T. Ziegler, P. V. Schleyer, *Organometallics* **1996**, *15*, 1477.

